

## **General circulation modelling of close-in extrasolar giant planets**

Thrastarson, Heidar Thor

The copyright of this thesis rests with the author and no quotation from it or information derived from it may be published without the prior written consent of the author

For additional information about this publication click this link.

<http://qmro.qmul.ac.uk/jspui/handle/123456789/2448>

Information about this research object was correct at the time of download; we occasionally make corrections to records, please therefore check the published record when citing. For more information contact [scholarlycommunications@qmul.ac.uk](mailto:scholarlycommunications@qmul.ac.uk)

# **General Circulation Modelling of Close-in Extrasolar Giant Planets**

**Heidar Thor Thrastarson**

Thesis submitted for the degree of  
Doctor of Philosophy (PhD)  
of the University of London

Queen Mary University of London

2011



# Abstract

A large fraction of the extrasolar planets detected so far are giant planets that have such short orbital periods (a few days) that they are thought to be tidally-synchronised with the host star. Such orbits lead to permanent day/night sides on the planets and provide a forcing condition for atmospheric dynamics that is not present in the Solar System. The main subject of this thesis is to model the atmospheric dynamics of these close-in extrasolar giant planets, using an accurate three-dimensional general circulation model (GCM).

Using the GCM, the primitive equations are numerically solved, with idealised forcing represented by Newtonian relaxation. A large number of simulations is performed to thoroughly explore the relevant physical and numerical parameter space.

First, it is found that different initial flow states lead to markedly different flow and temperature distributions. This result is in contrast with the results or assumptions of many published studies, and underlines the fact that circulation models are currently unsuitable for quantitative predictions without better constrained, and well-posed, initial conditions.

Second, the effects of artificial viscosity – particularly in relation to the thermal relaxation timescale – are studied. It is demonstrated that using a large range of thermal time scales, including very short ones ( $\sim 1$  h), as is common in the literature, leads to dominant noise and/or excessively dissipated fields.

Finally, variations of the strength of thermal forcing are studied. Distinct stationary or oscillatory states are identified for different sets of forcing parameters. In addition, multiple long lasting states are observed for a given forcing. Most of the states are characterised by a low number ( $\sim 4$ ) of large-scale vortices and planetary waves, which exhibit a periodic

time variability. The spatiotemporal variability can be important for observational studies, and provides a strong argument for making repeated measurements of a given planet.

# Declaration

This thesis describes work done at the Astronomy Unit of the School of Mathematical Sciences, at Queen Mary University of London, under the supervision of Dr. James Y-K. Cho. The results presented in Chapters 3 and 4 contain original material that has been published in a peer reviewed journal in the following articles:

- Thrastarson, H. T., and J. Y-K. Cho (2010), Effects of Initial Flow on Close-in Planet Atmospheric Circulation, *ApJ*, 716, 144153.
- Thrastarson, H. T., and J. Y-K. Cho (2011), Relaxation Time and Dissipation Interaction in Hot Planet Atmospheric Flow Simulations, *ApJ*, 729, 117.

I hereby declare that the work presented in this thesis is my own, unless otherwise stated.

Heidar Thor Thrastarson  
12 July 2011

# Acknowledgements

My deepest gratitude goes to my supervisor James Y-K. Cho. It has been a privilege to benefit from his guidance, knowledge and generosity. The times of pushing and ‘pestering’ questions are much appreciated too! And I have lost count of the sushi-dinners I owe you now!

Before starting my PhD studies I didn’t fully realise the benefits of being part of an active research group. Now I know how it can multiply the learning and knowledge of each individual member. Thanks to members of the PAD-group, Orkan (Matt) Umurhan, Chris Watkins, Ali Gulsen, Inna Polichtchouk and Tommi Koskinen, for providing an enjoyable and stimulating group atmosphere, and for all the feedback on the work described in this thesis. Also thanks to Inna and Chris for proofreading parts of the thesis.

Thanks to my family. To my mother Hulda and my sister Drifa, for their understanding, encouragement and mental support. To my brother Ulli, and sister-in-law Marta, for all their generous hosting and support throughout my time in London.

Thanks to my flat mates and friends and colleagues at Queen Mary for all the helpful – and unhelpful – discussions, and for making my time in London a very enjoyable experience.

Finally, I acknowledge my funding support from the EU fellowship.

# Contents

<b>1</b>	<b>Introduction</b>	<b>15</b>
1.1	Extrasolar Planets . . . . .	15
1.1.1	Hot Jupiters . . . . .	17
1.2	Planetary Atmospheres . . . . .	19
1.2.1	Constraints from Observations . . . . .	20
1.3	Previous Modelling Work . . . . .	21
1.4	Outline of the Thesis . . . . .	22
<b>2</b>	<b>Governing Equations and Numerical Model</b>	<b>23</b>
2.1	The Primitive Equations . . . . .	23
2.2	Dynamical Regime . . . . .	26
2.3	General Circulation Model . . . . .	30
2.3.1	The CAM Equations in Continuous Form . . . . .	31
2.3.2	Physical Parameterisations . . . . .	35
2.3.3	Numerical Methods . . . . .	36
<b>3</b>	<b>Effects of Initial Conditions</b>	<b>39</b>
3.1	Introduction . . . . .	39
3.2	Method . . . . .	41
3.3	Results . . . . .	45
3.3.1	Basic Dependence: Jets . . . . .	45
3.3.2	Extreme Sensitivity: Small Stirring . . . . .	53
3.3.3	Robustness: Additional Parameter Variations . . . . .	53
3.4	Conclusion . . . . .	59
<b>4</b>	<b>Dissipation and Relaxation Time Interaction</b>	<b>61</b>
4.1	Introduction . . . . .	62

---

4.2	Method . . . . .	64
4.2.1	Numerical Algorithm . . . . .	64
4.2.2	Calculation Setup . . . . .	67
4.3	Results . . . . .	69
4.3.1	Spatial Dissipation . . . . .	69
4.3.2	Temporal Dissipation . . . . .	78
4.4	Conclusion . . . . .	85
<b>5</b>	<b>Coherent States and Internal Variability</b>	<b>88</b>
5.1	Introduction . . . . .	89
5.2	Zonally Asymmetric Heating and Waves . . . . .	91
5.3	Model Setup . . . . .	92
5.4	Results . . . . .	95
5.4.1	States for Varied Forcing Strength . . . . .	95
5.4.2	Transitions During Long Term Evolution . . . . .	108
5.4.3	Storms and Variability . . . . .	115
5.5	Conclusion . . . . .	118
<b>6</b>	<b>Conclusion</b>	<b>121</b>
6.1	Summary . . . . .	121
6.2	Outlook . . . . .	124

# List of Figures

- 3.1 Initial conditions for simulations RUN1 (—), RUN2 (---), RUN3 (— · —), and RUN4 (···). The height-independent, zonally-symmetric, eastward velocities,  $u(\lambda, \phi, \eta, 0) = u_0(\phi)$ , are shown. . . . . 45
- 3.2 Temperature (color map) and flow (streamlines) fields at  $t = 40 \tau_p$ , near the  $p \sim 900$  mbar level, for RUN1 (a), RUN2 (b), RUN3 (c), and RUN4 (d). The fields are shown in cylindrical-equidistant projection centred at the equator. The four simulations are set up identically, except for the initial wind field. The location and size of vortices, and the associated temperature patterns, strongly depend on the initial wind configuration. . . . . 47
- 3.3 Temperature (color map) and flow (streamlines) fields at  $t = 40 \tau_p$ , near the  $p \approx 85$  mbar level, for the same four simulations as shown in Figure 3.2: RUN1 (a), RUN2 (b), RUN3 (c) and RUN4 (d). The sensitivity to the initial wind state is present throughout all heights in the atmosphere. . . . . 48
- 3.4 Snapshots of temperature vertical cross-section at the sub-stellar longitude, at  $t = 40 \tau_p$ , for the four simulations presented in Figure 3.2: RUN1 (a), RUN2 (b), RUN3 (c) and RUN4 (d). The vertical temperature structure is strongly sensitive to the initial flow state, and usually contains an inversion. . . . . 49

- 
- 3.5 Time series of total kinetic energy, integrated over the domain, for RUN1 (black —), RUN2 (red ---), RUN3 (blue - · -), and RUN4 (green ---). . . . . 51
- 3.6 Temperature vertical cross-section at an arbitrary longitude ( $\lambda = 135^\circ$ ), averaged over 450 planetary rotations (150 thermal relaxation times), for the four simulations presented in Figure 3.2: RUN1 (a), RUN2 (b), RUN3 (c) and RUN4 (d). The difference in the temperature structure is independent of long time-averaging and is not due to a phase shift in a quasi-periodic evolution. . . . . 52
- 3.7 Temperature (color map) and flow (streamlines) fields after 1000 planetary rotations, at the  $p \sim 420$  mbar level, for two simulations differing only by small deviations in the initial wind. The top panel shows the result of a simulation started from rest, while the bottom panel is from a simulation started with a small perturbation. Note the clear asymmetry in the north-south direction, which only appears when the small perturbations are present in the initial state. . . . . 54
- 3.8 Snapshots of temperature fields (colour coded) with streamlines overlaid. Fields at the  $p \sim 900$  mbar level are shown at  $t = 1000$  planetary rotations, for two simulations (RUN6 and RUN7); the thermal relaxation time is 0.5 planetary rotations (42 hours) in these runs. The only difference between the simulations is the initial wind state. The top panel shows the result of a simulation started with only a small perturbation and the bottom panel is from a simulation started with a westward jet. The sensitivity to the initial flow state is still present for this small value of the thermal relaxation time (cf., RUNS 1–4). . . . . 56



- 3.9 Time averaged temperature fields from two simulations that differ only in the initial wind state. The two simulations (RUN6, top panel, and RUN7, bottom panel) and the vertical level ( $p \sim 900$  mbar) are the same as in Figure 3.8. The average is taken over 300 rotations (planet days 1200 to 1500). The location of the coldest spot differs by 40 degrees in longitude between the two simulations. . . . . 57
- 3.10 Time series of total kinetic energy, integrated over the domain, for RUN6 (black —) and RUN7 (red ---). . . . . 58
- 4.1 Vorticity field at  $t = 80 \tau_p$  (planet rotations), near the  $p \approx 85$  mb level, for two sets of five simulations (left column and right column) that are set up identically, except for the viscosity coefficient and the thermal relaxation time. The superdiffusion coefficient is  $\nu_4 = \{10^{24}, 10^{23}, 10^{22}, 10^{21}, 10^{20}\} \text{ m}^4 \text{ s}^{-1}$ , decreasing from top to bottom in each column. The panels in the left column have a relaxation time of  $\tau_{\text{th}} = 0.1 \tau_p$  while the panels on the right have  $\tau_{\text{th}} = 3 \tau_p$ . Red (blue) colour represents positive (negative) values of vorticity, with units  $\text{s}^{-1}$ . . . . . 71
- 4.2 Kinetic energy spectra for the fields shown in Figure 4.1 for simulations that are set up identically, except for the artificial viscosity and the thermal relaxation time. The runs shown in the upper panel have a relaxation time of  $\tau_{\text{th}} = 0.1 \tau_p$  while the runs on the lower panel have  $\tau_{\text{th}} = 3 \tau_p$ . The different coloured lines are for different values of  $\nu$ , as indicated in the legend. Note the different scales on the two panels—much more kinetic energy is contained in the flow when the relaxation time is short. The spectra reveal both under-dissipated (e.g. red line, left panel) and over-dissipated (e.g. blue line, left panel) flow fields. A  $\nu$ -value that seems to give a reasonable spectrum for the short  $\tau_{\text{th}}$  (e.g. black line, upper panel) results in over-dissipation for the longer  $\tau_{\text{th}}$  (black line, lower panel). . . . 73

- 4.3 Kinetic energy spectra for simulations that are set up identically, except for the artificial viscosity. The different lines refer to different values of  $\nu$ , as indicated in the legend. The blue and black lines are the same as in the upper panel of Figure 4.2, for which the viscosity is of biharmonic form ( $\nabla^4$  with  $p = 2$ ). But, the red line is for a simulation where the order of the viscosity is lower ( $p = 1$ ), the normal Newtonian viscosity. . . . . 77
- 4.4 Courant number as a function of time for two sets of runs with different values of  $\tau_{th}$  in each set. The four runs within each set have different  $\epsilon$  values, setting the strength of the Robert-Asselin time filter. For clarity each time series in a set has been offset vertically by 0.1 in the plot; and, the two sets, as groups, have been offset vertically by 0.5. The lower set of runs have  $\tau_{th} = 3 \tau_p$ , while the upper set of runs have  $\tau_{th} = 0.1 \tau_p$ . For each set the run with  $\epsilon = 0.001$  is indicated with a blue line,  $\epsilon = 0.002$  a red line,  $\epsilon = 0.006$  a green line, and  $\epsilon = 0.01$  a black line. . . . . 81
- 4.5 Temperature (color coded in K) with streamlines overlaid, for three simulations differing only in the value of  $\epsilon$ , shown at three moments in time. From left to right, the snapshots are taken at  $t = \{130, 138, 145\} \tau_p$ . The top row is from a run with  $\epsilon = 0.01$ , the middle row with  $\epsilon = 0.06$  and the bottom row  $\epsilon = 0.10$ . All the fields are shown at the  $p \approx 900$  mb level. The substellar point is at  $0^\circ$  longitude and latitude. . . . . 83
- 4.6 Temperature at a fixed point, at  $0^\circ$  longitude and  $30^\circ$  latitude, as a function of time for the first 150 planet rotations in two simulations. The two curves show results of simulations that are identical apart only from the strength of the Robert-Asselin time filter. The red curve is from a run with  $\epsilon = 0.10$ , and the blue curve from a run with  $\epsilon = 0.01$ . 84

- 5.1 Snapshots from run F1b\* (small  $\Delta T_e = 50$  K, slow relaxation  $\tau_{th} = 3 \tau_p$ ), at  $t = 100 \tau_p$ . The upper panels show temperature (colour) and wind fields (arrows) at high ( $\eta = 0.24$ , panel a) and low ( $\eta = 0.83$ , panel b) altitude. The lower panels show geopotential (colour) and wind fields (arrows) at the 30 mb (c) and 850 mb (d) pressure surfaces. The substellar point is in the middle of each plot at  $0^\circ$  longitude and latitude. . . . . 96
- 5.2 Snapshots from run F4b\* (large  $\Delta T_e = 500$  K, slow relaxation  $\tau_{th} = 3 \tau_p$ ), at  $t = 82 \tau_p$ . The upper panels show temperature (colour) and wind fields (arrows) at high ( $\eta = 0.24$ , panel a) and low ( $\eta = 0.83$ , panel b) altitude. The lower panels show geopotential (colour) and wind fields (arrows) at the 30 mb (c) and 500 mb (d) pressure surfaces. 97
- 5.3 Snapshots from run F1d\* (small  $\Delta T_e = 50$  K, fast relaxation  $\tau_{th} = 0.1 \tau_p$ ), at  $t = 100 \tau_p$ . The upper panels show temperature (colour) and wind fields (arrows) at high ( $\eta = 0.24$ , panel a) and low ( $\eta = 0.83$ , panel b) altitude. The lower panels show geopotential (colour) and wind fields (arrows) at the 30 mb (c) and 700 mb (d) pressure surfaces. 98
- 5.4 Snapshots from run F4d\* (large  $\Delta T_e = 500$  K, fast relaxation  $\tau_{th} = 3 \tau_p$ ), at  $t = 100 \tau_p$ . The upper panels show temperature (colour) and wind fields (arrows) at high ( $\eta = 0.24$ , panel a) and low ( $\eta = 0.83$ , panel b) altitude. The lower panels show geopotential (colour) and wind fields (arrows) at the 30 mb (c) and 600 mb (d) pressure surfaces. 99
- 5.5 Time series of meridional wind at a certain point for four runs with a varied strength of forcing. The chosen point is at mid latitude ( $\lambda \approx 45^\circ$ ),  $90^\circ$  west of the substellar point, at the level  $\eta = 0.83$ , where the time series clearly show the different periodic oscillations that are characteristic of runs F1d (red line), F4b (green) and F4d (blue), and the stationary character of run F1b (black). . . . . 102

- 5.6 An oscillation cycle from run F4b\*. Each panel shows the temperature (colour) and flow (arrows) fields at a different time,  $t = \{89.1, 93.4, 96.0, 98.0\}\tau_p$ , with time increasing downward from panel to panel. . . . . 103
- 5.7 An oscillation cycle from run F1d\*. The temperature (colour) and flow (arrows) fields are shown at different times and heights. The panels show low (left column,  $\eta = 0.83$ ) and high (right column,  $\eta = 0.23$ ) altitude, at  $t = \{110.6, 113.1, 115.1, 117.7\}\tau_p$ , with time increasing downward from panel to panel. . . . 104
- 5.8 An oscillation cycle from run F4d\*. The temperature (colour) and flow (arrows) fields at the  $\eta = 0.83$  level are shown at different times. The panels show  $t = \{100.6, 101.1, 101.7\}\tau_p$ , with time increasing downward from panel to panel. . . . 105
- 5.9 Early response in run F4b\*. Geopotential (colour) and wind fields (arrows) are shown at the 30 mb (top) and 700 mb (bottom) pressure surfaces, at an early time,  $t = 0.9 \tau_p$ . 107
- 5.10 Total kinetic energy evolution of two runs that are identical apart from the initial condition. The four frames zoom in on different epochs. The black curve is for run F4cI, initialised with a small amount of noise, and the red curve is for run F4cII, started with a westward jet. After reaching the stage where both curves are flat, the total kinetic energy did not change for even longer than the last panel shows, and was still at the same value after more than 80000 planet rotations, when the simulation was stopped. . 109
- 5.11 Snapshots of temperature (colour) and flow (arrows) fields at various stages of run F4cI. The panels show low (left column,  $\eta = 0.83$ ) and high (right column,  $\eta = 0.23$ ) altitude, at  $t = \{40, 2700, 2900, 20000\}\tau_p$ , with time increasing downward. . . . . 111
- 5.12 Snapshots of temperature (colour) and flow (arrows) fields at various stages of run F4cII. The panels show low (left column,  $\eta = 0.83$ ) and high (right column,  $\eta = 0.23$ ) altitude, at  $t = \{40, 2700, 5000, 7000, 20000\}\tau_p$ , with time increasing downward. . . . . 113

- 
- 5.13 Snapshots of zonal wind (colour) and horizontal flow (arrows) fields at various stages of run F4cII. The panels all show the fields at  $\eta = 0.23$ , at  $t = \{40, 2700, 5000, 7000, 20000\}\tau_p$ , with time increasing downward. . . . . 114
- 5.14 Results from run F4d\*, at four successive times (100.0, 100.3, 100.6 and 100.9 planet rotations). The plots are centered at the substellar point, with the color scale showing vorticity. The flow is highly variable in time, with large scale vortices, or storms, moving and changing in cyclic fashion. . . . . 116
- 5.15 Power spectrum of temperature time series for a CEGP simulation. The red line shows the temperature at the substellar point and the blue line at the antistellar point. Both show temporal variability of various periods, but clearly identifiable dominant components. . . . . 117

# List of Tables

2.1	Measured and Estimated Planetary Parameters . . . . .	27
3.1	Physical Parameters . . . . .	42
3.2	Vertical Coordinate Coefficients . . . . .	44
3.3	Summary of Runs For Initial Condition Sensitivity . . . . .	46
4.1	List of Runs Discussed . . . . .	69
4.2	Summary of Runs for Time Filter Sensitivity. . . . .	82
5.1	Summary of Runs with Varied Forcing Strength . . . . .	94
5.2	Numerical Parameters for Runs with Varied Forcing Strength	94

# Chapter 1

## Introduction

### 1.1 Extrasolar Planets

Since the discovery of the first planet around a star other than the Sun nearly two decades ago, well over 500 planets have been found. The rate of discoveries has been rising and is expected to increase further in the coming years. The discovered planets have shown great diversity and unexpected features. Currently, there is a strong drive to characterise their atmospheres and assess the conditions possible on the planets. For the atmospheres, a variety of characteristics is expected with different rotation rates, planet-star distances, surface properties, eccentricities, planetary masses and sizes, for example. This wealth of observed planets presents an opportunity to apply and extend theories of planetary atmospheres, beyond the conditions observed for the planets of the Solar System. In addition, to help guide and interpret observations, understanding of the planets' atmospheric dynamics and circulations is crucial since they affect temperature distributions and observed spectra.

The first planets that were discovered outside the Solar System were found in 1991, orbiting the pulsar PSR B1257+12 [*Wolszczan and Frail*, 1992], using the method of pulsar timing. In 1995 the first planet orbiting another main-sequence star, 51 Pegasi, was detected by Michael Mayor and Didier Queloz using the radial velocity technique [*Mayor and Queloz*, 1995]. Most of the extrasolar planets have been observed either via the radial velocity method or the transit method. Other planets have been found via microlensing, direct imaging, or pulsar timing.

The radial velocity method has yielded the largest number of planets so far. Both the star and planet orbit the centre of mass of the star-planet system. Throughout an orbit the star's line-of-sight velocity will change periodically, causing a Doppler shift of stellar spectral lines. The blue- or red-shift is detectable, as long as the planet is massive and/or close enough to the star, and effects of stellar variability are not too large. The period of the Doppler fluctuations gives the orbital period of the planet, or its semi-major axis, and the shape of the radial velocity curve can give constraints on the orbital eccentricity. Furthermore, the product  $M_p \sin i$  can be determined, where  $M_p$  is the planetary mass, and  $i$  is the inclination of the orbital plane with respect to the plane of the sky. If  $i$  cannot be constrained,  $M_p \sin i$  gives a lower mass limit for the planet. The method is biased toward massive and close-in planets, around less active stars.

For characterisation of atmospheres, the most detailed constraints come from the transit method. During the primary transit, the planet moves in front of the stellar disc, as seen from an observer's perspective, and blocks some of the stellar light. If the viewing geometry is favourable (a system is seen nearly edge-on), and the star to planet size and brightness ratios are not too large, the resulting dip in the stellar light curve can be measured photometrically. From the shape of the dip, the inclination angle,  $i$ , can be inferred. Thus, by combination with the radial velocity method (which gives  $M_p \sin i$ ), the mass of the planet is determined. The technique also yields the ratio of the planet and star radii. So if the stellar radius is known, the size of the planet can be inferred. When the planet mass is available, the planets mean density can be obtained, which can roughly constrain the internal composition and gaseous or solid nature of the planet. Given the size and mass, the planet's surface gravity can also be estimated.

The first extrasolar planet observed in transit was HD209458b [*Charbonneau et al.*, 2000; *Henry et al.*, 2000]. Since that breakthrough, the Spitzer Space Telescope and the Hubble Space Telescope have been used for numerous transit measurements, along with ground based efforts. Furthermore, the ongoing space missions KEPLER and CoRoT, which were specifically designed to measure transits, have had many successes. To-day, well over a hundred transiting planets have been detected, in addition to a large sample of unconfirmed planet candidates.



### 1.1.1 Hot Jupiters

The first planet detected around a main-sequence star, 51 Pegasi b, orbits its star every four days, at only 0.052 AU. This is more than seven times closer to its star than Mercury to the Sun. The detection was surprising, since at the time planets were not expected at such close-in orbits in general. The temperature at such a distance from the star is so high that the material needed to assemble the core of a giant planet, cannot be found in a solid phase there. This implies an important role for migration processes in the evolution of the planet's orbit after its formation. Since the first discovery however, a large fraction of the extrasolar planets discovered have been found to orbit very close to the star, with roughly a third of them having a semi-major axis  $a \leq 0.1$  AU, or just within a few tens of stellar radii. In part this is due to a selection effect, but nevertheless it is apparent that planets on close-in orbits are not unusual.

The 'effective' temperature of a planet (if it radiates as a blackbody in radiative equilibrium) can be estimated as

$$T_{p,\text{eff}} = \hat{f} \sqrt{\frac{R_*}{a}} (1 - A_B)^{1/4} T_{*,\text{eff}} \quad (1.1)$$

where  $A_B$  is the bond albedo, i.e. the fraction of reflected radiation to total intercepted radiation, integrated over all wavelengths and directions,  $R_*$  is the radius of the star,  $a$  the orbital semi-major axis, and  $T_{*,\text{eff}}$  is the effective temperature of the star. The factor  $\hat{f}$  is  $(1/2)^{1/2}$  if the radiative energy flux is assumed to be distributed over the whole planet, but  $(1/2)^{1/4}$  if it is distributed over one hemisphere. The actual temperature can vary and depend on a number of additional factors, but this simple equation leads to typical effective temperature estimates in the range of 1000-2000 K, for the close-in giant planets that have been detected. A large part of them are roughly in a Jovian mass range, and have been loosely classified under the name 'hot Jupiters', due to their mass and temperature range. In this thesis they will usually be referred to as Close-in Extrasolar Giant Planets (CEGPs).

For the close-in planets, in cases where the orbital eccentricity is low, it is expected that tidal forces will cause the planet's spin and orbit to become locked into a 1:1 resonance [Goldreich and Soter, 1966; Rasio *et al.*, 1996; Lubow *et al.*, 1997]. Under the tidally locked condition the star

shines and heats perpetually on the same side of the planet, so the planet has a permanent day-side and night-side. This represents an ideal forcing configuration not present in the Solar System, where none of the planets have a 1:1 spin-orbit synchronisation. Thus, studying tidally locked planets offers an opportunity to broaden our knowledge of planetary atmospheres.

The eccentricity distribution of the exoplanets (when known) spans almost the full range between 0.0–1.0. However, most of the short period planets (i.e., with orbital periods less than about 6 days) have very nearly circularised orbits. This gives an indication that they are tidally synchronised as well, since tidal synchronisation is expected to occur faster than orbital circularisation [e.g., *Goldreich and Soter*, 1966; *Rasio et al.*, 1996].

If spin-orbit synchronisation can be assumed, the rotation rate of the planet can be inferred. The rotation rate is a crucial parameter for atmospheric dynamics studies that is otherwise unknown. In addition, since the close-in planets are more likely to transit their parent stars, several important physical properties and parameters can and have been obtained, such as the size, composition, albedo and temperature contrast between day- and night sides. Importantly, the measurements are repeatable due to the frequency of the transits for small orbits. For some of the CEGPs, such as HD 209458 b and HD 189733 b, a substantial amount of data has already been gathered during repeated observations, making them attractive targets for theoretical studies. Furthermore, atmospheric modelling efforts for these planets over the last years are beginning to offer opportunities for comparison between different models and approaches.

A few of the close-in planets detected have masses and sizes that indicate they should have a solid and/or ocean surface, and are in some ways more Earth-like. The study of gas giant atmospheres is in a sense simpler, since a solid or liquid surface introduces complications due to mechanical and thermal interactions with the atmosphere above. Results from studies of atmospheric dynamics of tidally-locked CEGPs should be useful when theories are extended to lighter planets that have a solid/liquid surface, with added complications, but are under a similar permanent day-night forcing condition. In this thesis the focus is on giant planets on non-eccentric, tidally synchronised orbits. In particular, the emphasis is on the

region of their atmospheres where most of the weather activity is expected to take place, and most of the observations are expected to originate.

## 1.2 Planetary Atmospheres

Solar system planetary atmospheres generally have dynamically active, stably stratified layers, where advective and radiative transport is important. This is expected for extrasolar planets as well. These layers are bounded at the top by the tenuous region where molecular diffusion starts to dominate over advection (the turbopause). At the bottom end, convection becomes the dominant mechanism of energy transport.

Vast amounts of energy are released during planetary accretion, resulting in hot interiors of giant planets, that can still be cooling off several Gyr after the formation. All the gas giants in the Solar System seem to have a heat flux from their interiors, although its origin may vary. In the optically thick interior the energy is expected to be carried by convection, with temperature and density profiles close to adiabatic. As opacities decrease higher up in the atmosphere, there will be a transition to radiative transport and suppression of convection. For the gas giants in the Solar System this radiative-convective boundary occurs in the region 0.1-1 bar, although it may occur deeper for the highly irradiated CEGPs [Guillot and Showman, 2002].

At the lower boundary of the radiative layers, the convection can provide a forcing mechanism, in the form of stirring. Forcing from the top end comes from the host star's radiation. Most of the incoming radiation is usually in the visible and ultraviolet range. Part of it is scattered, and if clouds are present, they may reflect some of the irradiation. The remaining part is absorbed by atmospheric gases and clouds, and then partly emitted at longer (usually infrared) wavelengths, either to be re-absorbed elsewhere in the atmosphere or lost to space. In addition to radiative transfer, dynamics and dissipation processes govern the distribution of energy and temperature within the active layer.

### 1.2.1 Constraints from Observations

Measurements of eclipses, both the transit (or primary eclipse) when the planet passes in front of the star from the observers viewpoint, and the occultation (or secondary eclipse) when the planet passes behind the star, can give information about the composition and temperature structure of the planetary atmosphere. During a transit, a small portion of the starlight will be filtered through the upper atmosphere of the planet, in the terminator region, where it is partially absorbed at certain wavelengths, giving a transmission spectrum of the planetary atmosphere. From the drop in flux during an occultation, when the planetary flux is blocked, the brightness temperature of the planet can be obtained at different wavelengths, giving an emission spectrum for the planet's dayside.

Given the large mass of CEGPs, they are expected to be composed mainly of an extensive hydrogen atmosphere, similar to Jupiter or Saturn. For the two CEGPs with the brightest host stars, HD 209458 b and HD 189733 b both transmission and emission spectra have been obtained. Spectral features have been interpreted to indicate the presence of sodium, water, methane, carbon monoxide and carbon dioxide [e.g. *Charbonneau et al.*, 2002; *Tinetti et al.*, 2007; *Grillmair et al.*, 2008; *Swain et al.*, 2008].

Direct detections of the infrared thermal flux from the planet's dayside have been obtained from occultation observations, e.g., for HD 209458 b [*Deming et al.*, 2005] and TrES-1 [*Charbonneau et al.*, 2005]. Some constraints have been placed on horizontal temperature contrasts between day and night sides. Light curves for HD 189733 b and HD 209458 b exhibit relatively modest ( $\sim 20\text{-}30\%$ ) differences between dayside and nightside brightness temperatures, which might suggest efficient redistribution of thermal energy from dayside to nightside [*Knutson et al.*, 2007, 2009; *Cowan et al.*, 2007]. On the other hand, Ups And b and HD 179949 b indicate larger day-night phase variations that suggests large day-night temperature differences [*Harrington et al.*, 2006; *Cowan et al.*, 2007]. *Knutson et al.* [2007] analysed the phase curve of HD 189733 b over half an orbital period of the planet to obtain the longitudinal dependence of its temperature, and found the maximum to be shifted eastward from the substellar point. *Crossfield et al.* [2010] reported an even larger ( $\sim 80^\circ$ ) eastward shift of the maximum for Ups And b. Measurements can also

potentially yield information about differences in composition with longitude.

Several observations have fuelled speculations about the vertical temperature structure of the atmospheres. Emission in excess of a blackbody spectrum between 4–8  $\mu\text{m}$  for some planets has been interpreted as indication of an inversion layer, where temperature increases with height [Burrows *et al.*, 2008; Fortney *et al.*, 2008]. Pressure-temperature profiles can be indirectly inferred from comparison of models and data, but they cannot be directly obtained without assumptions.

There are multiple examples of observations which do not agree between different epochs, and could possibly be an indication of time variability in the planetary atmospheres. Grillmair *et al.* [2008] report discrepancies in spectral features in emission between two epochs. Charbonneau *et al.* [2008] find spectral features in secondary eclipse that are inconsistent with measurements of Grillmair *et al.* [2007]. They also find a different eclipse depth from Knutson *et al.* [2007]. Sing *et al.* [2009] measure at two wavelengths during transit and claim they fail to reproduce the Swain *et al.* [2008] result of a water signature. And in Agol *et al.* [2010], six pairs of transits and eclipses of HD 189733 b are studied, resulting in constraints on variability of the dayside and nightside (up to 17 % with 68% confidence).

### 1.3 Previous Modelling Work

A variety of two-dimensional (2-D) and three-dimensional (3-D) models have been used to study the atmospheric circulation of CEGPs. Cho *et al.* [2003, 2008] performed high-resolution, global simulations for CEGPs on circular orbits, using a pseudospectral model to solve the one-layer equivalent barotropic equations. These equations are a vertically integrated version of the primitive equations, which are used in this thesis, and introduced in Section 2.1. In Cho *et al.* [2003, 2008], the layer is forced with a large-scale deflection of the lower bounding surface to represent heating/cooling in the adiabatic limit. They considered HD 209458 b as a paradigm planet and although a variety of outcomes is possible, the flow is typically characterised by few broad east-west jets and dynamic polar

vortices.

*Showman and Guillot* [2002]; *Cooper and Showman* [2005, 2006]; *Showman et al.* [2008a] and *Rauscher and Menou* [2010] performed global simulations with the 3D primitive equations. The dayside heating and nightside cooling was parameterised with a Newtonian heating/cooling scheme, but in *Showman et al.* [2009] the forcing is represented in a non-gray, cloud-free radiative transfer scheme with opacities calculated assuming local chemical equilibrium. Although the models differ, they emphasise a dominant, broad, eastward equatorial jet reaching very high wind speeds (up to several km/s), in all their simulations, which show little variability in time.

*Dobbs-Dixon and Lin* [2008] performed simulations with the full Navier-Stokes equations in a limited-area domain, where the polar regions are cut off, using a flux-limited diffusion scheme for radiative processes. A few other approaches have been taken, such as the shallow-water and 2D studies of *Langton and Laughlin* [2007, 2008].

## 1.4 Outline of the Thesis

The outline of this thesis is as follows. In the next chapter, the equations that are used in this thesis to model the atmospheres of CEGPs are presented, as well as the numerical model used. Chapter 3 contains an investigation of the effects of initial conditions on the CEGP atmospheric simulations. This work has been published in *Thrastarson and Cho* [2010]. In Chapter 4 the relation between forcing and numerical dissipation of different origins is explored. The results of this study have also been published in *Thrastarson and Cho* [2011]. Building on the foundation set by the results described in these chapters, discernible coherent states obtained in simulations with a varied strength of forcing, as well as the multiple long-lasting states observed for a given forcing, are discussed in Chapter 5. That chapter also contains a discussion of the large-scale dynamic vortices that are a common feature of the simulations contained in this thesis, and their associated time variability. Chapter 6 is the conclusion, which includes an outlook for future work.

## Chapter 2

# Governing Equations and Numerical Model

### 2.1 The Primitive Equations

A compressible fluid obeys the mass continuity equation, describing mass conservation. Using general coordinates, the continuity equation is

$$\frac{D\rho}{Dt} + \rho \nabla \cdot \mathbf{u} = 0 \quad (2.1)$$

where  $\rho$  is the density,  $\mathbf{u}(\mathbf{x}, t)$  is the three-dimensional (3-D) velocity,  $\nabla$  is the 3-D gradient operator,  $\mathbf{x}$  is 3-D position,  $t$  is time, and  $D/Dt = \partial/\partial t + \mathbf{u} \cdot \nabla$  is the material derivative, following the motion of a fluid element of constant mass. Newton's second law of motion, describing how the velocity (or momentum) of the fluid responds to internal and imposed forces, is:

$$\frac{D\mathbf{u}}{Dt} = -\frac{1}{\rho} \nabla p + \mathbf{F}_f, \quad (2.2)$$

where  $p$  is pressure and  $\mathbf{F}_f$  represents viscous and body forces per unit mass. Together with an equation of state, relating  $\rho$  and  $p$ , these equations are generally referred to as the Navier-Stokes equations, when  $\mathbf{F}_f$  includes viscous forces, and as the Euler equations otherwise.

The equations that describe the 3-D dynamics of a thin (relative to the planet size) atmospheric layer are the *primitive equations* (PE) [e.g. Vallis, 2006; Holton, 2004]. They can be derived from the Navier-Stokes

equations for a reference frame rotating with the planet in spherical coordinates. For the derivation, the “shallow atmosphere” approximation and the “traditional approximation” are made. In its full form, the PE include the continuity equation, the momentum equation, and the equation of temperature (related to the thermodynamic variables by the equation of state) – along with appropriate boundary conditions and forcing. Given an initial state, the PE evolve the set of fluid quantities, {velocity  $\mathbf{u}$ , density  $\rho$ , temperature  $T$ , pressure  $p$ }, in time.

By switching from an inertial frame of reference to a frame rotating with the planet, the apparent forces of the Coriolis force, due to the rotation, and the centrifugal force, are introduced to the equations. When set in spherical coordinates,  $\lambda$  (longitude),  $\phi$  (latitude),  $r$  (radial distance), additional terms appear in the equations since the directions of the coordinate axes change with position on the sphere. These terms are often called metric and curvature terms.

In the shallow atmosphere approximation, it is assumed that the height of the atmosphere,  $z_{\max}$ , is small compared to the planetary radius  $R_p$  – i.e.,  $z \ll R_p$ , where  $r = R_p + z$ . In the traditional approximation the Coriolis and metric terms involving vertical velocity in the horizontal momentum equations are ignored. The hydrostatic approximation limits the frequency of the vertical motion to that below the acoustic frequency. Equivalently, the vertical length scale of motions is small compared to the horizontal length scale.

The continuity equation in the spherical coordinates now reads

$$\frac{D\rho}{Dt} + \rho \nabla \cdot \mathbf{u} = 0, \quad (2.3)$$

but with the material derivative,

$$\frac{D}{Dt} = \frac{\partial}{\partial t} + \frac{u}{R_p \cos \phi} \frac{\partial}{\partial \lambda} + \frac{v}{R_p} \frac{\partial}{\partial \phi} + w \frac{\partial}{\partial z}, \quad (2.4)$$

where  $(u, v, w)$  are the  $(\lambda, \phi, z)$  components of the velocity. The momentum equation for the longitudinal (eastward) velocity component is

$$\frac{Du}{Dt} - (2\Omega \sin \phi)v - \frac{uv}{R_p} \tan \phi = -\frac{1}{\rho R_p \cos \phi} \frac{\partial p}{\partial \lambda} + F_u, \quad (2.5)$$



where  $\Omega$  is the rotation rate. For the latitudinal (northward) velocity component,

$$\frac{Dv}{Dt} + (2\Omega \sin\phi)u + \frac{u^2}{R_p} \tan\phi = -\frac{1}{\rho R_p} \frac{\partial p}{\partial \phi} + F_v \quad (2.6)$$

$F_u$  and  $F_v$  represent momentum sinks due to viscous dissipation in the longitudinal and latitudinal directions, respectively, as well as momentum sources. On the left hand side of Equations (2.5, 2.6) the second term is due to the Coriolis force, and the third term is a metric term. In the vertical direction, hydrostatic equilibrium is assumed, so

$$\frac{\partial p}{\partial z} = -\rho g, \quad (2.7)$$

where  $g$  is the effective acceleration of gravity, which includes the contribution from the centrifugal acceleration.

The first law of thermodynamics, describes the conservation of energy. Assuming constant composition, it states that the internal energy of a body may change because of work done by or on it, or because of heat input. Applied to a moving fluid element,

$$c_p \frac{DT}{Dt} - \frac{1}{\rho} \frac{Dp}{Dt} = \dot{q}_{\text{net}}, \quad (2.8)$$

where  $c_p$  is the specific heat at constant pressure and  $\dot{q}_{\text{net}}$  is the heating rate, which can include radiative and conductive heating.

To close the system of equations, an equation of state is needed, relating the thermodynamic variables,  $T$ ,  $p$  and  $\rho$ . Assuming an ideal gas, with constant chemical composition, the equation of state is

$$p = \rho RT \quad (2.9)$$

where  $R$  is the specific gas constant.

In the work described herein, the primitive equations are formulated and solved using a generalised pressure coordinate,  $\eta$ , in the vertical direction, as described in Section 2.3. A suitable set of boundary conditions, used here, is  $D\eta/Dt = 0$  at the top and bottom  $\eta$ -surfaces. Hence, the boundaries are material surfaces and no mass flow is allowed to cross the boundaries. With these boundary conditions, the equations admit the full range of motions for a stably-stratified atmosphere – except for vertically propagating sound waves.

As long as the continuum hypothesis is valid, i.e., that the characteristic length scale is much larger than the mean free path of the constituents that make up the atmosphere, the neutral atmosphere is well described by Eqs. (2.3-2.9). Since close-in extrasolar planets are subject to intense ionising radiation from their host stars, significant ionisation levels may be reached quite deep in their atmospheres, and even affect the circulation in the traditionally-assumed neutral, radiative layer [Koskinen *et al.*, 2010]. However, the possible effects of magnetic fields are not considered in this thesis.

## 2.2 Dynamical Regime

HD209458b and HD189733b are two of the most studied CEGPs, with a relatively large amount of data now measured for them. They are taken here as ‘paradigm’ planets, typical for the sample of CEGPs. In Table 2.1, measured or estimated values of some planetary parameters of HD209458b and HD189733b are listed, along with the values for Jupiter and Saturn, for comparison.

An obvious difference between the Solar System gas giants and the CEGPs is the amount of radiative energy flux received. The flux received by HD 209458 b (globally averaged) is on the order of  $10^4$  times greater than what Jupiter receives. The enormous heating can lead to temperatures well over a thousand degrees. If a Jupiter-like value is taken for the albedo, and the flux is assumed to be distributed over the whole globe, one obtains an effective temperature of  $\sim 1300$  K for HD 209458b, compared to only  $\sim 100$  K for Jupiter.

Whereas the time scale for radiative processes on Jupiter is on the order of years, the high temperature on the close-in extrasolar giants can lead to much shorter radiative time scales (on the order of days), and a more prominent role for radiative processes and their interaction with dynamical processes. At a local pressure,  $p$ , and temperature,  $T$ , the radiative time scale can be roughly estimated as [e.g., Showman and Guillot, 2002]:

$$\tau_{\text{th}} \sim \frac{c_p p}{4\sigma g T^3}, \quad (2.10)$$

where  $c_p$  is the specific heat at constant pressure,  $g$  is the gravitational

Table 2.1: Measured and Estimated Planetary Parameters

Parameter	Units	HD 209458b	HD 189733b	Jupiter	Saturn
$M_p$	$M_{\text{Jup}}$	0.69	1.14	1.00	0.30
$R_p$	$10^7 \text{ m}$	10.0	8.1	7.0	6.0
$a$	AU	0.05	0.03	5.2	9.6
$e$		0.014	0.004	0.049	0.057
$P$	days	3.5	2.2	4333	10759
$\Omega$	$10^{-5} \text{ s}^{-1}$	2.1	3.3	16	18
$g$	$\text{m s}^{-2}$	8.7	22.3	25.9	10.9
$T_{p,\text{eff}}$	K	1300	1100	110	80
$H_p$	km	500	200	27	60
$Ro$		0.03-0.3	0.03-0.3	0.003	0.01
$L_\beta$	$\pi R_p$	0.8	0.7	0.07	0.14

Notes: The planetary mass,  $M_p$  (in Jupiter masses), radius  $R_p$ , and surface gravity,  $g$ , as well as the orbital semi-major axis,  $a$ , eccentricity,  $e$ , and period,  $P$ , are all based on observations. The astronomical unit is  $\text{AU} = 1.496 \cdot 10^{11} \text{ m}$ . To obtain the rotation rate,  $\Omega$ , for the extrasolar planets, 1:1 spin-orbit synchronisation is assumed. The effective temperature of the planets,  $T_{p,\text{eff}}$ , is only a rough estimate obtained using Equation (1.1) with an assumed albedo of 0.3 and  $\hat{f} = (1/2)^{1/2}$ , for the extrasolar planets. A crude estimate for the pressure scale height is obtained from  $H_p = RT/g$ , using the estimated globally averaged effective temperature and  $R = 3500 \text{ J kg}^{-1}\text{K}^{-1}$  for the extrasolar planets. The Rossby number,  $Ro$  (Eq'n. 2.11), and Rhines scale,  $L_\beta$  (Eq'n. 2.14), are the values at  $45^\circ$  latitude, with  $L = R_p$  and  $U$  in the range 100–1000 m/s for the extrasolar planets, 40 m/s for Jupiter and 150 m/s for Saturn. Observed values are obtained from the Extrasolar Planet Encyclopaedia, <http://exoplanet.eu>, and NASA Planetary Factsheets, <http://nssdc.gsfc.nasa.gov/planetary/planetfact.html>.

acceleration, and  $\sigma = 5.67 \times 10^{-8} \text{ W m}^{-2} \text{ K}^{-4}$  is the Stefan-Boltzmann constant. As an example, using estimated values for HD 209458 b of  $c_p = 12300 \text{ J kg}^{-1} \text{ K}^{-1}$ ,  $g = 8.7 \text{ m s}^{-1}$  (see Table 2.1), and  $T_{p,\text{eff}} = 1300 \text{ K}$  for the temperature, the above equation for the radiative time scale gives  $\tau_{\text{th}} \sim 80 \text{ h}$  at the 1 bar pressure level.

Another potential source of difference between the CEGPs and the Solar System gas giants lies in their rotation rates. If CEGPs can be assumed spin-orbit synchronised, their implied rotation periods are a few Earth days ( $\sim 50$ – $100$  hours). Under this assumption, they are rotating much slower than Jupiter or Saturn, which both have close to 10-hour rotation periods. The relative importance of rotation can be estimated by a scale analysis on the horizontal equations of motion, Eqs. (2.5 and 2.6). If the horizontal length scale of the motions considered is  $L$ , and a representative wind speed is  $U$ , then the order of magnitude of the advective term is  $U^2/L$ , while the Coriolis term scales as  $fU$ , where  $f = 2\Omega \sin \phi$ . The ratio of the strength of the advection term to the Coriolis term is the Rossby number,

$$Ro = U/(fL). \quad (2.11)$$

For the Solar System giant planets, as well as Earth and Mars, typical values for  $Ro$  lie in the range 0.001–0.1.

As long as the horizontal length scale considered does not exceed the planetary radius, the order of the metric terms ( $U^2/R_p$ ) is the same or smaller than the advection term. When  $Ro \ll 1$ , the Coriolis terms dominate over the advection terms, and in the common case where the frictional term is weak, the Coriolis term is the only term that remains to balance against the pressure gradient term. This is geostrophic balance, where wind blows along isobars (lines of constant pressure) at a given height,

$$fu = -\frac{1}{R_p \rho} \frac{\partial p}{\partial \phi} \quad fv = \frac{1}{R_p \cos \phi \rho} \frac{\partial p}{\partial \lambda} \quad (2.12)$$

Taking the vertical derivative of the above equations, and using the ideal gas law and hydrostatic equilibrium, results in the thermal wind shear equations, that relate the vertical shear of horizontal wind to horizontal temperature gradients,

$$\frac{\partial u}{\partial z} = -\frac{g}{R_p f T} \frac{\partial T}{\partial \phi} \quad \frac{\partial v}{\partial z} = \frac{g}{R_p \cos \phi f T} \frac{\partial T}{\partial \lambda} \quad (2.13)$$

Geostrophy holds quite well in large regions of, e.g., Jupiter's, Saturn's and Earth's atmospheres. However, at the equator where  $f$  goes to 0, the geostrophic approximation breaks down.

The proper value for the order of wind speeds on the CEGPs is unknown. But if  $U$  is taken as 100–1000 m/s for global-scale flows with  $L = R_p$ , the Rossby number for HD209458 for instance is  $Ro \sim 0.03$ –0.3 at mid-latitudes. For smaller scales, faster winds or higher latitudes, the Rossby number can approach or exceed 1. Bearing in mind the caveats of a simple scaling analysis, it appears that the CEGPs may be in a regime where Coriolis forces are not as strong as on Jupiter or Saturn, but still play a significant role, and geostrophy may hold in some regions of their atmospheres.

A prominent feature of the atmospheric circulation of all the Solar System giant planets is the presence of zonal (east-west) jet streams. A potential explanation of this feature is offered by the Rhines mechanism [e.g., *Rhines*, 1975; *Williams*, 1978; *Cho and Polvani*, 1996; *Scott*, 2010]. In a turbulent fluid where the motion is mainly layer-wise or quasi-two-dimensional, energy cascades from small to large scales, with a corresponding growth of eddies by successive mergers. For a rotating sphere, the growth is anisotropic, since the Coriolis force provides a restoring force in the meridional direction, whereas in the zonal direction, eddies are free to grow to the largest scales, leading to zonal jets and bands. The meridional width of the bands can be roughly characterised by the Rhines scale,

$$L_\beta \equiv \pi(2U/\beta)^{1/2}, \quad (2.14)$$

where  $U$  is the characteristic wind speed of the jet, and  $\beta \equiv R_p^{-1}(\partial f / \partial \phi) = 2\Omega \cos \phi / R_p$ . The expected number of bands on a given planet can then be roughly estimated by  $n_{band} \sim \pi R_p / L_\beta$ , increasing with rotation rate.

Another length scale relevant to the morphology of atmospheric dynamical structures is the Rossby deformation radius. It can be thought of as the range over which flow structures can effectively interact, or the scale where pressure perturbations are resisted by the Coriolis force. Coherent vortices often have horizontal sizes near the deformation radius. It

is defined as

$$L_d \equiv NH/f, \quad (2.15)$$

thus depending on rotation rate and latitude through  $f$ , as well as the vertical scale of the flow,  $H$ , and the Brunt-Väisälä frequency,

$$N = \sqrt{\frac{g}{T} \left( \frac{\partial T}{\partial z} + \frac{g}{c_p} \right)}, \quad (2.16)$$

which is the frequency of buoyancy oscillations for an adiabatically displaced fluid parcel in a stably stratified atmosphere. If vertical temperature gradients can be assumed negligible compared to the dry adiabatic lapse rate,  $g/c_p$ , and the globally averaged  $T_{p,\text{eff}}$  is used as a crude estimate of the temperature, then using  $c_p = 12300 \text{ J kg}^{-1} \text{ K}^{-1}$  for the specific heat, gives  $N \sim 2 \times 10^{-3} \text{ s}^{-1}$ , or a buoyancy oscillation period on the order of an hour. A positive vertical temperature gradient would lead to higher  $N$ , or stronger stratification, while a negative vertical temperature gradient would lead to weaker stratification, and static instability if  $\partial T/\partial z < -g/c_p$ .

On Jupiter and Saturn  $L_\beta$  and  $L_d$  are small compared to the planetary radius. Their atmospheres exhibit a large number ( $\sim 10$ – $20$ ) of jets and vortices with horizontal sizes that are only a fraction of  $R_p$ . On Uranus and Neptune the ratios  $L_\beta/R_p$  and  $L_d/R_p$  are larger, coinciding with a smaller number of jets ( $\sim 3$ ). To get a rough estimate for  $L_d$  on HD209458b, using the scale height  $H_p$  from table 2.1 as a measure of the vertical flow scale, and  $N \sim 2 \times 10^{-3} \text{ s}^{-1}$  for the buoyancy frequency, results in a value on the order of the planetary radius for mid-latitudes. It has been argued that on many of the relatively slowly rotating CEGPs,  $L_\beta$  and  $L_d$  are expected to be comparable to  $R_p$ , and so their dominant flow structures could plausibly be expected to be planetary in scale [e.g., *Menou et al.*, 2003; *Cho et al.*, 2003], unlike Jupiter and Saturn.

## 2.3 General Circulation Model

The primitive equations are nonlinear and describe motions with many degrees of freedom. Thus, they are difficult to solve analytically, but they

can be solved numerically in an approximate way. In the work described in the following chapters, the Community Atmosphere Model (CAM) is used to numerically solve the primitive equations. CAM is a well-tested, highly-accurate, state-of-the-art General Circulation Model (GCM) developed by the National Center for Atmospheric Research (NCAR) for the atmospheric research community [Collins *et al.*, 2004]. A pseudospectral method is used for the horizontal representation of the equations, while in the vertical direction, a finite differencing method is used. The time-stepping is done using a semi-implicit, second-order leapfrog scheme. The full model has been extensively used for simulations of the Earth's climate and contains representations of many physical and chemical processes, such as cloud formation and land-air-ocean interactions. However, here only the dynamical core of the model is used, with Newtonian relaxation to represent effects of thermal/radiative processes. The primitive equations are solved in a form, modified from Equations (2.3-2.9), which is described below.

### 2.3.1 The CAM Equations in Continuous Form

The vertical coordinate system used in CAM, is a hybrid between a pure pressure coordinate and a surface pressure based (sigma) coordinate [Simmons and Struving, 1981; Kasahara, 1974]. The characteristics of the latter are useful when variations in the bottom boundary, caused by static or dynamic conditions, are not small. The generalised vertical coordinate,  $\eta$ , is defined implicitly through the relation

$$p(\lambda, \phi, \eta, t) = A(\eta)p_r + B(\eta)p_s(\lambda, \phi, t), \quad (2.17)$$

where  $p_r$  is a constant reference pressure and  $p_s(\lambda, \phi, t)$  is a deformable pressure surface at the bottom boundary. A set of levels  $\eta_k$  is then specified by  $A_k, B_k \in [0, 1]$ , such that  $\eta_k \equiv A_k + B_k$ . The coordinate  $\eta(p, p_s)$  is a monotonic function of pressure, which reduces to a pure pressure coordinate at the top, and a pure sigma (surface pressure based) coordinate at the bottom of the domain, satisfying the conditions

$$\eta(p_s, p_s) = 1, \quad \eta(0, p_s) = 0, \quad \eta(p_t, p_s) = \eta_t, \quad (2.18)$$

where  $p_t$  is the constant pressure at the top of the model. The material derivative following a fluid parcel in the  $(\lambda, \phi, \eta)$ -coordinate system is:

$$\frac{D}{Dt} = \frac{\partial}{\partial t} + \mathbf{v} \cdot \nabla_\eta + \dot{\eta} \frac{\partial}{\partial \eta}, \quad (2.19)$$

where  $\mathbf{v} = (u, v, 0)$  is the horizontal velocity,

$$\nabla_\eta = \left( \frac{1}{R_p \cos \phi} \frac{\partial}{\partial \lambda}, \frac{1}{R_p} \frac{\partial}{\partial \phi}, 0 \right) \quad (2.20)$$

is the gradient on a constant  $\eta$ -surface, and  $\dot{\eta} = D\eta/Dt$ . The boundary conditions at the bottom and top of the domain are:

$$\dot{\eta}(p_s, p_s) = 0, \quad (2.21)$$

$$\dot{\eta}(p_t, p_s) = \omega(p_t) = 0 \quad (2.22)$$

where  $\omega = Dp/Dt$ , so the boundaries are material surfaces and no mass flow is allowed to cross them.

When the horizontal momentum equations (2.5 and 2.6) are written in the  $\eta$ -system, a  $\nabla_\eta z$  term is introduced. Writing this in terms of the geopotential  $\Phi = gz$ , using the equation of hydrostatic equilibrium (2.7), and using the ideal gas law (2.9) to eliminate  $\rho$ , the horizontal momentum equation can be written in the following vector form:

$$\frac{D\mathbf{v}}{Dt} + \mathbf{f} \times \mathbf{v} = -\nabla_\eta \Phi - \frac{RT}{p} \nabla_\eta p, \quad (2.23)$$

where  $\mathbf{f} = f\hat{\mathbf{k}}$ , with  $\hat{\mathbf{k}}$  the unit vector in the vertical direction, and explicit viscosity is ignored. The identity  $\nabla(\mathbf{v} \cdot \mathbf{v}) = 2(\mathbf{v} \cdot \nabla)\mathbf{v} + 2\mathbf{v} \times (\nabla \times \mathbf{v})$ , can be used to write

$$\frac{D\mathbf{v}}{Dt} = \frac{\partial \mathbf{v}}{\partial t} + \frac{1}{2} \nabla_\eta (\mathbf{v} \cdot \mathbf{v}) + \boldsymbol{\zeta} \times \mathbf{v} + \dot{\eta} \frac{\partial \mathbf{v}}{\partial \eta}, \quad (2.24)$$

where  $\boldsymbol{\zeta} = \zeta \hat{\mathbf{k}} = \nabla_\eta \times \mathbf{v}$  is the relative vorticity in the vertical direction. Applying the above relation to Equation (2.23) and taking the vertical component of the curl of the resulting equation, yields the vorticity equation:

$$\frac{\partial \zeta}{\partial t} = \mathbf{k} \cdot \nabla_\eta \times [-(\zeta + f)\mathbf{k} \times \mathbf{v} - \dot{\eta} \frac{\partial \mathbf{v}}{\partial \eta} - \frac{RT}{p} \nabla_\eta p] \quad (2.25)$$



Taking the divergence of Equation (2.23) yields the divergence equation:

$$\frac{\partial \delta}{\partial t} = \nabla_{\eta} \cdot [-(\zeta + f)\mathbf{k} \times \mathbf{v} - \dot{\eta} \frac{\partial \mathbf{v}}{\partial \eta} - \frac{RT}{p} \nabla_{\eta} p] + \nabla_{\eta}^2 (E + \Phi), \quad (2.26)$$

where  $\delta = \nabla \cdot \mathbf{v}$  is the divergence and  $E = (\mathbf{v} \cdot \mathbf{v})/2$ . The hydrostatic equation (2.7) can also be written in terms of the geopotential and the ideal gas law used to eliminate  $\rho$ . Integrating the resulting equation from the bottom surface ( $\eta = 1, p = p_s, \Phi = \Phi_s$ ) to an  $\eta$ -surface where the pressure is  $p(\eta)$ , a diagnostic equation for the geopotential is obtained:

$$\Phi = \Phi_s + R \int_{p(\eta)}^{p(\eta=1)} T d \ln p. \quad (2.27)$$

The geopotential at the bottom boundary is set to  $\Phi_s = 0$  in all the work contained in this thesis.

With the aid of the hydrostatic equation, the continuity equation (2.3) can be expressed in the  $\eta$ -coordinate system as

$$\frac{\partial}{\partial \eta} \left( \frac{\partial p}{\partial t} \right) + \nabla_{\eta} \cdot \left( \mathbf{v} \frac{\partial p}{\partial \eta} \right) + \frac{\partial}{\partial \eta} \left( \dot{\eta} \frac{\partial p}{\partial \eta} \right) = 0. \quad (2.28)$$

By integrating from the bottom boundary ( $\eta = 1, p = p_s$ ) to the top ( $\eta = \eta_t, p = p_t$ ), and using the boundary conditions  $\dot{\eta} = 0$  at both the top and the bottom, a prognostic equation is obtained for the surface pressure:

$$\frac{\partial p_s}{\partial t} = \int_1^{\eta_t} \nabla_{\eta} \cdot \left( \frac{\partial p}{\partial \eta} \mathbf{v} \right) d\eta \quad (2.29)$$

Integration of the continuity equation from  $\eta_t$  to  $\eta$  yields a diagnostic equation for  $\dot{\eta}$  via

$$\dot{\eta} \frac{\partial p}{\partial \eta} = -\frac{\partial p}{\partial t} - \int_{\eta_t}^{\eta} \nabla_{\eta} \cdot \left( \frac{\partial p}{\partial \eta} \mathbf{v} \right) d\eta. \quad (2.30)$$

The diagnostic equation for  $\omega$  is then:

$$\omega = \mathbf{v} \cdot \nabla_{\eta} p - \int_{\eta_t}^{\eta} \nabla_{\eta} \cdot \left( \frac{\partial p}{\partial \eta} \mathbf{v} \right) d\eta. \quad (2.31)$$

The thermodynamic equation (2.8) is rearranged, and the identity,  $\nabla \cdot (T\mathbf{v}) = (\nabla T) \cdot \mathbf{v} + T\delta$ , is used to rewrite  $DT/Dt$ , to obtain an evolution equation for temperature in the  $\eta$ -coordinate system:

$$\frac{\partial T}{\partial t} = -\nabla \cdot (T\mathbf{v}) - T\delta - \dot{\eta} \frac{\partial T}{\partial \eta} + \frac{RT\omega}{c_p p} + \frac{\dot{q}_{\text{net}}}{c_p} \quad (2.32)$$

Terms representing horizontal diffusion of momentum and temperature, are added to Equations (2.25), (2.26) and (2.32). They are applied in the form of “hyperdiffusion”,

$$\mathcal{D}_\chi = \nu_{2p} [(-1)^{p+1} \nabla^{2p} + \mathcal{C}] \chi, \quad (2.33)$$

where  $\chi = \{\zeta, \delta, T\}$  and  $\mathcal{C} = (2/R_p^2)^p$  is a correction term added to the vorticity and divergence equations to prevent damping of uniform rotations for angular momentum conservation. Unless stated otherwise, the  $p = 2$  case is used in the work described herein. The hyperdiffusion is added in each layer to prevent accumulation of power on the small, poorly-resolved scales and to stabilise the integration. However, the effects of various numerical dissipation are often subtle and can be significant on the integration, particularly over long times [e.g., *Dritschel et al.*, 2007]. These effects are discussed further in Chapter 4.

In the final formulation of the equations, some terms involving  $\mathbf{v}$  are represented in terms of the transformed velocity  $\mathbf{V} = (U, V) = (u, v) \cos \phi$ , where  $\phi$  is latitude, in order to avoid discontinuities at the poles. Also, the equations are formulated using  $\Pi = \ln(p_s)$  instead of  $p_s$  to avoid aliasing problems in the hydrostatic equation (2.27). The  $\ln(p)$  integral in the hydrostatic equation introduces a high order nonlinearity, which then enters into the divergence equation, but formulating the equations using  $\ln(p_s)$  results in the nonlinearity being only quadratic in the hydrostatic equation [Collins *et al.*, 2004]. With a few rearrangements and applications of the chain rule, as well as the above mentioned modifications, the final continuous form of the primitive equations solved in CAM, consists of the following four prognostic equations for the vorticity, divergence, (logarithm of) surface pressure, and temperature:

$$\frac{\partial \zeta}{\partial t} = \mathbf{k} \cdot \nabla_\eta \times (\mathbf{n} / \cos \phi) + \mathcal{D}_\zeta, \quad (2.34)$$

$$\frac{\partial \delta}{\partial t} = \nabla_\eta \cdot (\mathbf{n} / \cos \phi) + \nabla_\eta^2 (E + \Phi) + \mathcal{D}_\delta, \quad (2.35)$$

$$\frac{\partial \Pi}{\partial t} = - \int_{(\eta_t)}^{(1)} \mathbf{v} \cdot \nabla_\eta \Pi d\left(\frac{\partial p}{\partial p_s}\right) - \frac{1}{p_s} \int_{p(\eta_t)}^{p(1)} \delta dp, \quad (2.36)$$

$$\begin{aligned} \frac{\partial T}{\partial t} = & - \frac{1}{\cos \phi} \nabla_\eta \cdot (T \mathbf{V}) - T \delta - \dot{\eta} \frac{\partial p}{\partial \eta} \frac{\partial T}{\partial p} \\ & + \frac{RT\omega}{c_p p} + \frac{\dot{q}_{\text{net}}}{c_p} + \mathcal{D}_T, \end{aligned} \quad (2.37)$$

where

$$\mathbf{n} = -(\zeta + f)\mathbf{k} \times \mathbf{V} - \dot{\eta} \frac{\partial p}{\partial \eta} \frac{\partial \mathbf{V}}{\partial p} - \cos \phi \frac{RT p_s}{p} \frac{\partial p}{\partial p_s} \nabla_{\eta} \Pi. \quad (2.38)$$

In addition, the final form of the three diagnostic equations needed, for the geopotential and vertical velocities, is as follows:

$$\Phi = \Phi_s + R \int_{p(\eta)}^{p(1)} T d \ln p, \quad (2.39)$$

$$\begin{aligned} \dot{\eta} \frac{\partial p}{\partial \eta} = & \frac{\partial p}{\partial p_s} \left[ \int_{(\eta_t)}^{(1)} p_s \mathbf{v} \cdot \nabla_{\eta} \Pi d \left( \frac{\partial p}{\partial p_s} \right) + \int_{p(\eta_t)}^{p(\eta)} \delta dp \right] \\ & - \int_{(\eta_t)}^{(\eta)} p_s \mathbf{v} \cdot \nabla_{\eta} \Pi d \left( \frac{\partial p}{\partial p_s} \right) - \int_{p(\eta_t)}^{p(\eta)} \delta dp, \end{aligned} \quad (2.40)$$

$$\begin{aligned} \omega = & \frac{\partial p}{\partial p_s} p_s \mathbf{v} \cdot \nabla_{\eta} p_s \\ & - \int_{(\eta_t)}^{(\eta)} p_s \mathbf{v} \cdot \nabla_{\eta} \Pi d \left( \frac{\partial p}{\partial p_s} \right) - \int_{p(\eta_t)}^{p(\eta)} \delta dp. \end{aligned} \quad (2.41)$$

### 2.3.2 Physical Parameterisations

In the simulations described in this thesis, the diabatic term in Equation (2.32) is modelled with Newtonian relaxation. In this simple prescription the net heating rate takes the form

$$\frac{\dot{q}_{\text{net}}}{c_p} = -\frac{1}{\tau_{\text{th}}} (T - T_e), \quad (2.42)$$

where  $T_e$  is a prescribed “equilibrium” temperature distribution and  $\tau_{\text{th}}$  is a specified relaxation time. This form of heating/cooling is a crude representation of the effects of radiative processes on the large-scale dynamics. As a linear approximation to radiative heating/cooling it is strictly only valid for small deviations of the temperature from the equilibrium distribution [e.g., *Andrews et al.*, 1987; *Cho et al.*, 2008]. In reality the radiative processes and their interaction with dynamical processes can be highly non-linear. Even in cases where the linear approximation is valid, the equilibrium temperature distribution and radiative timescales are in general unknown for extrasolar planets, and can depend in a complicated way on the distribution of atmospheric constituents and clouds and their radiative properties. The approach taken here is to specify simple, idealised functions for  $T_e$  and treat  $\tau_{\text{th}}$  as a parameter that is varied.

The evolution of chemical constituents (such as water vapour) has not been included in the simulations, even if an additional evolution equation for moisture, as well as its coupling with the other equations, is implemented in the full version of CAM. Thus, there is no representation of chemical reactions, and formation of clouds or their direct effects are not considered explicitly. The levels of uncertainty related to clouds, are large even for models of the Earth. Finding ways to represent and explore their effects on extrasolar planets in a meaningful way in a GCM, is a vast research project in itself. And in any case, gaining an understanding of the general circulation without cloud representation is an obvious and necessary first step, before the inclusion of such complications becomes amenable.

Unresolved gravity waves may play an important role on CEGPs [Watkins and Cho, 2010], but no parameterisation of their effects is included here. It is not clear yet, how to properly include these effects on the larger, resolved scales, but that is regarded here as an important future prospect. Sometimes GCMs include parameterisations of processes such as vertical diffusion to represent turbulent kinetic energy losses by small-scale shear instabilities and breaking waves. In general, there can be additional terms in the momentum and energy equations, due to other dissipative processes, but these are generally not included here.

### 2.3.3 Numerical Methods

The system described by Equations (2.34-2.41), with the boundary conditions (2.21-2.22), is integrated forward in time using a semi-implicit leapfrog scheme, with the exception of the horizontal diffusion terms. In the semi-implicit formulation, variables are expanded about a reference state, such that

$$\chi = \chi^r + \chi', \quad (2.43)$$

where the  $r$  superscript refers to a reference state and the prime refers to a deviation from that, for a general variable. Using this expansion in the equations, they are split into parts that are either linear or non-linear in the primed quantities. The linear parts are treated implicitly by averaging the previous and next timesteps. The non-linear parts on the other hand

are treated explicitly, using centred finite differences. A Robert-Asselin time filter [Robert, 1966; Asselin, 1972], whose strength is determined by the coefficient  $\epsilon$ , is applied at every timestep in each layer to stabilise the integration. Finite differences are also used in the vertical direction, on a grid of  $\eta$ -levels. In constructing the vertical finite differences, the requirement is imposed that the global integral of total energy is conserved, in the absence of sources and sinks [Simmons and Strufing, 1981].

For the horizontal discretisation, a pseudospectral method is used. In the model, horizontal derivatives and linear operations are performed in spectral space, while physical parameterisations and nonlinear operations are generally carried out in grid-point space. The horizontal representation of an arbitrary scalar quantity  $\xi$  (such as  $\zeta$ ,  $\delta$  or  $T$ ) in the spherical geometry, consists of a truncated series of spherical harmonics,

$$\xi(\lambda, \mu) = \sum_{m=0}^M \sum_{n=|m|}^{N(m)} \xi_n^m P_n^m(\mu) e^{im\lambda},$$

where  $m$  is the sectoral (or longitudinal) wavenumber;  $M$  is the highest sectoral wavenumber included;  $N(m)$  is the highest degree of the associated Legendre functions  $P_n^m$ ;  $\lambda$  is the longitude; and,  $\mu \equiv \sin \phi$ . The spherical harmonic functions,

$$Y_n^m(\lambda, \mu) = P_n^m(\mu) e^{im\lambda}, \quad (2.44)$$

used in the spectral expansion are the eigenfunctions of the Laplacian operator in spherical coordinates. The Legendre functions are normalised such that

$$\int_{-1}^1 [P_n^m(\mu)]^2 d\mu = 1. \quad (2.45)$$

The coefficients  $\xi_n^m$  are given by

$$\xi_n^m = \int_{-1}^1 \frac{1}{2\pi} \int_0^{2\pi} \xi(\lambda, \mu) e^{-im\lambda} d\lambda P_n^m(\mu) d\mu. \quad (2.46)$$

Here, the inner integral is a Fourier transform which is performed by a Fast Fourier Transform (FFT) subroutine. The outer integral is performed via Gaussian quadrature on a Gaussian grid,

$$\xi_n^m = \sum_{j=1}^J \xi^m(\mu_j) P_n^m(\mu_j) w_j, \quad (2.47)$$

where  $J$  is the number of Gaussian grid points from pole to pole, and  $\mu_j$  are the Gaussian grid points in the meridional direction. These points are given by the roots of  $P_J(\mu)$ , with the corresponding Gaussian weight at each point given by

$$w_j = \frac{2(1 - \mu_j^2)}{[JP_{J-1}(\mu_j)]^2}, \quad (2.48)$$

satisfying the condition

$$\sum_{j=1}^J w_j = 2.0. \quad (2.49)$$

Starting from grid-point values at time  $t$ , the methods described above are applied, with a given resolution in space and time, to solve Equations (2.34-2.41), including transformations from grid-space to spectral space and back, to arrive at forecasted values at time  $t + \Delta t$ , where  $\Delta t$  is the timestep. To ensure conservation of total mass and energy, ad-hoc mass and energy fixers are implemented. Thus, the total mass and energy is calculated after each time step, and correction factors applied to keep a constant value. However, these features are generally turned off in the calculations described here. Chapter 4 contains further details of the numerical methods used, and a discussion of some of their effects and limitations.

# Chapter 3

## Effects of Initial Conditions

A general circulation model is used to study the three-dimensional (3-D) flow and temperature distributions of atmospheres on tidally synchronised extrasolar planets. In this work, the focus is on the sensitivity of the evolution to the initial flow state, which has not received much attention in 3-D modelling studies. It is found that different initial states lead to markedly different distributions—even under the application of strong forcing (large day-night temperature difference with a short “thermal relaxation time”) that may be representative of close-in planets. This is in contrast with the results or assumptions of many published studies. In general, coherent jets and vortices (and their associated temperature distributions) characterise the flow, and they evolve differently in time, depending on the initial condition. If the coherent structures reach a quasi-stationary state, their spatial locations still vary. The result underlines the fact that circulation models are currently unsuitable for making quantitative predictions (e.g., location and size of a “hot spot”) without better constrained, and well posed, initial conditions.

### 3.1 Introduction

Understanding the flow dynamics of atmospheres is crucial for characterising extrasolar planets. Dynamics strongly influence the temperature distribution as well as the spectroscopic behaviour. An essential tool for studying dynamics on the large-scale is a global hydrodynamics model. Many studies have used such a model [e.g., *Showman and Guillot*, 2002;

*Cho et al.*, 2003; *Cooper and Showman*, 2005; *Langton and Laughlin*, 2007; *Cho et al.*, 2008; *Dobbs-Dixon and Lin*, 2008; *Showman et al.*, 2008a; *Menou and Rauscher*, 2009]. The models in these studies numerically solve a set of non-linear partial differential equations for the evolution of a fluid on a rotating sphere. Hence, the initial condition (as well as the boundary conditions) needs to be specified.

Presently, physically accurate and mathematically well-posed initial conditions for the models are not known for extrasolar planets. Unlike for the solar system planets, dynamically “balanced” initial data<sup>1</sup> are not available and dominant dynamical processes, such as baroclinic instability and geostrophic turbulence, are not yet understood for the extrasolar planets [*Cho et al.*, 2003, 2008; *Showman et al.*, 2008b; *Cho*, 2008]. Concerning initialization, there is a long history of research in geophysical fluid dynamics and numerical weather prediction, and it is still a subject of active research—even for the Earth [*Holton*, 2004].

In most simulations of close-in planets performed so far, the initial state is either at rest or with a small, randomly perturbed wind field to break the flow symmetry [*Cooper and Showman*, 2005; *Langton and Laughlin*, 2007; *Dobbs-Dixon and Lin*, 2008; *Showman et al.*, 2008a; *Menou and Rauscher*, 2009]. *Cho et al.* [2008] initialise their two-dimensional simulations with random eddies, and variations of the initial velocity distributions are studied. They find significant differences in the flow evolution, depending on the vigour of the eddies. On the other hand, *Cooper and Showman* [2005] report on a three-dimensional (3-D) simulation, set up with an initial retrograde equatorial jet, and find no qualitative difference, compared with one starting from a rest state. *Showman et al.* [2008b] and *Cho* [2008] give summaries of the various results.

In this work, runs from the advanced 3-D general circulation model, CAM, are presented. As in *Cooper and Showman* [2005], as well as in *Showman et al.* [2008a] and *Menou and Rauscher* [2009], the model used in this work solves the full primitive equations [e.g., *Pedlosky*, 1987]. However, there are some important assets in the model used in this work (see section 3.2), compared with most models used so far. For example,

---

<sup>1</sup>self-consistent set of fields which does not lead to excessive noise and deviations from accurate prediction



it uses a parallel pseudospectral algorithm [Orszag, 1970; Eliassen *et al.*, 1988; Canuto *et al.*, 1988] with better-controlled, less invasive numerical viscosity. In this regard, our model is similar to the one used by Menou and Rauscher [2009].

With the model, I focus on the sensitivity of the flow evolution to the initial state. The sensitivity has not been much emphasised in previous studies, particularly in those using 3-D circulation models. In order to unambiguously delineate the sensitivity effect, the simulations are set up in a manner similar to previous studies, idealised forcing is applied (in many cases unencumbered by a vertical variation), and runs with all parameters identical—except for the initial condition—are compared.

The basic plan of the chapter is as follows. The setup for the simulations is described in section 3.2, where I endeavour to provide enough details to facilitate reproduction of the results. In section 3.3 I present the results of simulations initialised with different organised large-scale flow patterns, including the rest state. In this section, it is also shown how sensitive the flow is to small perturbations in the initial wind field. I conclude in section 3.4, summarising this work and discussing its implications for close-in extrasolar planet circulation modelling work.

## 3.2 Method

The global dynamics of a shallow, 3-D atmospheric layer is governed by the primitive equations [e.g., Pedlosky, 1987; Holton, 2004]. Here, by “shallow” it is meant that the thickness of the atmosphere under consideration is small compared to the planetary radius  $R_p$ . The primitive equations are solved in the form presented in Chapter 2, given by Equations (2.34-2.41), along with the boundary conditions (2.22-2.21).

To solve the primitive equations in the spherical geometry, the Community Atmosphere Model (CAM 3.0) is used. As described in Section 2.3 this includes a pseudospectral algorithm for the horizontal direction, finite differences in the vertical, and a semi-implicit leapfrog scheme for the timestepping. Superviscosity ( $\nabla^4$  operators), as well as a small Robert-Asselin time filter  $\epsilon$  [Robert, 1966; Asselin, 1972], are applied at every timestep in each layer to stabilise the integration.

Table 3.1: Physical Parameters

Parameter	Symbol	Value	Unit
Planetary rotation rate	$\Omega$	$2.1 \times 10^{-5}$	$\text{s}^{-1}$
Planetary radius	$R_p$	$10^8$	m
Gravity	$g$	10	$\text{m s}^{-2}$
Specific heat at constant pressure	$c_p$	$1.23 \times 10^4$	$\text{J kg}^{-1} \text{K}^{-1}$
Specific gas constant	$R$	$3.5 \times 10^3$	$\text{J kg}^{-1} \text{K}^{-1}$
Mean equilibrium temperature	$T_m$	1400	K
Equilibrium substellar temperature	$T_D$	1900	K
Equilibrium antistellar temperature	$T_N$	900	K
Initial temperature	$T_0$	1400	K

In all the simulations discussed in this chapter, the physical parameters chosen are based on the close-in extrasolar planet, HD209458b. The basic result presented—that the evolution depends on the initial flow state—does not change for a different close-in planet. The physical parameters for the model HD209458b planet are listed in Table 3.1.

CAM is able to include radiatively-active species and their coupling to the dynamics. However, they are not included in the present work so that the effects discussed are not obfuscated by complications unrelated to the essential result. Our principle motivation is to study the dependence on the initial flow in the most unambiguous way possible. To this end, the flow is forced using the simple Newtonian relaxation/drag formalism, as in many previous studies of extrasolar planet atmospheres [e.g., *Cooper and Showman*, 2005; *Langton and Laughlin*, 2007; *Showman et al.*, 2008a; *Menou and Rauscher*, 2009]. This drag is a simple representation of the net heating term in the energy equation (2.32):

$$\frac{\dot{q}_{\text{net}}}{c_p} = -\frac{1}{\tau_{\text{th}}} (T - T_e), \quad (3.1)$$

where  $T_e = T_e(\lambda, \phi, \eta, t)$  is the “equilibrium” temperature distribution and  $\tau_{\text{th}}$  is the thermal relaxation time constant.

In this work, both  $T_e$  and  $\tau_{\text{th}}$  are prescribed and height-independent ( $\partial/\partial\eta = 0$ ) and steady ( $\partial/\partial t = 0$ ), although simulations relaxing these restrictions have been run to verify robustness of our results. In general,

both  $T_e$  and  $\tau_{\text{th}}$  are (as are  $R$  and  $c_p$ ) complicated functions of space and time [Choi *et al.*, 2008]. Here,

$$T_e = T_m + \Delta T_e \cos \phi \cos \lambda, \quad (3.2)$$

where  $T_m = (T_D + T_N)/2$  and  $\Delta T_e = (T_D - T_N)/2$ , and  $T_D$  and  $T_N$  are the maximum and minimum temperatures at the day and night sides, respectively. Most of the simulations described in this chapter have  $T_D = 1900$  K,  $T_N = 900$  K, and  $\tau_{\text{th}} = 3$  HD 209458 b planet days (where  $\tau_p \equiv 2\pi/\Omega$  is 1 planet day). Note that I have varied the timescale of the forcing by using a  $\tau_{\text{th}}$  value in the range from 0.01 to 10 planet days, as well as letting the timescale to decrease with height. The main result does not change for values  $\gtrsim 0.1$  day, which nearly covers the entire spectrum of  $\tau_{\text{th}}$  in all past studies using the Newtonian relaxation formalism.

The spectral resolution in the horizontal direction for most of the runs described in the chapter is T42, which corresponds to  $128 \times 64$  grid points in physical space. Runs were performed with resolutions varying from T21 ( $64 \times 32$ ) to T85 ( $256 \times 128$ ), in order to check convergence of the solutions. The vertical direction is resolved by 26 coupled layers, with the top level of the model located at 3 mbar. Table 3.2 presents the  $A$  and  $B$  coefficients of Equation (2.17) in Section 2.3.1, which give the positions of all the model levels (layer interfaces). Note that, as defined, each  $\eta$ -surface can span across a range of  $p$ -surfaces. The pressure at the bottom  $\eta$  boundary is initially 1 bar, but the value of the pressure changes in time. This range of pressure is chosen because it encompasses the region where current observations are likely to be probing and where most of the circulation modelling studies have thus far directed their attention. I have also performed simulations in which the domain extends down to 100 bars and again verified that the basic behaviour described in this chapter is not affected. The entire domain is initialised with an isothermal temperature distribution,  $T_m = 1400$  K.

Table 3.2: Vertical Coordinate Coefficients

Level Surface Index	$A \times 10^3$	$B \times 10^3$
0	2.2	0
1	4.9	0
2	9.9	0
3	18.1	0
4	29.8	0
5	44.6	0
6	61.6	0
7	78.5	0
8	77.3	15.0
9	75.9	32.8
10	74.2	53.6
11	72.3	78.1
12	70.0	106.9
13	67.3	140.9
14	64.1	180.8
15	60.4	227.7
16	56.0	283.0
17	50.8	347.9
18	44.7	424.4
19	37.5	514.3
20	29.1	620.1
21	20.8	723.5
22	13.3	817.7
23	7.1	896.2
24	2.5	953.5
25	0	985.1
26	0	1000.0

Note: The pressure at each point is given by Equation (2.17), with  $p_r = 1$  bar.

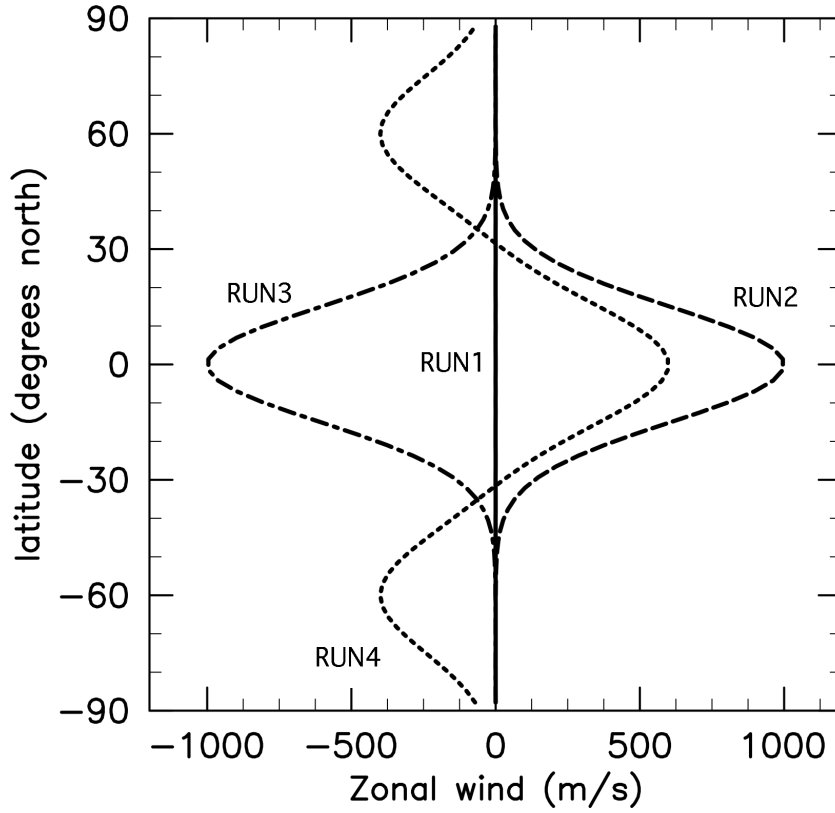


Figure 3.1: Initial conditions for simulations RUN1 (—), RUN2 (---), RUN3 (— · —), and RUN4 (···). The height-independent, zonally-symmetric, eastward velocities,  $u(\lambda, \phi, \eta, 0) = u_0(\phi)$ , are shown.

### 3.3 Results

#### 3.3.1 Basic Dependence: Jets

To examine the robustness of evolved flow states to organised initial flow configurations, I have performed simulations with a wide range of initial conditions. The conditions from four of those runs (labeled RUN1–RUN4) are shown in Figure 3.1. In all the runs presented, the setup is identical—except for the initial flow configuration. The physical and numerical parameters/conditions are given in Tables 3.1 and 3.3.

RUN1 is initialised with a small, random perturbation introduced in the flow. Specifically, values of  $u$  and  $v$  are drawn from a Gaussian random distribution centred on zero with a standard deviation of  $0.05 \text{ m s}^{-1}$ . RUN2 is initialised with a zonally-symmetric, eastward equatorial jet of

Table 3.3: Summary of Runs For Initial Condition Sensitivity

RUN	Initial Flow	$\tau_{\text{th}} [2\pi/\Omega]$	$N$	$\nu [10^{21} \text{ m}^4 \text{ s}^{-1}]$
1	small noise	3	42	1
2	eastward jet	3	42	1
3	westward jet	3	42	1
4	three jets	3	42	1
5	zero winds	3	42	1
6	small noise	0.5	21	10
7	westward jet	0.5	21	10

Notes:  $\tau_{\text{th}}$  is the thermal relaxation timescale,  $N$  is the spectral truncation wavenumber, and  $\nu$  is the superviscosity coefficient. All the runs have Robert-Asselin filter coefficient  $\epsilon = 0.06$ . In the T42 runs the timestep is  $\Delta t = 120$  s, but for T21 resolution  $\Delta t = 240$  s.

the following form:

$$u_0(\phi) = U \exp \left\{ \frac{(\phi - \phi_0)^2}{2\sigma^2} \right\}, \quad (3.3)$$

where  $u(t=0) = u_0$ ,  $U = 1000 \text{ m s}^{-1}$ ,  $\phi_0 = 0$ , and  $\sigma = \pi/12$ . RUN3 is initialised with a westward equatorial jet described by Equation (3.3), with  $U = -1000 \text{ m s}^{-1}$ ,  $\phi_0 = 0$ , and  $\sigma = \pi/12$ . RUN4 is initialised with a flow containing three jets. Note that the condition for RUN4 is very similar to the zonal average of the wind field of RUN1 at 50 planetary rotations. The jet profiles presented in Figure 3.1 are independent of height, as well as longitude.

Figure 3.2 shows the temperature and flow<sup>2</sup> fields of the four runs at  $t/\tau_p = 40$  (or  $t/\tau_{\text{th}} \approx 14$ ). The fields near the 900 mbar pressure level are shown. [Recall that the  $\eta$  level-surfaces of the model are functions of pressure, as described by Equation (2.17).] The figure illustrates the major point of this chapter: given different initial states, there are clear, qualitative (as well as quantitative) differences between the different runs. Qualitatively, there are some common features. For example, most of the runs exhibit a coherent quadrupole flow structure—two large cyclonic and

<sup>2</sup>Here, and in other figures, streamlines are shown. Streamlines are obtained by smoothly following the flow; they are tangent to the instantaneous velocity vectors at each grid point.

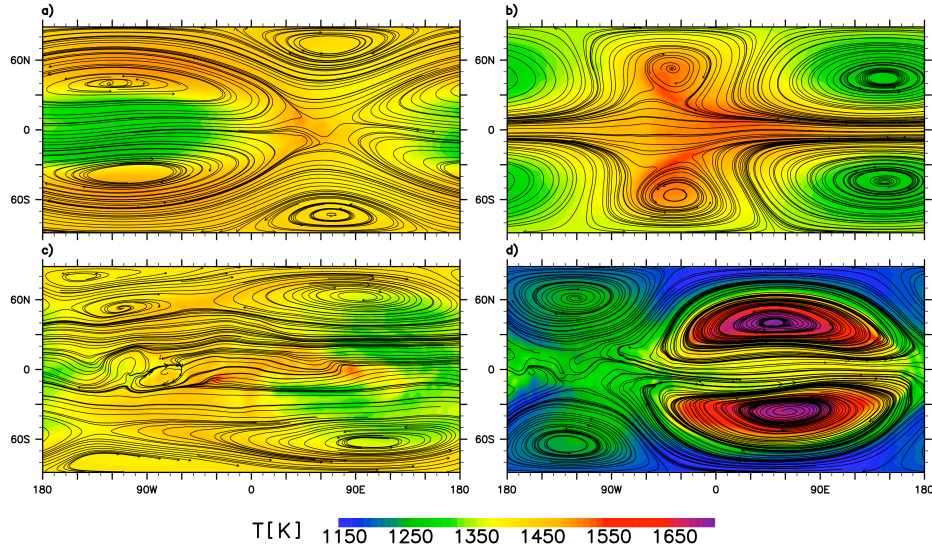


Figure 3.2: Temperature (color map) and flow (streamlines) fields at  $t = 40 \tau_p$ , near the  $p \sim 900$  mbar level, for RUN1 (a), RUN2 (b), RUN3 (c), and RUN4 (d). The fields are shown in cylindrical-equidistant projection centred at the equator. The four simulations are set up identically, except for the initial wind field. The location and size of vortices, and the associated temperature patterns, strongly depend on the initial wind configuration.

anti-cyclonic vortex-pairs straddling the equator.<sup>3</sup> However, the *location* of an individual vortex is different in the runs—as is the temperature pattern. In RUN3, a distinct quadrupole pattern is not present but there are more vortices in this run compared to the other runs. The temperature distributions are different because they are strongly linked to the flow. Consequently, the minimum-to-maximum temperature ranges vary from a moderately large 550 K (RUN4) to only about 200 K (RUN3) in the figure.

The behavior just described is not restricted to a single altitude. Figure 3.3 shows the fields corresponding to those presented in Figure 3.2, but at a higher altitude ( $p \approx 85$  mbar pressure level). Comparison of Figures 3.2 and 3.3 illustrates the structural differences in 3-D (vertical), as well as in 2-D (horizontal). In RUN2 and RUN4, the large-scale vortices are strongly aligned, forming columns through most of the height extent of the modelled atmosphere; that is, the flow is strongly barotropic. In

<sup>3</sup>The cyclonicity of a vortex is defined by the sign of  $\zeta \cdot \Omega$ : it is positive for a cyclone and negative for an anticyclone.

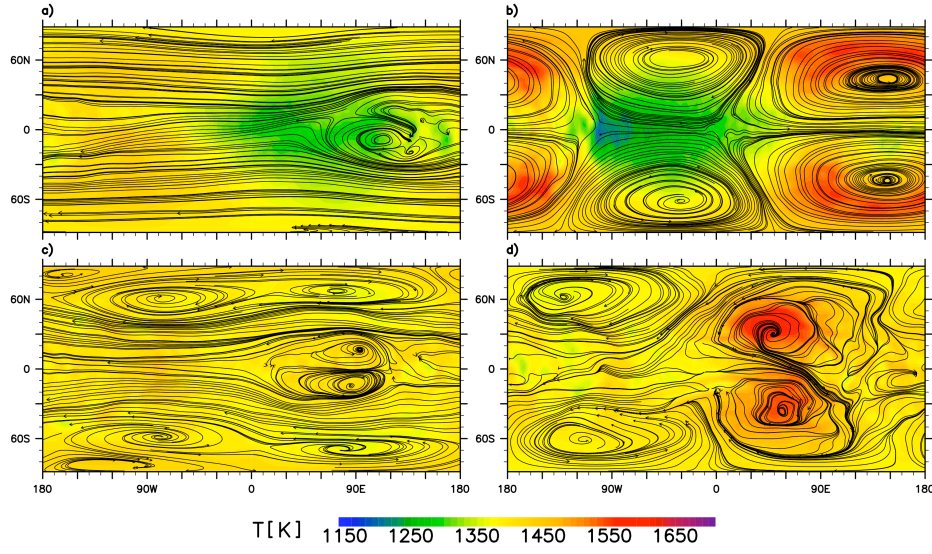


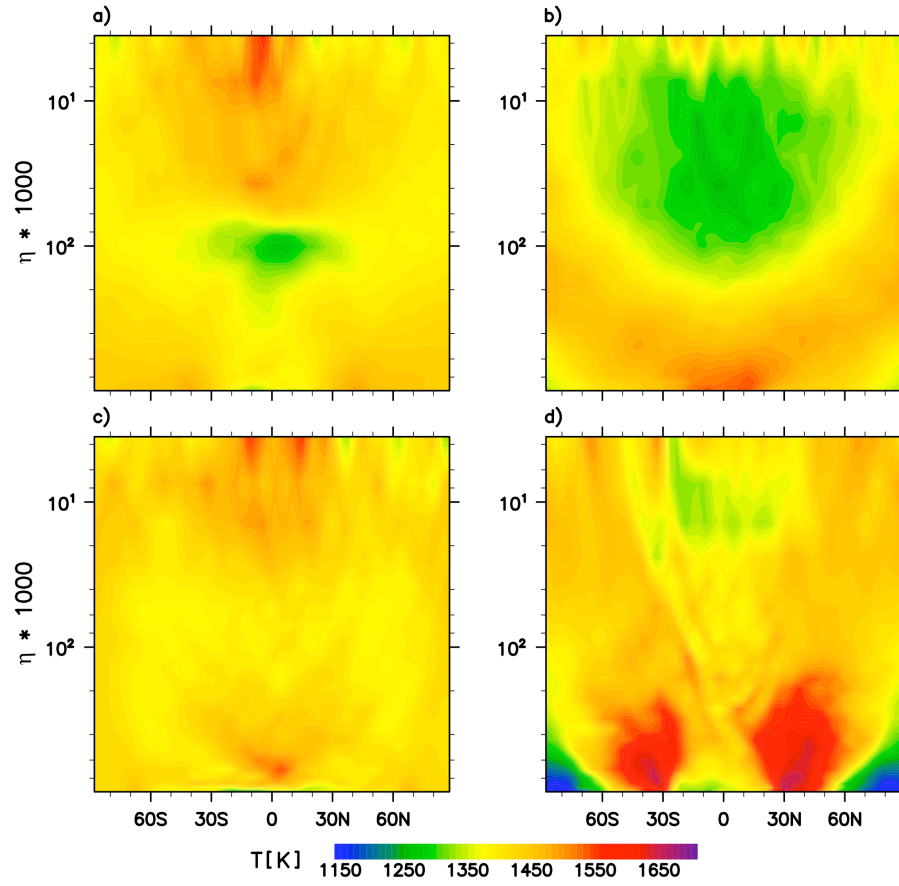
Figure 3.3: Temperature (color map) and flow (streamlines) fields at  $t = 40 \tau_p$ , near the  $p \approx 85$  mbar level, for the same four simulations as shown in Figure 3.2: RUN1 (a), RUN2 (b), RUN3 (c) and RUN4 (d). The sensitivity to the initial wind state is present throughout all heights in the atmosphere.

the other two runs, the flow is not vertically aligned throughout in large parts of the modelled atmosphere—and, therefore, the flow is baroclinic. The two figures also point to the corresponding strong difference in 3-D temperature distributions, associated with the flow structures.

This is more clearly seen in Figure 3.4. The figure shows the vertical (height-latitude) cross-section of the temperature at 0 degrees (sub-stellar) longitude from the runs presented in Figures 3.2 and 3.3. In Figure 3.4, the hottest and coldest regions are at different locations in all the runs. Near the equator, RUN1 exhibits a strong temperature inversion<sup>4</sup>, while RUN2 and RUN4 do not. In addition, RUN2 and RUN4 exhibit generally strong decreases in temperature with height, while the others do not. As can be seen, the degree of temperature mixing varies strongly in the vertical direction among the runs—from  $\sim 200$  K contrast (RUN3) to  $\sim 500$  K contrast (RUN4). In general, the vertical structure is of low order, containing usually a single inversion. In our study, some form of inversion appears to be a generic feature.

<sup>4</sup>See *Burrows et al.* [2007] and *Knutson et al.* [2008] for discussion of thermal inversion in the context of close-in extrasolar giant planets.





Preliminary steady state analysis of the primitive equations suggests that the basic behaviour described above is due to the way in which the applied,  $(s, n) = (1, 1)$ , forcing projects onto the normal modes of the planetary atmosphere; here,  $s$  is the zonal wavenumber and  $n$  is the total (sectoral) wavenumber of the spectral harmonics. In particular, a normal mode decomposition of the atmosphere into the vertical structure and Hough functions [e.g., *Chapman and Lindzen, 1970; Longuet-Higgins and Gill, 1967*] indicates that the forcing projects mostly onto low-order baroclinic modes, when the initial state is at rest. In contrast, when the initial state contains large-scale jets, the forcing projects more strongly on the barotropic mode, compared to the runs started from rest. Similar behaviour has been observed in studies of the Earth's troposphere under tropical forcing [e.g., *Geisler and Stevens, 1982; Lim and Chang, 1983*].

Furthermore, it is important to note that all of the above features, both dynamical and thermal, can vary in time. All of these features are important for observations [e.g., *Knutson et al., 2007*] and spectral modelling [e.g., *Tinetti et al., 2007*]. A thorough study of the long-time evolution (over 1000 planetary rotations, or more than  $330 \tau_{\text{th}}$ ) of the runs reveals a fundamental difference in their temporal behaviour as well. For example, the flow pattern in RUN2 is characterised by two vertically aligned vortex columns in each hemisphere that translate longitudinally around the poles. The temperature in the upper altitude region is more strongly coupled to the flow than it is in the lower altitude regions. The flow pattern in RUN4 is also a set of vertically aligned vortex columns, but the columns oscillate in the east-west direction. The patterns in RUN1 and RUN3 are more complex, exhibiting a mixture of vortex splitting and merger and stationary states at different altitude levels. Figure 3.5, which shows a time series of the total kinetic energy, gives a quantitative measure of the different temporal behaviour of the simulations.

When the flow field is time-averaged over a long period, the time-mean state is also significantly sensitive to the initial flow. This can be seen in Figure 3.6, which shows temperature cross-sections at an arbitrary longitude ( $\lambda = 135^\circ$ ), averaged over 450 planetary rotations (planet day 300 to 750). The figure clearly shows that the variability observed is not simply a result of a phase shift in a quasi-periodic evolution. The flow and

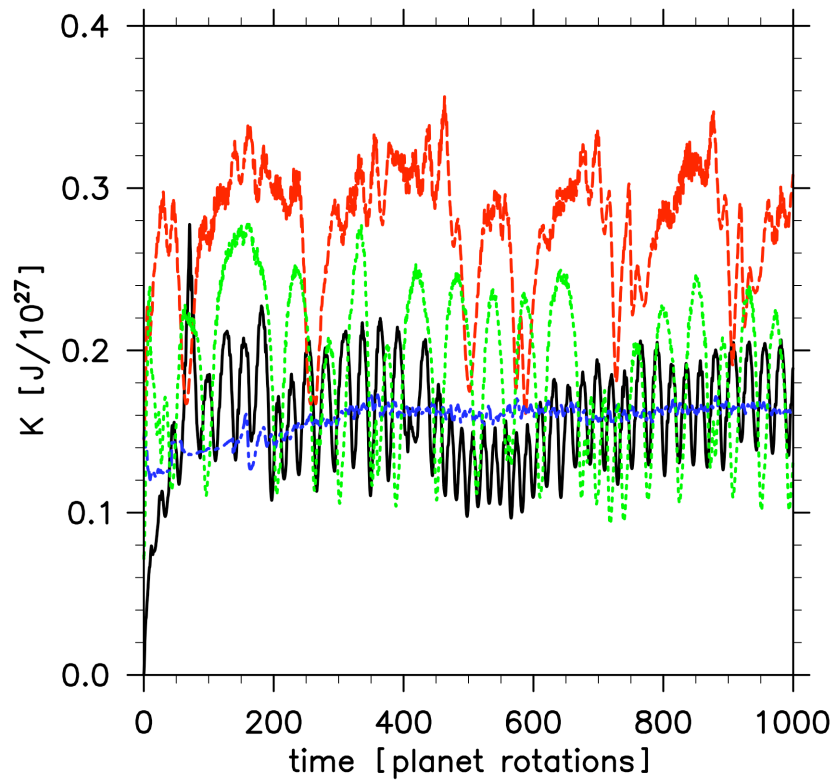


Figure 3.5: Time series of total kinetic energy, integrated over the domain, for RUN1 (black —), RUN2 (red ---), RUN3 (blue - · -), and RUN4 (green ---).

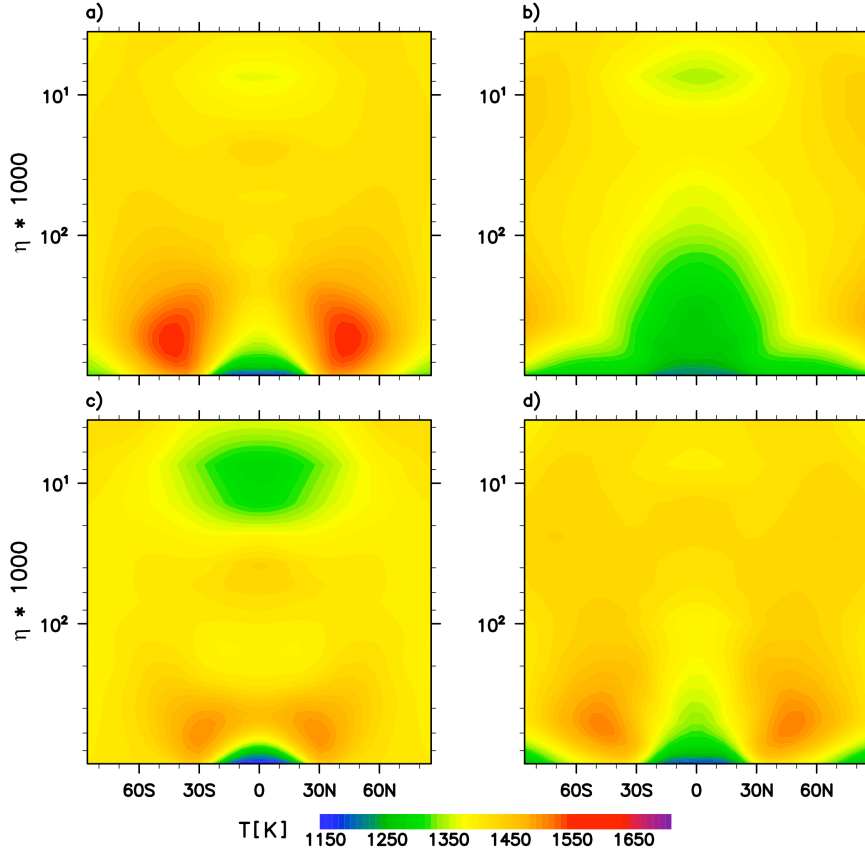


Figure 3.6: Temperature vertical cross-section at an arbitrary longitude ( $\lambda = 135^\circ$ ), averaged over 450 planetary rotations (150 thermal relaxation times), for the four simulations presented in Figure 3.2: RUN1 (a), RUN2 (b), RUN3 (c) and RUN4 (d). The difference in the temperature structure is independent of long time-averaging and is not due to a phase shift in a quasi-periodic evolution.

temperature structures in each run are fundamentally different from one another.

Interestingly, the full range of flow and temperature behaviour described above has been previously captured qualitatively, using the one-layer equivalent-barotropic model [Cho *et al.*, 2008]. The equivalent-barotropic equations are a reduced, vertically-integrated version of the full primitive equations used in this study [Salby, 1989]. In many situations, the reduced model can be fruitfully used to study the dynamics of the full model by varying the Rossby deformation radius to represent different heights (or temperatures) of the full multi-layer model [e.g., Cho *et al.*,

2008; *Scott and Polvani, 2008*], and this also appears to be the case for hot extrasolar planets.

### 3.3.2 Extreme Sensitivity: Small Stirring

As might be expected from general nonlinear dynamics theory, in fact the evolution can be strongly sensitive to small differences in the initial flow state. This is illustrated in Figure 3.7. There, two simulations are presented (panels a and b), which are identical in all respects except for a minute difference in the initial flow. The simulation in the top panel (RUN5) is started from rest. In contrast, the simulation in the bottom panel (RUN1) is started with a small perturbation: the initial values of  $u$  and  $v$  at each grid point are set to a Gaussian random distribution, centred on zero with a standard deviation of  $0.05 \text{ m s}^{-1}$ . Note that the maximum initial wind perturbation magnitude is only about 0.02% of the typical root mean square flow speed in the frames shown ( $\sim 500 \text{ m s}^{-1}$ ).

The two panels in Figure 3.7 show temperature and flow distributions after  $t/\tau_p = 1000$  (or  $t/\tau_{\text{th}} \approx 333$ ) at the  $p \sim 420 \text{ mbar}$  level. The distributions in the two panels are clearly different. At times they may look more similar than shown here, but in general that is not the case. The two runs generally show a different temporal behaviour. Note that in Figure 3.7a, there is a high degree of hemispheric symmetry, particularly in the north-south direction. In contrast, Figure 3.7b shows a clear asymmetry in both the north-south and east-west direction. The small asymmetry in Figure 3.7a is entirely due to machine precision and is not physical, since there is no way to break the symmetry in the setup of the run. Therefore, not surprisingly, some mechanism for inducing a noticeable symmetry breaking is necessary. The salient point here is, however, that even a tiny perturbation can lead to a marked difference in the flow and temperature distributions, even at relatively early integration times.

### 3.3.3 Robustness: Additional Parameter Variations

It is important to understand that the dependence on the initial flow state is robust and the behaviour is not limited only to the parameters, and the ranges, discussed thus far. The dependence has been verified for numer-

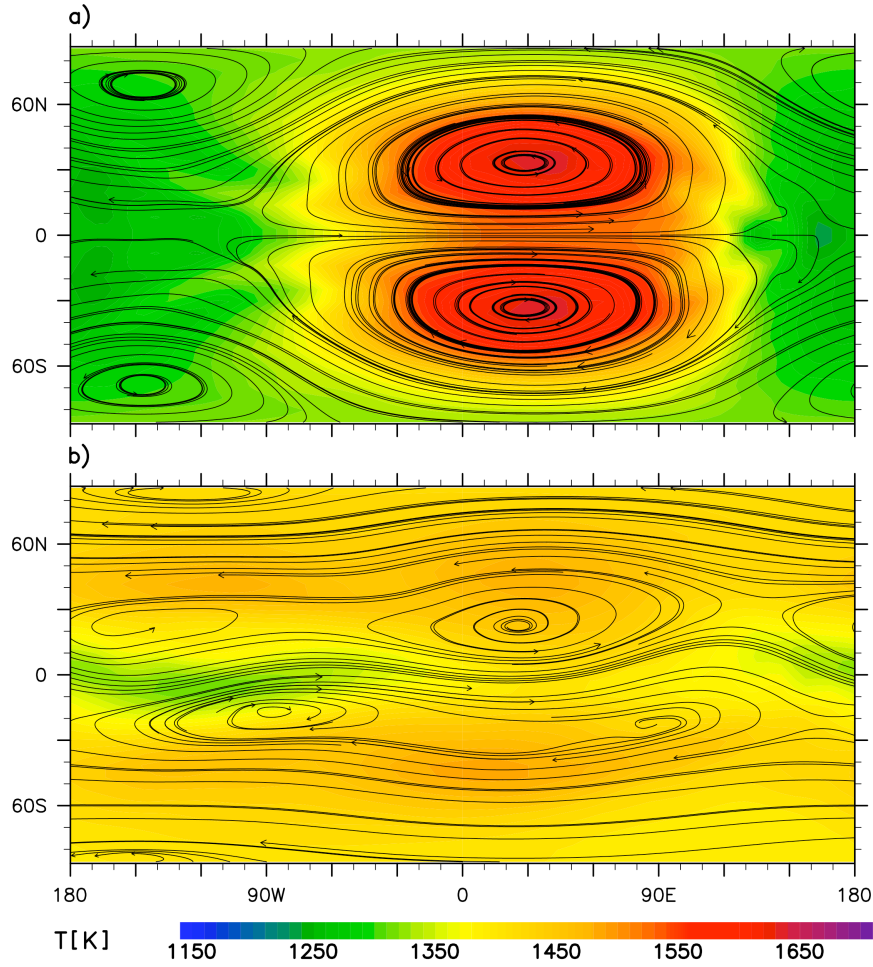


Figure 3.7: Temperature (color map) and flow (streamlines) fields after 1000 planetary rotations, at the  $p \sim 420$  mbar level, for two simulations differing only by small deviations in the initial wind. The top panel shows the result of a simulation started from rest, while the bottom panel is from a simulation started with a small perturbation. Note the clear asymmetry in the north-south direction, which only appears when the small perturbations are present in the initial state.

ous model parameters and ranges. For example, Figure 3.8 shows that the strong dependence on the initial wind exists for much shorter  $\tau_{th}$ , despite the strong forcing such relaxation times entail. In this case,  $\tau_{th}/\tau_p = 0.5$ . The upper panel is from RUN6 and the lower panel is from RUN7. The former run is initialised with only small stirring and no organised jet. In contrast, the latter run is initialised with a westward equatorial jet, identical to the setup of RUN3. At the shown time and height, there are clear differences between the flow and temperature patterns of the two simulations. The coldest area is advected east of the anti-stellar point in RUN6, but west of the anti-stellar point in RUN7. Furthermore, all the vortices have different locations. In RUN7, there is a fairly zonally symmetric jet at high latitudes, leading to a much more homogenised temperature distribution above the mid-latitudes than in RUN6.

While a weaker difference might be expected in this case, based on other studies [e.g., *Cooper and Showman, 2005*], the sensitivity is unabated in our simulations. And, this holds for the long time average behaviour as well. Figure 3.9 shows a time mean of the temperature fields, taken over 300 rotations (planet days 1200 to 1500), at the same level as shown in Figure 3.8. The location of the coldest region differs by 40 degrees in longitude between the two simulations shown in the figure. Figure 3.10 shows a time series of the total kinetic energy in the two simulations, revealing their different evolution. Even after integrating for a very long time (over 80,000 rotations), I have checked that the differences between RUN6 and RUN7 are still present. Note that this is a much longer integration time than that reported in any published studies of close-in planet circulation thus far. However, the flow at such long times is inexorably affected by cumulative numerical dissipation and phase errors and the result obtained should not be taken too literally [e.g., *Canuto et al., 1988*].

In addition, I have studied the dependence when the initial jet contains a vertical shear—i.e., the jet distribution is baroclinic. Simulations have been initialised with an eastward jet, which has zero magnitude at the bottom and increases linearly with height so that the lateral flow distribution in the top layer of the model is identical to that in RUN2.<sup>5</sup> In

<sup>5</sup>Recall that the flow distribution in this run is barotropic.

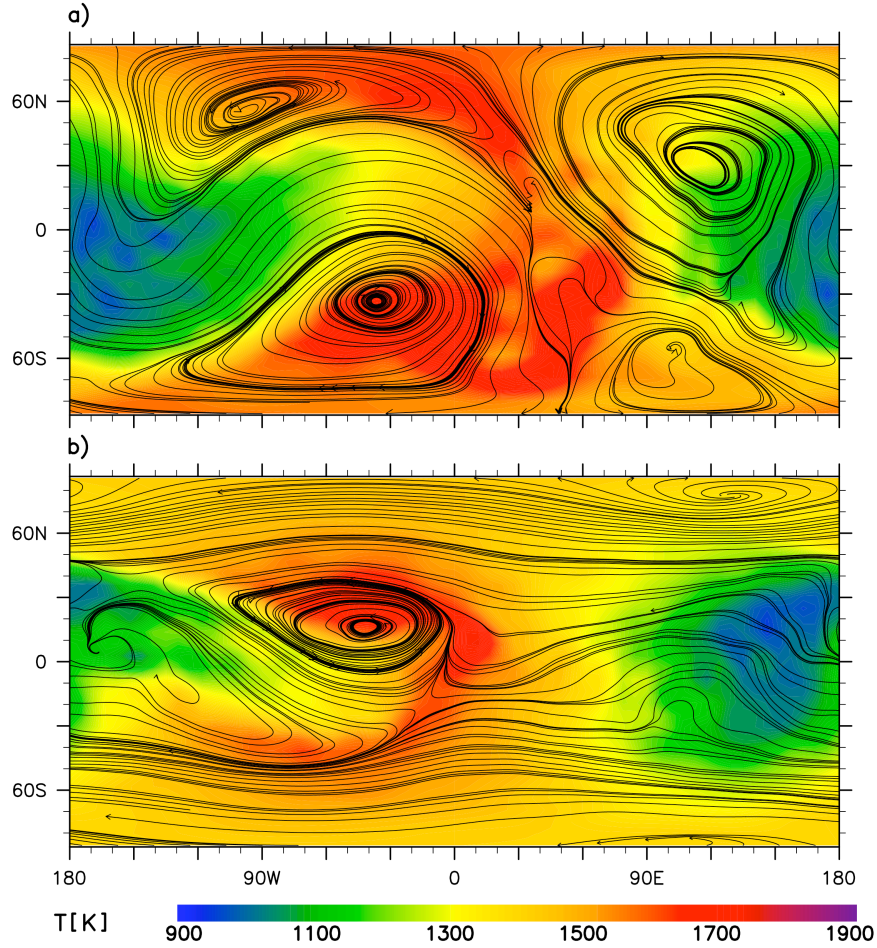


Figure 3.8: Snapshots of temperature fields (colour coded) with streamlines overlaid. Fields at the  $p \sim 900$  mbar level are shown at  $t = 1000$  planetary rotations, for two simulations (RUN6 and RUN7); the thermal relaxation time is 0.5 planetary rotations (42 hours) in these runs. The only difference between the simulations is the initial wind state. The top panel shows the result of a simulation started with only a small perturbation and the bottom panel is from a simulation started with a westward jet. The sensitivity to the initial flow state is still present for this small value of the thermal relaxation time (cf., RUNS 1–4).



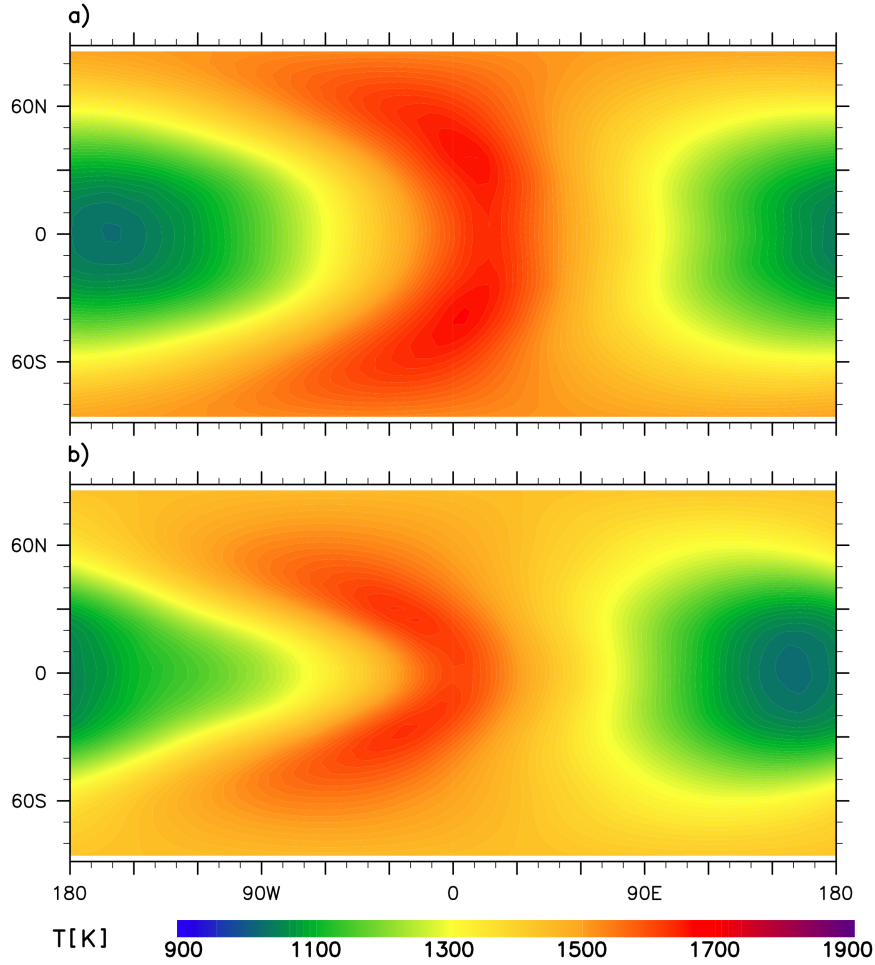


Figure 3.9: Time averaged temperature fields from two simulations that differ only in the initial wind state. The two simulations (RUN6, top panel, and RUN7, bottom panel) and the vertical level ( $p \sim 900$  mbar) are the same as in Figure 3.8. The average is taken over 300 rotations (planet days 1200 to 1500). The location of the coldest spot differs by 40 degrees in longitude between the two simulations.

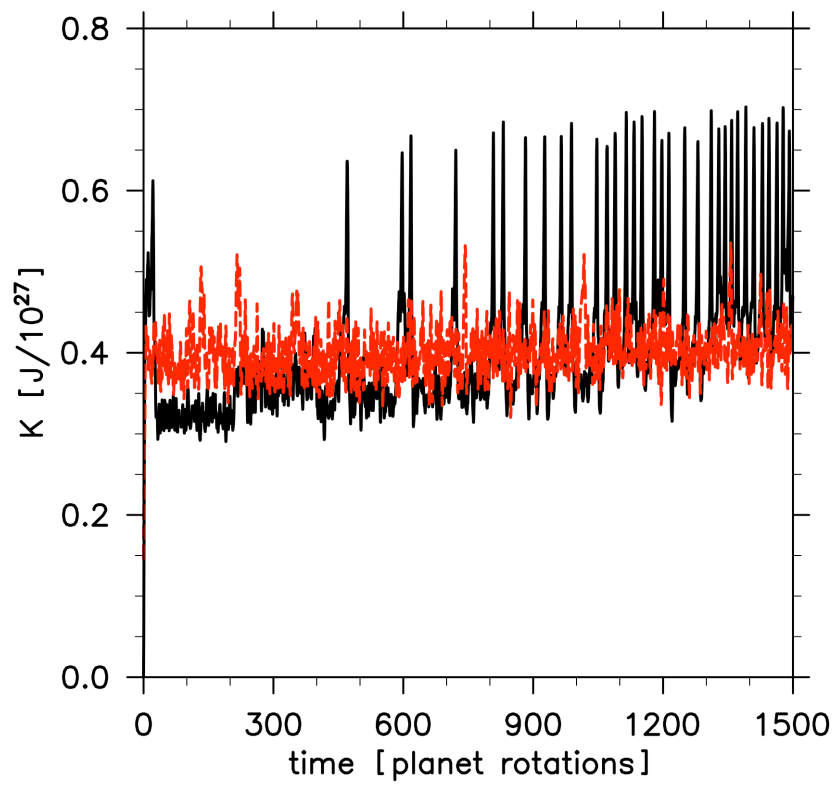


Figure 3.10: Time series of total kinetic energy, integrated over the domain, for RUN6 (black —) and RUN7 (red ---).

the baroclinic case, vortex columns evolve that extend throughout most of the atmosphere, as in RUN2. However, unlike in RUN2, the temperature structure here is also strongly barotropic. This appears to be related to the way the forcing projects onto the free modes of the system, as described in section 3.3.1.

As alluded to in section 2.1, the timescale of the fastest motions admitted by Equations (2.3-2.9) (and equivalently Equations (2.34-2.41)) with the given boundary condition is  $\sim 40$  minutes, for the planetary physical parameters used in this work. Hence, a forcing with timescales of the same order or smaller is not entirely physically self-consistent with the use of Equations (2.3-2.9). Notably, such forcing introduces numerical difficulties, as discussed in Chapter 4. For the physically unrealistic relaxation time of  $\tau_{\text{th}} = 1$  hour, for which excessive numerical dissipation is required to prevent the code from blowing up or being inundated with numerical noise, the *temperature* evolution is only mildly sensitive to the initial condition, at long-time integrations. However, when such short relaxation times are only applied over a limited range in pressure—i.e.,  $\tau_{\text{th}}$  is allowed to vary with  $\eta$ —the sensitivity to the initial condition is present even after long time integrations (7000 planet days).

## 3.4 Conclusion

In this chapter, it has been shown that in a generic general circulation simulation of a tidally synchronised planet, the flow and temperature distributions depend strongly on the initial state. In all simulations initialised with a different jet configuration, large scale coherent vortices are formed; but, their location, size, and number varies, depending on the initial wind. The temperature distribution is relatively homogenised by the flow, compared to the large temperature contrast in the forcing equilibrium temperature profile. But the degree of mixing, as well as locations of temperature extremes vary between differently initialised simulations. The time variability of the atmosphere – i.e. how vortices and associated temperature patterns move around the planet or whether they stay at fixed positions – varies depending on the initial wind.

The Newtonian relaxation scheme used in this study is idealised and

the “correct” parameters to use in the setup are unknown, with many choices possible. Explorations of different parts of the parameter space are presented in the following chapters. Here, the setup has been chosen to capture, as cleanly as possible, the effects of the initial flow in a regime of parameter space plausibly relevant for hot Jupiters with strong zonally-asymmetric forcing. It has been found that the strong dependence on the initial wind is valid for a wide range of thermal relaxation times ( $\tau_{\text{th}} = 0.5$ –10 planet days) and with T21, T42, and T85 resolutions. Some reduction in the sensitivity is sometimes observed for the very small  $\tau_{\text{th}}$  and long time integration simulations, which require large numerical dissipation to prevent the fields from being dominated by small scale noise. This situation is, however, not physically realistic and numerically suspect.

The strong dependence on initial wind has implications for the use of general circulation models for interpretation of observations of extrasolar planet atmospheres. These results underline that, while numerical circulation models of the kind employed here are useful for studying plausible mechanisms and flow regimes, they are currently unsuitable for making “hard” predictions—such as exact locations of temperature extremes on a given planet.

## Chapter 4

# Dissipation and Relaxation Time Interaction

In this chapter, I elucidate the interplay between Newtonian thermal relaxation and numerical dissipation, of several different origins, in flow simulations of hot extrasolar planet atmospheres. Currently, a large range of Newtonian relaxation, or “cooling”, times ( $\sim 10$  days to  $\sim 1$  hour) is used among different models and within a single model over the model domain. In this study, I demonstrate that a short relaxation time (much less than the planetary rotation time) leads to a large amount of unphysical, grid-scale oscillations that contaminate the flow field. These oscillations force the use of an excessive amount of artificial viscosity to quench them and prevent the simulation from “blowing up”. Even if the blow-up is prevented, such simulations can be highly inaccurate because they are either severely over-dissipated or under-dissipated, and are best discarded in these cases. Other numerical stability and timestep size enhancers (e.g., Robert-Asselin filter or semi-implicit time-marching schemes) also produce similar, but less excessive, damping. Diagnostics procedures to choose the “optimal” simulation are presented and the implications of these findings for modelling hot extrasolar planet atmospheres are discussed.

## 4.1 Introduction

There are many studies using a “general circulation model” (GCM) to investigate the flow and temperature structure of close-in extrasolar planet atmospheres [e.g., *Showman and Guillot*, 2002; *Cho et al.*, 2003; *Cooper and Showman*, 2005; *Langton and Laughlin*, 2007; *Cho et al.*, 2008; *Dobbs-Dixon and Lin*, 2008; *Showman et al.*, 2008a; *Menou and Rauscher*, 2009; *Thrastarson and Cho*, 2010; *Rauscher and Menou*, 2010]. In these sophisticated models, numerous parameters are needed to specify the representation of heating and cooling in the atmosphere and to stabilise the numerical integration.

Thus far, not much emphasis has been given to the numerical aspects of simulations in the extrasolar planet literature, in particular their influence on the accuracy of the model results. In Chapter 3 and *Thrastarson and Cho* [2010] the sensitivity of initial condition on the extrasolar planet atmosphere flows was investigated. In the present chapter, the focus is on another significant aspect—the subtle, and not so subtle, interplay between numerical and physical parameters. It should be noted that, while the discussion is basically numerical, this work is relevant to both theoretical studies and observations of extrasolar planets.

GCMs usually solve the hydrostatic primitive equations [see, e.g., *Salby*, 1996], which filter sound waves so that only two important classes of waves remain—Rossby, or planetary, waves (which evolve on slow time scales) and gravity waves (which generally evolve on time scales much shorter than the Rossby waves). The spatial scales of the two classes of motions are generally large and small, respectively. Nonlinear advection, which has often been used to define a time scale in extrasolar planet work so far, has roughly the same time scale as the Rossby waves. Generally, the amplitude of gravity waves, when averaged over the globe, is very small compared to that of Rossby waves, and most of the kinetic energy is contained in the large-scale, slow motions.

A long-standing challenge in GCM theory is finding ways to deal with fast waves accurately and efficiently. The fast motions not only force small timesteps to be taken (increasing the “wall time” of the simulations), they also degrade the fidelity with which the equations are solved. Moreover,

the very inaccuracy often causes the calculation to “blow up” (become unstable), preventing any solution at all. With certain types of numerical algorithms, such as implicit or semi-implicit time-integration schemes, the timestep size restriction can be alleviated. But, artificial viscosity and various filters are still required to stabilise the integration in general.

It is well known that, in conjunction with coarse resolution, dissipation and filters can produce results that are seductively misleading—even to the wary modellers. For example, in the classic Held-Suarez test for the dynamical core of GCMs for the Earth [*Held and Suarez, 1994*], increasing the resolution generally leads to enhanced equator-ward shift of wave activity [*Wan et al., 2008*]. The shift becomes more evident in the simulations with horizontal resolutions  $\gtrsim$  T85 resolution (i.e., 85 sectoral and 85 total modes) so that precise jet positions, for example, cannot be ascertained at lower resolutions. This is a relatively mild example, but it is telling: the more extreme forcing condition for extrasolar planets, it can be argued, will lead to larger or more sensitive variations, given that the models have been designed and tested for conditions appropriate for Solar System planets. In this backdrop, even inter-comparing different GCMs for extrasolar planet work becomes non-trivial.

In this chapter we present and discuss examples of interesting behaviour when a GCM is stressed to its limits, with what may be considered a typical hot, spin-orbit synchronised extrasolar planet condition. The implications are broad in the sense that the lessons are not just limited to studies using GCMs, but also other types of global circulation models. The issues are present in all of them.

The basic plan of the chapter is as follows. In Section 4.2 the numerical methods used in the model are discussed, and the setup for the simulations presented in this work is described. In Section 4.3.1 we focus on the interdependence between artificial viscosity and the thermal relaxation time, which is an important parameter in the representation of thermal forcing commonly used in current studies. In Section 4.3.2 we examine sensitivity of the simulations to the Robert-Asselin filter, which is used to stabilise the time-marching scheme. We conclude in Section 4.4, summarising this work and discussing its implications for extrasolar planet circulation modelling.

## 4.2 Method

### 4.2.1 Numerical Algorithm

In this chapter, the same equations are solved as in the previous chapter, the primitive equations in the form (2.34-2.41). To solve the equations, the Community Atmosphere Model (CAM 3.0), described in Section 2.3, is used. CAM is a well-tested, highly-accurate hydrodynamics model employing the pseudospectral algorithm [Orszag, 1970; Eliassen *et al.*, 1988].

For problems not involving sharp discontinuities (e.g., shocks or, in atmospheric dynamics problems, fronts) and irregular geometry, the pseudospectral method is superior to the standard grid and particle methods [e.g., Canuto *et al.*, 1988]. To equal the accuracy of the pseudospectral method for a problem solved with the computational domain decomposed into  $N$  grid points, one would need a  $N^{\text{th}}$ -order finite difference or finite element method with an error of  $O(N\Delta x)$ , where  $\Delta x$  is the grid spacing and  $O(\cdot)$  is the asymptotic order [e.g., Nayfeh, 1973]. This is because as  $N$  increases, the pseudospectral method benefits in two ways. First,  $\Delta x$  becomes smaller, which would cause the error to rapidly decrease even if the order of the method were fixed. However, unlike finite difference and finite element methods, the order is *not* fixed: when  $N$  is doubled to  $2N$ , the error becomes  $O[(\Delta x)^{2N}]$  in terms of the new, smaller  $\Delta x$ . Since  $\Delta x$  is  $O(1/N)$ , the error for the pseudospectral method is  $O[(1/N)^N]$ .

Significantly, the error decreases faster than any finite power of  $N$  since the power in the error formula is always increasing as well, giving an “infinite order” or “exponential” convergence. This advantage is particularly important when many decimal places of accuracy or high resolution is needed. When steep jumps are present, the pseudospectral method loses its advantage, but in this case both finite difference and spectral methods require high resolution or additional measures to properly capture the flow. Note that in the vertical direction CAM uses a finite differencing scheme, as in most GCMs.

For the spherical geometry, the horizontal representation of an arbitrary scalar quantity  $\xi$  consists of a truncated series of spherical harmon-



ics,

$$\xi(\lambda, \mu) = \sum_{m=0}^M \sum_{n=|m|}^{N(m)} \xi_n^m P_n^m(\mu) e^{im\lambda}, \quad (4.1)$$

where  $M$  is the highest Fourier (sectoral) wavenumber included in the east-west representation;  $N(m)$ , which can be a function of the Fourier wavenumber  $m$ , is the highest degree of the associated Legendre functions  $P_n^m$ ;  $\lambda$  is the longitude; and,  $\mu \equiv \sin \phi$ . The spherical harmonic functions,

$$Y_n^m(\lambda, \mu) = P_n^m(\mu) e^{im\lambda}, \quad (4.2)$$

used in the spectral expansion are the eigenfunctions of the Laplacian operator in spherical coordinates:

$$\nabla^2 Y_n^m = - \left[ \frac{n(n+1)}{R_p^2} \right] Y_n^m, \quad (4.3)$$

where

$$\nabla^2 = \frac{1}{R_p^2} \left\{ \frac{\partial}{\partial \mu} \left[ (1 - \mu^2) \frac{\partial}{\partial \mu} \right] + \frac{1}{1 - \mu^2} \frac{\partial^2}{\partial \lambda^2} \right\}$$

and  $R_p$  is the planetary radius. The set,  $\{Y_n^m\}$ , constitutes a complete and orthogonal expansion basis [Byron and Fuller, 1992].

In the Navier-Stokes equations, the diffusion terms appear as the Laplacian of the dynamical variables [Batchelor, 1967]. In our case, the diffusion is generalised to the following “hyperdiffusion” form [e.g., Cho and Polvani, 1996]:

$$\mathcal{D}_\chi = \nu_{2p} \left[ (-1)^{p+1} \nabla^{2p} + \mathcal{C} \right] \chi, \quad (4.4)$$

where  $\chi = \{\zeta, \delta, T\}$  and  $\mathcal{C} = (2/R_p^2)^p$  is a correction term added to the vorticity and divergence equations to prevent damping of uniform rotations for angular momentum conservation. In the above form, the  $p = 2$  case is sometimes referred to as *superdissipation*. When  $p = 1$ , the above general expression reduces to the ordinary molecular, or Newtonian, viscosity. Hyperdiffusion is added in each layer to prevent accumulation of power on the small, poorly-resolved scales and to stabilise the integration.

Cho and Polvani [1996] describes the effects of various hyperviscosity-

ties (i.e., different values of  $p$ ). As outlined in that work, a rational procedure for estimating roughly the value of  $\nu_{2p}$  can be obtained in the following way. To damp oscillations at the smallest resolved scale (set by the truncation wave number,  $n_t$ ), by an  $e$ -folding factor in time  $\tau_d$ , one requires that

$$\nu_{2p} = O \left\{ \frac{1}{\tau_d} \left[ \frac{R_p^2}{n_t(n_t + 1)} \right]^p \right\}. \quad (4.5)$$

Thereafter, the optimal value of  $\nu_{2p}$  is obtained by computing the kinetic energy spectrum (see Section 4.3). Note that the precise value is problem specific, and the procedure just described should be performed for *each* problem, adjusting  $\nu_{2p}$  between different simulations—as has been done in this work.

In numerical solutions of time-dependent equations, there are two main ways of marching in time. Explicit methods give the solution at the next time level in terms of an explicit expression which can be evaluated by using the solution at the previous timestep. Implicit methods, on the other hand, require solving a boundary value problem at each timestep. Explicit time differencing is a more straightforward numerical approximation to the equations. In our model, the time-marching is effected using a *semi*-implicit scheme, a mixture of the two methods commonly used in GCMs. In this scheme, the equations are split into nonlinear and linear terms, symbolically written:

$$\frac{\partial \Psi}{\partial t} = \mathcal{N}(\Psi) + \mathcal{L}(\Psi), \quad (4.6)$$

where  $\mathcal{N}(\Psi)$  and  $\mathcal{L}(\Psi)$  denote the nonlinear and linear terms, respectively, and  $\Psi$  is the state of a variable in  $\chi = \{\zeta, \delta, T\}$ .

For the nonlinear terms, an explicit leapfrog scheme is used. This is a second-order, three-time-level scheme. Because a second-order method is applied to solve a differential equation which is first-order in time, an unphysical computational mode is admitted, in addition to the physical one. In simulations containing nonlinear waves, the computational mode can amplify over time, generating a time splitting instability [Durrant, 1999]. Robert (1966) and Asselin (1972) designed a filter to suppress the computational mode—hence the time splitting instability. This filter is applied in

the GCM used in the present work. It is applied at each timestep so that

$$\bar{\Psi}^n = \Psi^n + \epsilon (\bar{\Psi}^{n-1} - 2\Psi^n + \Psi^{n+1}), \quad (4.7)$$

where  $\Psi^n = \Psi(n\Delta t)$ , an overbar refers to the filtered state, and  $\epsilon$  specifies the strength of the filter. The filter results in strong damping of the amplitude of the spurious computational mode. However, it also introduces a second-order error in the amplitude of the physical mode with high values of  $\epsilon$ , as we discuss further in Section 4.3.2.

Some parts of the equations can be solved implicitly with advantage. In particular, the linear parts that produce fast gravity waves are treated implicitly in many GCMs, including the one used in this work. This treatment allows a larger timestep to be used, as mentioned in Section 4.1. However, it is also at the cost of degraded accuracy [e.g., *Durran*, 1999].

As can be seen, time-integration of the primitive equations is not a straightforward matter, even with a relatively simple method like the leapfrog scheme. The theoretical analysis of the scheme is equally complex. The stability of the combined, semi-implicit leapfrog scheme has been examined by *Simmons et al.* [1978], particularly with respect to the basic state temperature profile. They find the isothermal basic state distribution to be more stable than a spatially-varying distribution, with the stability generally increasing with higher basic temperature. In the present work an isothermal basic state of 1400 K is used.

### 4.2.2 Calculation Setup

In addition to tuneable parameters associated with the numerical scheme, such as the ones mentioned in the preceding subsection, the representations of physical processes also require specification of parameters. Many of these are as yet poorly constrained by observations or unobtainable from first principles (see, e.g., discussions in *Cho et al.* [2008], *Showman et al.* [2008b], and *Cho* [2008]). One example is thermal forcing (i.e., heating and cooling) due to the irradiation from the host star and radiative processes in the planetary atmosphere, which is represented in an idealised way currently in all extrasolar planet atmosphere simulations. Many crudely represent the forcing by Newtonian relaxation, as in this work [e.g., *Cooper and Showman*, 2005; *Langton and Laughlin*, 2007;

*Showman et al.*, 2008a; *Menou and Rauscher*, 2009; *Rauscher and Menou*, 2010; *Thrastarson and Cho*, 2010].

In this representation, the net heating term in equation (2.32) is represented by

$$\frac{\dot{q}_{\text{net}}}{c_p} = -\frac{1}{\tau_{\text{th}}} (T - T_e), \quad (4.8)$$

where  $T_e = T_e(\lambda, \phi, \eta, t)$  is the “equilibrium” temperature distribution and  $\tau_{\text{th}}$  is the thermal relaxation (drag or “cooling”) time. The appropriate values to use for this relaxation time (as well as the equilibrium temperature distribution) are poorly known and a large range of values has been used in the extrasolar planet literature. In several studies, very short relaxation times—even less than an hour—and large  $T_e$  gradients have been used [e.g., *Showman et al.*, 2008a; *Rauscher and Menou*, 2010; *Thrastarson and Cho*, 2010]. This represents a rather “violent” forcing on the flow, depending on the initial condition.

In this work, both  $\tau_{\text{th}}$  and  $T_e$  are prescribed and barotropic (i.e.,  $\partial/\partial\eta = 0$ ) and steady (i.e.,  $\partial/\partial t = 0$ ). As in Chapter 3 and *Thrastarson and Cho* [2010],

$$T_e = T_m + \Delta T_e \cos \phi \cos \lambda, \quad (4.9)$$

with  $T_m = (T_D + T_N)/2$  and  $\Delta T_e = (T_D - T_N)/2$ , where  $T_D$  and  $T_N$  are the maximum and minimum temperatures at the day and night sides, respectively. All the simulations described in this chapter have  $T_D = 1900$  K and  $T_N = 900$  K. Other physical parameters chosen are based on the close-in extrasolar planet, HD209458b. These are the same parameters as those used in Chapter 3, and they are listed in Table 3.1.

The spectral resolutions in the horizontal direction for the runs described in the paper are T85 and T21. The number refers to the maximum total wavenumber,  $n_t = \max\{N(m)\}$ , at which expansion (4.1) is truncated (e.g., T85  $\Rightarrow n_t = 85$ ); “T” means the truncation is such that  $M = N$  in equation (4.1), a “triangular truncation” in wavenumber space. The vertical direction is resolved by 26 coupled layers, with the top level of the model located at 3 mbar. The pressure at the bottom  $\eta$  boundary is initially 1 bar, but the value of the pressure changes in time. The entire domain is initialised with an isothermal temperature distribution,

Table 4.1: List of Runs Discussed

Run	$\nu_{2p}$ [ $\text{m}^4 \text{s}^{-1}$ ]	$p$	$\tau_{\text{th}}/\tau_p$
N1a	$1 \times 10^{24}$	2	.1
N1b	$1 \times 10^{24}$	2	3
N2a	$1 \times 10^{23}$	2	.1
N2b	$1 \times 10^{23}$	2	3
N3a	$1 \times 10^{22}$	2	.1
N3b	$1 \times 10^{22}$	2	3
N4a	$1 \times 10^{21}$	2	.1
N4b	$1 \times 10^{21}$	2	3
N5a	$1 \times 10^{20}$	2	.1
N5b	$1 \times 10^{20}$	2	3
N6a	${}^\dagger 6 \times 10^{12}$	1	.1

Notes:  $\nu$  is the hyperviscosity coefficient and  $p$  the order index of the hyperviscosity.  $\tau_{\text{th}}$  is the thermal relaxation timescale and  $\tau_p$  is one planet rotation. All the simulations are run at T85 resolution with a timestep  $\Delta t$  of 60 s and a Robert-Asselin filter coefficient  $\epsilon$  of 0.06.

${}^\dagger$ The units for this  $\nu$  are [ $\text{m}^2 \text{s}^{-1}$ ].

$T_0 = T_m = 1400$  K. The flow field is initialised with a small, random perturbation; specifically, values of the  $\mathbf{v}$  components are drawn from a Gaussian random distribution centred on zero with a standard deviation of  $0.05 \text{ m s}^{-1}$ . The sensitivity to initial flow is described in detail in Chapter 3 and *Thrastarson and Cho* [2010].

## 4.3 Results

### 4.3.1 Spatial Dissipation

Table 4.1 lists all the runs discussed in this subsection. Simulations are performed with the setup described above, but with varying strength of artificial viscosity ( $\nu$  and  $p$ ) and the forcing timescale ( $\tau_{\text{th}}$ ). Figure 4.1 presents the relative vorticity field near the  $p \approx 85$  mb level; this is approximately a quarter of the way down from the top of the computational domain. The field at  $t = 80 \tau_p$  is shown in cylindrical equidistant projection, centered at the equator, for ten simulations in which the setup is identical except for the values of  $\tau_{\text{th}}$  and  $\nu$  ( $p = 2$ , superdissipation);

here,  $\tau_p = 2\pi/\Omega$  is the planetary rotation period. Positive vorticity (red colour) signifies local rotation in the same direction as the planetary rotation (counter-clockwise in the northern hemisphere), and opposite for the negative vorticity. The panels on the left column all have the same short value of  $\tau_{th} = 0.1 \tau_p$ , while the panels on the right column all have  $\tau_{th} = 3 \tau_p$  for five different values of  $\nu$ . In all the runs shown, the global kinetic energy time series have reached a quasi-stationary (“equilibrated”) state and do not change qualitatively for approximately  $300 \tau_p$ .

For a given value of  $\tau_{th}$ , simulations with different  $\nu$ ’s generally share some common features over a range of  $\nu$ ’s. But, there are clear differences in the character of the flow and temperature fields. The differences, which are both qualitative and quantitative, arise from the strength of dissipation. Moreover,  $\nu$  can affect the temporal behaviour as well. For example, temporal variability can be muted with larger  $\nu$ . Not surprisingly, in the strongest dissipation cases [panels (a) and (b)] variability in time is essentially completely quenched and the flow structures are quite smooth in appearance. These are examples of runs which are severely over-dissipated.

At the other extreme, runs can also be severely under-dissipated. This is shown in panels (i) and (j) in Figure 4.1. Note that the common  $\nu$  value in these runs is four orders of magnitude smaller than that for the runs of panels (a) and (b). A quick visual check of panels (i) and (j) immediately shows the physical fields dominated by small-scale oscillations: this is numerical noise. Here, by “small” we mean scales near the grid-scale,  $l = O(\Delta x)$ . Typically, runs like these blow up—or at least they should (see Section 4.3.2). Simulations often blow up long before the small-scales contain any significant amount of energy compared to the large-scales. As we discuss more later, this is because the calculation *correctly* becomes unstable. But, sometimes misbehaving simulations can be surprisingly resilient and not crash. This is usually a signal that bad numerics is at play.

As expected, increasing  $\nu$  leads to decreasing small-scale oscillations and to increasingly smoother fields. However, significantly, we note that for a given value of  $\nu$  for the two  $\tau_{th}$ ’s (cf., panels of the same row in Figure 4.1) shorter  $\tau_{th}$  in a run admits much more pronounced grid-scale oscillations. For example, with  $\nu_4 = 10^{22} \text{ m}^4 \text{ s}^{-1}$  [panels (e) and (f)], the

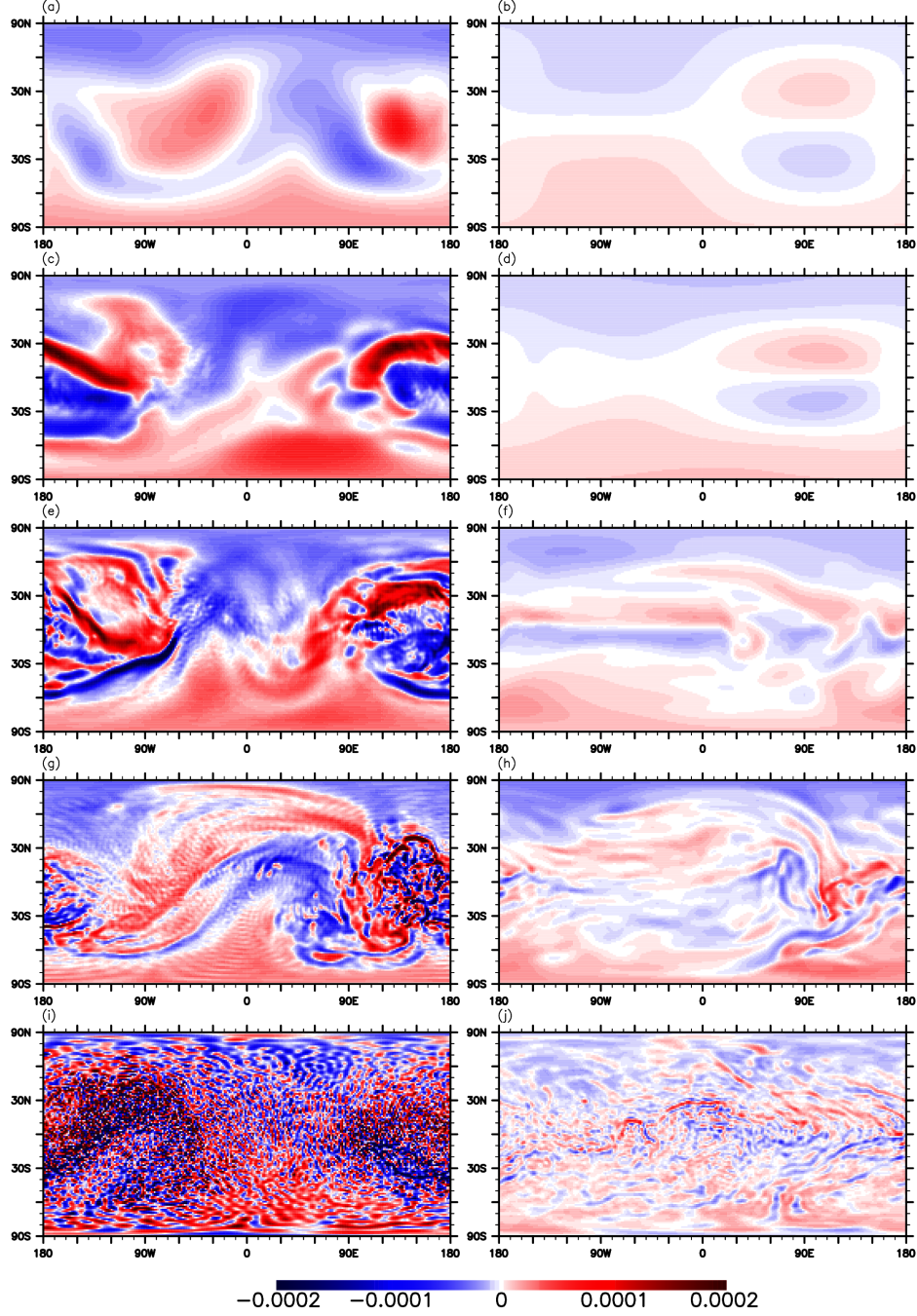


Figure 4.1: Vorticity field at  $t = 80 \tau_p$  (planet rotations), near the  $p \approx 85$  mb level, for two sets of five simulations (left column and right column) that are set up identically, except for the viscosity coefficient and the thermal relaxation time. The superdiffusion coefficient is  $\nu_4 = \{10^{24}, 10^{23}, 10^{22}, 10^{21}, 10^{20}\} \text{ m}^4 \text{ s}^{-1}$ , decreasing from top to bottom in each column. The panels in the left column have a relaxation time of  $\tau_{\text{th}} = 0.1 \tau_p$  while the panels on the right have  $\tau_{\text{th}} = 3 \tau_p$ . Red (blue) colour represents positive (negative) values of vorticity, with units  $\text{s}^{-1}$ .

viscosity is clearly *insufficient* to suppress small-scale oscillations in the case of  $\tau_{\text{th}} = 0.1 \tau_p$ , while no small-scale oscillations are present in the calculation with longer  $\tau_{\text{th}}$ . More importantly, a  $\nu$  value which appears to be acceptable for the shorter relaxation time [e.g., panel (a)] is clearly over-dissipative for the run with the longer  $\tau_{\text{th}}$  [e.g., panel (b)]: here, the calculation in (b) should be compared with that in (f), which is clearly a much less dissipated run than that in (b). Hence, running a simulation at a single  $\tau_{\text{th}}$ —even if  $\nu$  were varied—would not produce trustworthy results since the parameter space is at least two-dimensional.

The implication of this is serious. In many current simulations of hot planet atmospheric flows, a range of  $\tau_{\text{th}}$ 's is specified, spread over the model atmosphere domain, which always contains a region with a short  $\tau_{\text{th}}$ . Note that the values of  $\tau_{\text{th}}$  used in several studies for some regions of their model atmospheres are even smaller than that employed here—e.g.,  $0.01 \tau_p$  in *Cooper and Showman* [2005] and *Rauscher and Menou* [2010] and  $0.001 \tau_p$  in *Showman et al.* [2008a]. This forces those model atmosphere calculations to be excessively noisy *and* excessively dissipated, in different atmospheric regions of the computational domain. Once noise appears in the calculation somewhere in the domain, the entire domain becomes quickly contaminated (via, e.g., nonlinear interactions). Note that an inherently smooth field—such as temperature, compared to vorticity, for example—would not reveal the noise as well, since it is essentially two integrations (smoothing operations) of the vorticity field. In other words, temperature possesses a steep (narrow) spectrum like the stream function, as opposed to a shallow (broad) spectrum like the vorticity. Similarly, other averaging (integrating) procedures, such as taking zonal (eastward) and/or temporal means, would obscure, possibly mislead, the analysis of the simulation if non-averaged “higher-order” fields like vorticity are not considered concomitantly.

It should be emphasised that, in contrast to what might be the customary view, numerical noise and blow-ups are useful. Simulations with severe forcing should be *allowed* to crash—or at least halted, when near grid-scale oscillations are visible in the flow field. Any phenomena observed thereafter would be seriously compromised in accuracy, and quite possibly entirely artifactual [Boyd, 2000]. In numerical work, it is easy



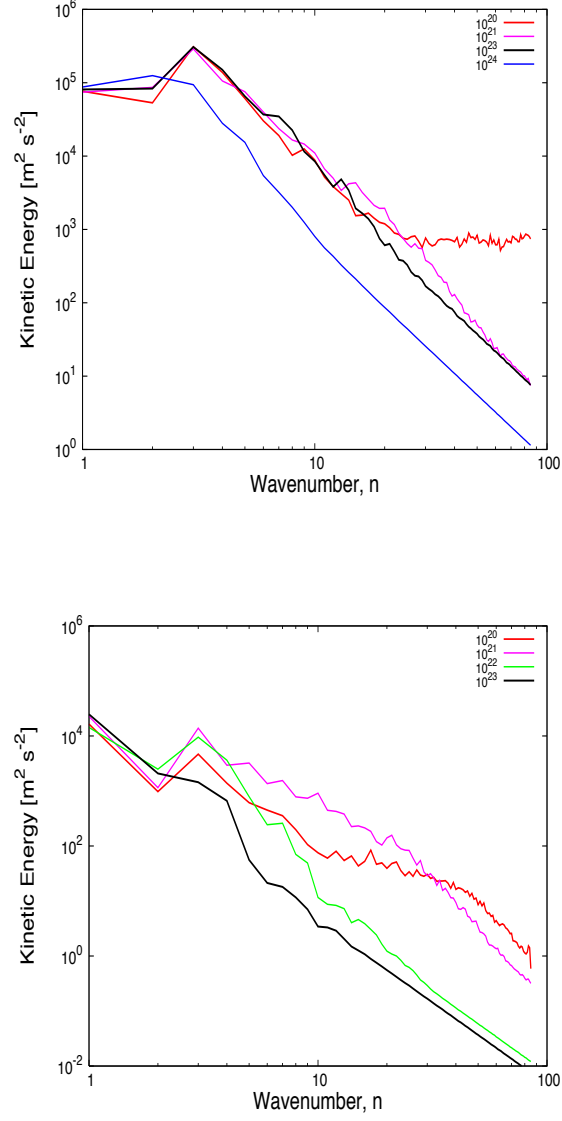


Figure 4.2: Kinetic energy spectra for the fields shown in Figure 4.1 for simulations that are set up identically, except for the artificial viscosity and the thermal relaxation time. The runs shown in the upper panel have a relaxation time of  $\tau_{th} = 0.1 \tau_p$  while the runs on the lower panel have  $\tau_{th} = 3 \tau_p$ . The different coloured lines are for different values of  $\nu$ , as indicated in the legend. Note the different scales on the two panels—much more kinetic energy is contained in the flow when the relaxation time is short. The spectra reveal both under-dissipated (e.g. red line, left panel) and over-dissipated (e.g. blue line, left panel) flow fields. A  $\nu$ -value that seems to give a reasonable spectrum for the short  $\tau_{th}$  (e.g. black line, upper panel) results in over-dissipation for the longer  $\tau_{th}$  (black line, lower panel).

to get lured into believing a calculation by not heeding important telltale signs.

As already mentioned, there is a rational way to diagnose the onset of the small-scale error sources—as well as the excessive dissipation—in a simulation. This is illustrated in Figure 4.2, which contains the kinetic energy spectra of the fields presented in Figure 4.1. Kinetic energy spectra have not been shown before in publications of extrasolar planet atmosphere flow simulations. They provide an important diagnostic, when used in conjunction with instantaneous fields (see, e.g., *Cho and Polvani* [1996] and *Koshyk et al.* [1999] for a discussion of kinetic energy spectra and horizontal diffusion), and can be used to choose an appropriate  $\nu$  value.

The upper set of spectra in Figure 4.2 corresponds to runs with the shorter  $\tau_{\text{th}} = 0.1 \tau_p$  in the left column of Figure 4.1, and the lower set of spectra in Figure 4.2 corresponds to runs with the longer  $\tau_{\text{th}} = 3 \tau_p$  in the right column of Figure 4.1. Visual inspection of the vorticity fields along the left column of Figure 4.1 suggests the runs in panels (a) and (c) are not much affected by the small-scale oscillations [if at all in the run of panel (a)]. This can be quantified by confirming that the corresponding spectra in Figure 4.2 (upper panel) are the blue and black lines (runs N1a and N3a, respectively). In fact, the blue line clearly reveals a case of over-damping, in which all scales are less energetic than the corresponding scales in the other runs.

In contrast, note the appearance of near-grid-scale waves in physical space, for the run in panel (i) in Figure 4.1, indicated by a tendency for the spectrum (red line in upper panel of Figure 4.2) to peel off and curl up near—and considerably to the left (larger scale) of—the aliasing limit; this is

$$n_a = \frac{2\pi R_p}{3\Delta x},$$

which is  $\approx 85$  in our case, since  $\Delta x$  is chosen to be “alias-free” up to  $n_t$  [Orszag, 1971]. Clearly, our de-aliasing procedure, of inverse transforming onto a physical grid that is  $3n_t + 1$  around the longitude, is not successful in runs N5a and N4a, as well as in run N3a (spectrum not shown). This is because increasingly greater resolution is needed as the calcula-

tion proceeds, as discussed below. In turbulence simulations, this peeling off behaviour is known as an “energy pile-up” or “spectral blocking” (because direct energy cascade to high wavenumbers in three-dimensional turbulence is blocked). It is not limited to spectral methods. It is universal to all methods which discretise space.

Spectral blocking can cause numerical instability in the time integration of any nonlinear equations. The instability arises due to the quadratically nonlinear term in the solved equations. For example, a typical quadratically nonlinear term (in one-dimensional Cartesian geometry for simplicity) gives:

$$\psi \frac{\partial \psi}{\partial x} = \left( \sum_{p=-K}^K a_p e^{ipx} \right) \cdot \left( \sum_{q=-K}^K i q a_q e^{iqx} \right) = \sum_{k=-2K}^{2K} b_k e^{ikx}.$$

Here,  $\psi(x, t)$  is an arbitrary one-dimensional scalar function, which is Fourier expanded;  $b_k$  are given by a sum over the products of the  $a_k$ ;  $K$  is the truncation wavenumber, corresponding to  $n_t$  in equation (4.5). Note that the nonlinear interaction generates high wavenumbers,  $k > K$ , which will be aliased into wavenumbers on the range  $k \in [-K, K]$ . This induces an unphysical inverse cascade of energy from high wavenumbers to low wavenumbers.

It is important to realise that the above cascade injects artificial energy into *all* scales. The injection is simply more noticeable in the small scales since not much energy is contained there in the absence of blocking. Oscillations of size  $l = O(\Delta x)$  are a precursor to breakdown of computational fidelity. These oscillations are insidious because they require higher and higher resolution in the calculation over time. Without the increasing resolution, they deteriorate the accuracy of the simulation on all scales as the calculation proceeds, as pointed out in *Thrastarson and Cho* [2010]. Although some blocking is almost inevitable in a long time integration of a nonlinear system (unless the dissipation is unrealistically large), it can be monitored and controlled—albeit better in some methods than in others.

The upper and lower panels of Figure 4.2 reveal not only how the appropriate dissipation can be chosen, but also the crucial interplay between the small-scale noise and  $\tau_{th}$ —hence, underscoring the importance of using *both* the spectra and the physical field in analysing a calculation.

Consider, for example, the “optimal” calculation (i.e., least affected by too much or too little dissipation) for the short  $\tau_{th}$  runs. The calculation with  $\nu_4 = 10^{23} \text{ m}^4 \text{ s}^{-1}$  (black line in the upper panel) is devoid of non-physical build up of energy at the smallest scales while still retaining the same amount of energy in the large scales as in the calculations with smaller  $\nu$ . On the other hand, the calculation with longer  $\tau_{th}$  but same  $\nu$  (black line in the lower panel) is clearly over-dissipated, containing less energy compared to the other calculations on essentially all the scales. Hence, if the  $\nu$  value were “tuned” with the calculations with shorter  $\tau_{th}$  (only), then a calculation with a different  $\tau_{th}$ —say a longer one, as in this example—would be over-damped. In other words, a correct  $\nu$  value which is independent of  $\tau_{th}$  cannot be obtained:  $\nu = \nu(\tau_{th}, \epsilon, \dots)$ , where “ $\dots$ ” includes  $T_e$ ,  $R_p$ , semi-implicitness, etc.

The above behavior is generic. Simulations performed with a greater range of  $\tau_{th}$  (down to  $0.01 \tau_p$ ) and  $\nu$  and  $p$ , exhibit the same basic behaviour; and, it is present throughout the model domain; grid-scale oscillations can appear in the duration of a calculation anywhere in the domain. These oscillations can be controlled to some degree in mild cases, as outlined above. However, grid-scale oscillations can be dominant near the top of the domain for many values of  $\nu$  considered. In this situation, it is common in GCM studies to include a “sponge layer”, where dissipation is artificially enhanced in the topmost layers. While this can damp unphysical oscillations, it can also have spurious effects.

Figure 4.3 shows how the spectrum is affected when the form of the artificial viscosity is of lower order. The blue and black lines (runs N1a and N2a, respectively) are the same as in the top panel of figure Figure 4.2. They can be compared to the red line (run N6a), which shows the spectrum from a simulation that is identical to the other two runs in the figure, except for the value of  $\nu$  and the order of the viscosity operator (here  $p = 1$ ). In this case, the energy in the small scales (high wavenumbers) is dissipated much more strongly. More importantly, essentially *all* wavenumbers are affected by the lower order viscosity; and, as discussed in *Cho and Polvani* [1996], the slope of the spectrum becomes steeper—even at wavenumbers well below the truncation scale.

The simulations described above are, as is common in the literature,

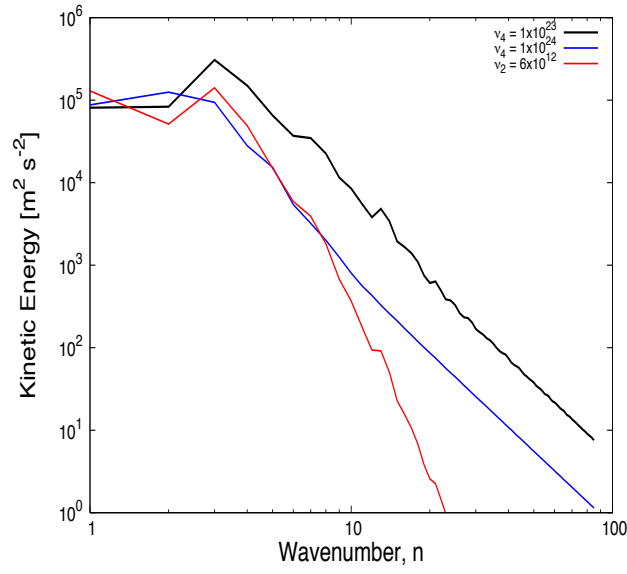


Figure 4.3: Kinetic energy spectra for simulations that are set up identically, except for the artificial viscosity. The different lines refer to different values of  $\nu$ , as indicated in the legend. The blue and black lines are the same as in the upper panel of Figure 4.2, for which the viscosity is of biharmonic form ( $\nabla^4$  with  $p = 2$ ). But, the red line is for a simulation where the order of the viscosity is lower ( $p = 1$ ), the normal Newtonian viscosity.

initialised close to a resting state and very suddenly subjected to forcing with large day-night gradients. This creates a highly unbalanced flow which is a likely source of fast gravity waves and ultimately noise if the waves are not well resolved. Turning the forcing on more gradually thus seems a better approach to avoid generation of spurious waves. To address this issue, additional simulations were performed (at T21 resolution) where the forcing was gradually ramped up.

A simulation was performed where  $\tau_{\text{th}}$  was linearly decreased from  $10 \tau_p$  to  $0.01 \tau_p$  over the first  $100 \tau_p$  of the simulation, with the value fixed at  $0.01 \tau_p$  thereafter. The setup for this simulation was otherwise identical to that of run N3a (with  $\nu = 10^{22}$ ). This ramped-forcing simulation was compared to runs that were identical except the value of  $\tau_{\text{th}}$  was fixed from the start. The simulation with fixed  $\tau_{\text{th}} = 0.01 \tau_p$  was severely noisy, whereas a run with fixed  $\tau_{\text{th}} = 3 \tau_p$ , but the same  $\nu = 10^{22}$ , was not. At time  $t = 150 \tau_p$ , well after the ramping period, the ramped-forcing simulation had settled into a state that was indiscernible from the case where  $\tau_{\text{th}}$  was fixed at  $0.01 \tau_p$  from the start. The amount of noise was no less, so the ramping of the forcing did not make a noticeable difference in this case. The same was true when  $\Delta T_e$  was also ramped linearly from 0 to 500 K over the first  $100 \tau_p$  of the simulation. Hence, this simple ramping was not found to alleviate the problems associated with the short  $\tau_{\text{th}}$  and large  $\Delta T_e$ . Nevertheless, further experiments with ramping of the forcing or initialising from balanced states, are an important development for improved future simulations, especially if the forcing is strong.

### 4.3.2 Temporal Dissipation

If the solved equations support several types of waves, as with the primitive equations, the maximum stable timestep is limited by the Courant number,

$$\mu^* \equiv c_{\text{max}} \left( \frac{\Delta t}{\Delta x} \right),$$

where  $c_{\text{max}}$  is the maximum horizontal wind speed associated with the fastest propagating wave. Some fast waves are of little physical significance, but they enslave  $\Delta t$  to be small. Implicit schemes do permit a

larger timestep size to be used than in explicit schemes, often making the former more computationally efficient. However, for nonlinear equations, implicit schemes have a high cost per timestep because a nonlinear boundary value problem must be solved at each timestep.

As noted, a semi-implicit algorithm is commonly used in GCMs. In general, the implicit and explicit parts in the algorithm may be of same or different order. Treating some terms explicitly while others implicitly may appear strange, but there are some major advantages. First, because the nonlinear terms are treated explicitly, it is only necessary to solve a *linear* boundary value problem at each timestep. Second, the (hyper)dissipation terms, which involve even number of derivatives, impose a much stiffer timestep requirement than the advective terms; for example,  $\Delta t$  is  $O(1/N^4)$  and  $O(1/N^2)$ , respectively, for the Newtonian viscosity ( $p = 1$ ). Hence, the semi-implicit algorithm stabilises the most unwieldy terms. Third, in general circulation and other fluid dynamics problems, advection is crucial; therefore, it is important to use a high order time-marching scheme with a short timestep to accurately compute phenomena or structures such as frontogenesis, advection of storm systems, and turbulent cascades. There is little advantage in treating the nonlinear terms implicitly because a timestep longer than the explicit advective stability limit would be too inaccurate.

Note that, although it is possible to treat the time coordinate spectrally, it is generally more efficient to apply spectral methods to the spatial coordinates only because time marching is usually much cheaper than computing the solution simultaneously over all space-time. In general, much less concern is given to the temporal accuracy than the spatial accuracy of GCMs—usually with good justification: spatial errors pose greater problems, especially for the short and medium range duration runs typically performed with the models. This obviously does not apply for long duration runs, particularly if quantitative predictions are sought [Thrustarson and Cho, 2010].

As already discussed, a computational mode arises in the leapfrog scheme, which is an example of a two-step scheme:

$$\Psi^{n+1} = \Psi^{n-1} + \mathcal{F}(\Psi^n, \mathbf{x}, t^n; \epsilon), \quad (4.10)$$

where  $\mathbf{x} \in \mathbb{R}^2$ ; recall that  $\epsilon$  is the Robert-Asselin time filter coefficient. Computational modes arise in all multistep methods. Fortunately, in some multistep methods  $\Delta t$  can be chosen to keep the amplitude of the modes from growing. However, the leapfrog scheme is unstable for diffusion, for all  $\Delta t$ . For this reason, the diffusion part of the equations is “time-lagged” by evaluating the diffusion terms at the time level  $(n - 1)$ . This effectively time-marches the diffusion part by a first-order scheme.

The Robert-Asselin filtered leapfrog scheme has been analysed by *Durran* [1991] for the simple oscillation equation,

$$\frac{d\psi}{dt} = i\omega\psi, \quad (4.11)$$

where  $\omega$  is the frequency of oscillation. That analysis shows that, in the limit  $\omega\Delta t \ll 1$ , the relative phase-speed error of the physical mode is

$$\mathcal{R}_{\text{phys}} = 1 + \left[ \frac{1 + 2\epsilon}{6(1 - \epsilon)} \right] (\omega\Delta t)^2. \quad (4.12)$$

Therefore, the phase of the numerical solution leads the actual solution in time, and the error increases with larger  $\epsilon$ . No analysis exists to guide in choosing  $\epsilon$ . Hence, it is important to assess the sensitivity of the simulations to the filter *for each problem considered*. Accordingly, in this work, we have performed a series of simulations in which  $\epsilon$  has been varied while keeping everything else fixed, for different values of relaxation time  $\tau_{\text{th}}$ . The simulation parameters are summarised in Table 4.2.

Figure 4.4 shows the evolution of the Courant number  $\mu^*$  for simulations with different  $\epsilon$ , for two sets of runs with different values of  $\tau_{\text{th}}$  in each set. Note that for clarity each time series in a set has been offset vertically by 0.1 in the plot; and, the two sets, as groups, have been offset vertically by 0.5. At the T21 resolution of the runs shown, for  $\tau_{\text{th}} = 3\tau_p$  and  $\nu = 10^{22} \text{ m}^4 \text{ s}^{-1}$ , it is found that a value of at least  $\epsilon = 0.002$  is needed to prevent the simulation from succumbing to time-splitting instability.

With shorter relaxation time ( $\tau_{\text{th}} = 0.1\tau_p$ ), a *larger* value of  $\epsilon$  is required for the simulation to proceed without blowing up. This is perhaps not surprising, in light of the preceding discussion. But, remarkably, even without explicit numerical viscosity turned on (i.e.,  $\nu$  set to 0), the simulation can proceed without crashing; and, this is so despite the fact that the physical field is completely swamped with noise! When  $\tau_{\text{th}} = 3\tau_p$ ,



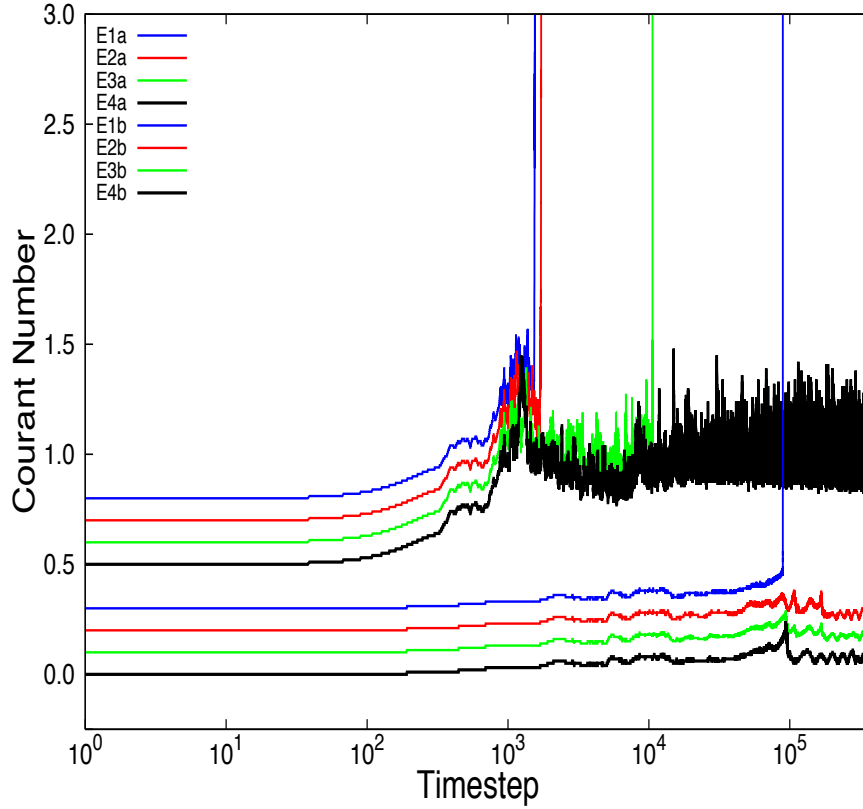


Figure 4.4: Courant number as a function of time for two sets of runs with different values of  $\tau_{th}$  in each set. The four runs within each set have different  $\epsilon$  values, setting the strength of the Robert-Asselin time filter. For clarity each time series in a set has been offset vertically by 0.1 in the plot; and, the two sets, as groups, have been offset vertically by 0.5. The lower set of runs have  $\tau_{th} = 3 \tau_p$ , while the upper set of runs have  $\tau_{th} = 0.1 \tau_p$ . For each set the run with  $\epsilon = 0.001$  is indicated with a blue line,  $\epsilon = 0.002$  a red line,  $\epsilon = 0.006$  a green line, and  $\epsilon = 0.01$  a black line.

Table 4.2: Summary of Runs for Time Filter Sensitivity.

Run	$\epsilon$	$\tau_{\text{th}}/\tau_p$	Notes
E1a	0.001	.1	blow-up ( $t = 1 \tau_p$ )
E1b	0.001	3	blow-up ( $t = 71 \tau_p$ )
E2a	0.002	.1	blow-up ( $t = 1 \tau_p$ )
E2b	0.002	3	
E3a	0.006	.1	blow-up ( $t = 8 \tau_p$ )
E3b	0.006	3	
E4a	0.01	.1	
E4b	0.01	3	
E5a	0.06	.1	
E5b	0.06	3	
E6a	0.1	.1	
E6b	0.1	3	

Notes:  $\tau_{\text{th}}/\tau_p$  is the thermal relaxation time in units of planetary rotations, and  $\epsilon$  is the Robert-Asselin filter coefficient. All the runs are at T21 resolution and have  $\nu_4 = 10^{22} \text{ m}^4 \text{ s}^{-1}$ . The timestep is  $\Delta t = 240 \text{ s}$ .

runs do not crash as long as  $\epsilon \geq 0.006$ . However, with  $\tau_{\text{th}} = 0.1 \tau_p$ , the minimum  $\epsilon$  for not crashing is an order of magnitude greater. Evidently, an  $\epsilon$  value used in earlier studies of Earth's atmosphere should be adjusted when adapting an Earth GCM for extrasolar planet study. In general, a shorter  $\tau_{\text{th}}$  or lower viscosity requires stronger Robert-Asselin filtering to prevent blow-up.

Note that the Courant-Friedrichs-Lewy (CFL) criterion for stability of the leapfrog scheme [Durrant, 1999],

$$\mu^* \leq \frac{1}{\pi},$$

can sometimes be exceeded in the middle of a run, even though the simulation is stable at  $t = 0$  (cf., run E3a in Figure 4.4). This is because the advective time-stepping limit depends on the maximum speed  $c_{\text{max}}$ , which can increase during the evolution of a flow. Careful monitoring of the physical fields shows a zone of intense shear between the two vortices generating small-scale oscillations that rapidly amplify until the simulation becomes nonsense. The culprit is not lack of spatial resolution or a blocked turbulent cascade, in this case, because the calculation can be

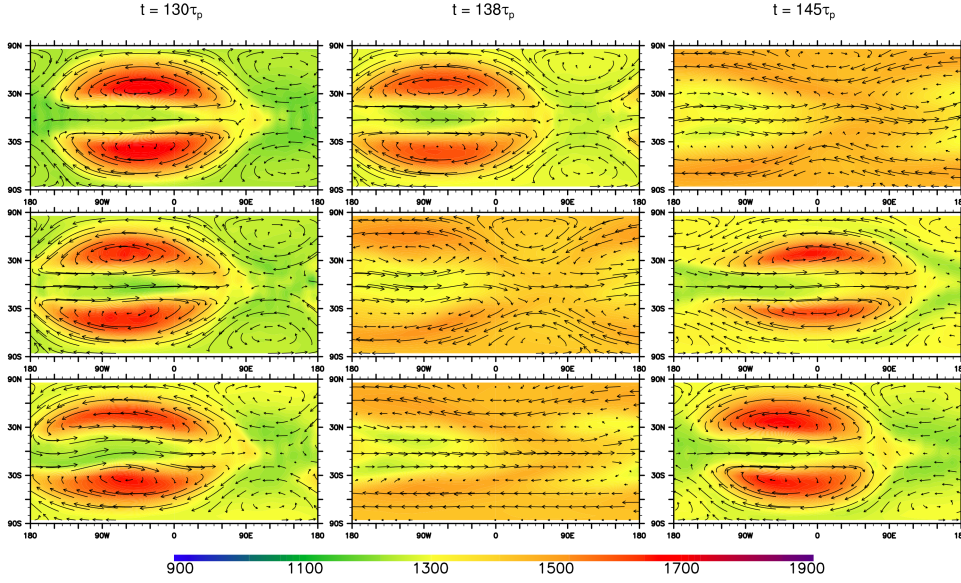


Figure 4.5: Temperature (color coded in K) with streamlines overlaid, for three simulations differing only in the value of  $\epsilon$ , shown at three moments in time. From left to right, the snapshots are taken at  $t = \{130, 138, 145\}\tau_p$ . The top row is from a run with  $\epsilon = 0.01$ , the middle row with  $\epsilon = 0.06$  and the bottom row  $\epsilon = 0.10$ . All the fields are shown at the  $p \approx 900$  mb level. The substellar point is at  $0^\circ$  longitude and latitude.

extended indefinitely by halving the timestep.

Figure 4.5 illustrates the sensitivity of the evolution to  $\epsilon$  for the range,  $\epsilon \in [0.01, 0.1]$ . Although the resolution in these calculations is only T21, they illustrate the point. Snapshots of the flow field are shown at three successive times for three simulations, differing only in the value of  $\epsilon$ . Similar flow patterns emerge in all the simulations: they all exhibit a cyclic behaviour with vortices translating around the planet, undergoing large variations in strength and size as they do so, with corresponding changes in the temperature field. However, *at a given instant* the flow and temperature fields look different between the three runs. At  $t = 130\tau_p$ , in all the runs there is a warm cyclone pair centred west of the substellar point. And in all the runs, the cyclones move westward and the flow and temperature fields undergo substantial changes before eventually returning to a similar state, 15–20 planet rotations later. But at  $t = 145\tau_p$ , the run with the largest  $\epsilon$  has already returned to a state similar to that at  $t = 130\tau_p$ , while the runs with smaller  $\epsilon$  take longer to complete their cycles.

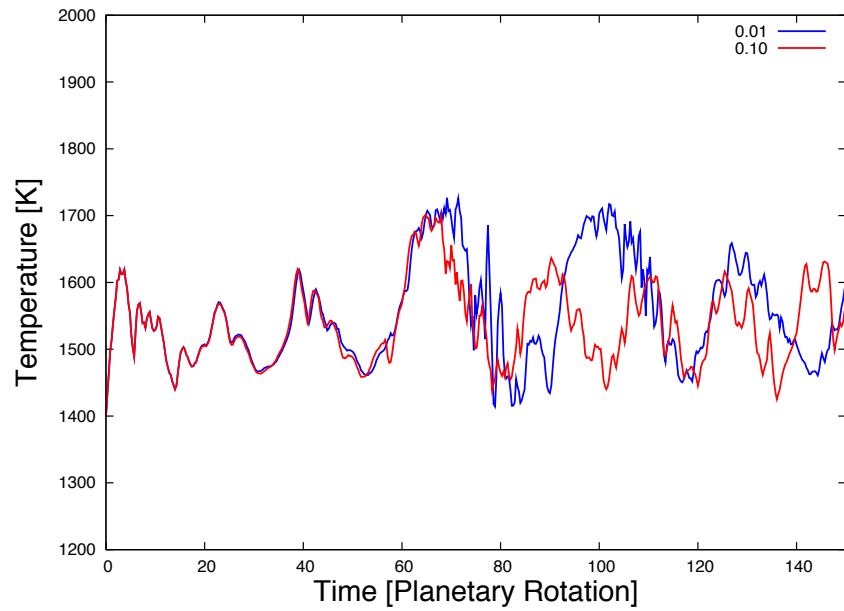


Figure 4.6: Temperature at a fixed point, at  $0^\circ$  longitude and  $30^\circ$  latitude, as a function of time for the first 150 planet rotations in two simulations. The two curves show results of simulations that are identical apart only from the strength of the Robert-Asselin time filter. The red curve is from a run with  $\epsilon = 0.10$ , and the blue curve from a run with  $\epsilon = 0.01$ .

Figure 4.6 shows the behaviour more clearly. The temperature at a point on the model planet atmosphere ( $0^\circ$  longitude,  $30^\circ$  latitude) evolves in time for two simulations which have identical parameters, except for  $\epsilon$ . The two runs match nearly exactly until about  $45 \tau_p$ , when the two runs start to deviate—in the beginning only slightly. But, at about  $70 \tau_p$  the temperature oscillations in the run with the larger  $\epsilon$  lead in phase, compared to the run with smaller  $\epsilon$ . This behaviour agrees qualitatively with Equation 4.12. Over long timescales the three simulations exhibit similar qualitative behaviour, although amplitudes, phases, and periodicities of the flow and temperature fields are not quantitatively the same. As noted, simulations shown in Figures 4.5 and 4.6 are at T21 resolution, but with higher resolution deviations appear even earlier. Based on the above behaviour, it is reasonable to select the smallest filter coefficient that does not result in blow-up, to minimise errors.

In *Showman et al.* [2009], the MITgcm [Adcroft et al., 2004] is used. In that study, the model employs the third-order Adams-Bashforth method, which has some attractive properties [Durran, 1991]. However, the scheme does require an initialisation phase in which  $\Psi^1$  and  $\Psi^2$  are computed from the initial condition  $\Psi^0$  by some other procedure, such as the fourth-order Runge-Kutta or a first- or second-order scheme with several short timesteps. It should be emphasised that—as *it is a major point of this chapter*—the main concern is usually adequate spatial resolution, especially in problems with inherent small-scale phenomena, not the time-integration. A second- or even first-order time-integration scheme can be perfectly adequate for many purposes.

## 4.4 Conclusion

A major aim of this chapter has been to shed light on some crucial aspects for numerical modelling of atmospheric circulation on hot extrasolar planets. It has been argued that, a spectral model offers advantages in accuracy and diagnostics, given that the higher-order field and wavenumbers are what's actually evolved. However, all numerical models, including spectral models, have limitations in how well they can represent physical reality. Moreover, the models can easily be applied outside the realm of

“safe parameters” and produce results that are nonsensical. The challenge is to properly test and identify the limits. When numerical artefacts appear, it is important to know how to deal with them and to know when a simulation should be discarded.

In this chapter it has been demonstrated that, for hot extrasolar planets simulations with stationary forcing, there is a strong sensitivity to the strength of applied artificial viscosity. In addition, there is a relation between the thermal relaxation time  $\tau_{\text{th}}$  and the viscosity  $\nu$ : small  $\tau_{\text{th}}$ ’s lead to a large amount of unphysical, grid-scale oscillations in the simulation, which forces the use of excessive amounts of artificial viscosity to quench the oscillations. Hence, using a fixed strength of artificial viscosity in a simulation with a large range of  $\tau_{\text{th}}$  in the model domain (e.g., from about an hour to tens of days)—as done in many simulations in the literature—inevitably produces flow and temperature fields, which are either dominated by unphysical noise or over-damping. One may then wish to apply a spatially varying  $\nu$ , but clearly this is then motivated by a numerical basis rather than a physical one.

The proper values to use for the relaxation time (or variables needed for realistic radiative transfer) are not known. Based on the findings in this work, calculations with extremely short  $\tau_{\text{th}}$ ’s warrant further scrutiny. Current GCMs may not be standing up too well to this stressful test. If, however, the short  $\tau_{\text{th}}$  are really *physically* relevant, then another form of heating/cooling parameterisation or setup is needed. This is not a criticism of the Newtonian relaxation scheme, which in fact has been (and continues to be) very useful for understanding basic mechanisms.

One solution could be to spatially vary the  $\nu$ , as already discussed; but, this would lead to further complexity. Even if direct radiative transfer is incorporated, one must ensure that the forcing is not too violent or strong (large amplitude and short timescale). The  $\nu$  values used in our study correspond to dissipation time scales for the highest resolved wavenumber ranging from a few seconds to a few hours. And, indeed, a comparison with calculations for the Earth shows that we have had to use  $\nu$  values higher (leading to shorter dissipation time scales) than that normally used in Earth studies [Collins *et al.*, 2004]. As discussed in Cho *et al.* [2008], if the radiative processes appear as practically instantaneous from the per-

spective of the flow, then an adiabatic approach is more appropriate. Certainly from a numerical accuracy standpoint, as motivated by the present work, adiabatic and “gently forced” calculations are useful as baselines. Else, gradually ramping up heating and/or initializing simulations close to a balanced state is necessary [*Thrastarson and Cho*, 2010].

GCMs of extrasolar planet atmospheres have great value in helping to guide and interpret observations. It is then important to critically examine the effects of the numerous parameters that are specified. This is particularly crucial when applying the models to a “new regime”, where the physical conditions differ markedly from a traditional (e.g., Earth) one. In this paper we have shown examples of how a commonly-used forcing can steer GCMs to produce misleading results and how numerical expediences, such as the Robert-Asselin filter, can produce slewing frequency as well as the well-known damping and phase-errors [*Durran*, 1991; *Williams*, 2009]. In addition, we have discussed diagnostics procedures to better assess the quality of a simulation using the vorticity field and energy spectra. Reliance on spatial and temporal averages can effectively conceal telltale signs that a simulation is not trustworthy.

A simulation which is properly resolving the flow should approximately conserve energy for a long time, particularly in freely-evolving (unforced) conditions. This should be so even if the mentioned conservation property is not explicitly built into the discretisation algorithm, as in the scheme of *Arakawa* [1966] [this scheme conserves the domain-integrated energy *and* enstrophy ( $\frac{1}{2}\zeta^2$ ) in the nonlinear advection term]. For only then can we trust that a calculation is not artificially driven to an unphysical region in the solution space.

## Chapter 5

# Coherent States and Internal Variability

For extrasolar planets on close-in orbits, the heating condition, where the same hemisphere may be perpetually and intensely heated, is one of the aspects that sets them apart and makes them so interesting. However, for models of their atmospheric circulation, the appropriate specification of the thermal forcing is not yet constrained by observations. In this chapter I describe simulations where the strength of the thermal forcing, represented by Newtonian thermal relaxation, is systematically varied for an idealised tidally locked extrasolar giant planet. Distinct long-lasting stationary and oscillatory states are identified for different sets of forcing parameters. In addition, multiple statistically steady states are observed for a *given* forcing. For a given forcing, varying initial conditions leads to different states, but a given run also exhibits transitions between distinguishable long-lasting (hundreds or thousands of planet rotations) states during its long term evolution.

Most of the identified states are time variable in a periodic manner. In all of the simulations large scale vortices, or storms, form. They are dominant features of the flow and persist during most of the long-lasting states. The motion of the vortices is usually accompanied by an associated periodic variability in the temperature field. While these idealised calculations cannot be expected to give an accurate match to the actual state of the atmosphere of a particular planet, systematic studies of the parameter space provide valuable insights for guiding and interpreting observations.



For example, the storms and their associated variability can suggest plausible time scales of variability, and provide a strong argument in support of repeated measurements of a given planet, in future observational studies.

## 5.1 Introduction

The general circulation of a planet's atmosphere can be regarded as a statistically steady solution to a complex, forced boundary-value problem. The question whether the observed solution is unique for a given forcing and boundary conditions, has been asked by many investigator's in the past.

For idealised conditions relevant to Earth's atmosphere, *Charney and Devore* [1979] showed that multiple stable equilibrium states are possible for a given forcing. They showed this both analytically and numerically for topographic forcing, and analytically in the case of thermal forcing, by using highly truncated spectral expansions and performing stability analyses on quasi-geostrophic equations for a barotropic channel flow on the  $\beta$ -plane.

*Suarez and Duffy* [1992] found a bifurcation of circulation regimes for model conditions relevant for Earth's atmosphere, which was also studied by *Saravanan* [1993]. They found that the general circulation in their simulations changed abruptly from a regime close to the observed state, to a superrotating regime, when heating rate was increased past a threshold value. At low resolution these cases showed hysteresis, where the simulation would stay in the superrotating regime when the heating rate was decreased again below the threshold.

Similar questions are also relevant and crucial for studies of other planets, in other circulation regimes, with different forcing and boundary conditions. More recently, *Edson et al.* [2011] discussed multiple equilibria for specific types of terrestrial exoplanets. Arguably it is even more important to look for, and be aware of, multiple equilibria when exploring new regimes which may not be as well constrained by observations as they are for the Earth.

For close-in extrasolar giant planets (CEGPs) the appropriate specification of thermal forcing is unknown. While many of these planets are

expected to have permanent daysides that are perpetually irradiated by the host star, the distribution of radiatively active species and other factors that determine the heating and cooling of the atmosphere, are very poorly constrained. In this chapter, we use the simple Newtonian thermal relaxation scheme and explore the quasi-stable states that are reached when the strength of the thermal forcing, specified by the relaxation time and amplitude of the equilibrium temperature profile, is varied between simulations. In Chapter 3 and *Thrastarson and Cho* [2010], sensitivity to initial conditions has been discussed. In addition to the various quasi-stable states shown there, I also describe here the evolution of selected simulations on extremely long time scales (more than  $80000 \tau_p$ ), and discuss transitions between long-lived states within a given simulation with fixed parameters.

Giant planets in our own solar system are home to violent weather systems, large storms that last for hundreds of years as well as smaller ones that come and go almost at random. Such systems are responsible for redistributing energy from the Sun and determining the physical conditions across the atmosphere. This raises the question of how stable – and variable – atmospheric systems are on exoplanets.

Some of the simulations of CEGP atmospheric dynamics, reported in the literature, have shown little signs of time variability [*Showman et al.*, 2008a, 2009; *Rauscher and Menou*, 2010]. However, the high horizontal resolution, equivalent-barotropic simulations of *Cho et al.* [2003, 2008], showed variability. These simulations included a representation of the forcing in the adiabatic limit, for HD 209458 b-like parameters. The variability was especially in connection with high-latitude vortices revolving around the poles and wave breaking at mid and low latitudes. *Menou et al.* [2003] applied these results to other CEGPs and argued that variability should apply to a wide range of CEGPs. *Rauscher et al.* [2007] discussed the observational consequences of the variability in the *Cho et al.* [2003] simulations, and concluded that it could result in eclipse depth variability that would be within the reach of Spitzer measurements.

A common feature of the long-lasting states reached in the simulations considered in this chapter, are large scale vortices, both at high and low latitudes, and an associated time variability, and in the following sections this variability is characterised. Before that, Section 5.2 introduces past

studies of the response to zonally asymmetric heating and relevant wave types. In Section 5.3, the setup of the simulations is specified. The results of simulations with varying forcing strength are presented in Section 5.4.1, and Section 5.4.2 is focused on the very long term evolution of selected cases. The implications of the vortices, or storms, that characterise most of the states, are discussed in Section 5.4.3, before concluding in Section 5.5.

## 5.2 Zonally Asymmetric Heating and Waves

The major types of waves in stratified, rotating planetary atmospheres, are Rossby planetary waves and gravity waves. For Rossby waves, which are usually large in scale, the gradient of the Coriolis force provides the restoring mechanism. For gravity waves, buoyancy acts as the restoring force. They are usually small-scale, but on larger scales inertia-gravity waves, which feel the effects of rotation and geometry as well as buoyancy, can be important.

For the simplified setup of a single homogeneous, unforced and inviscid layer on a flat bottomed  $\beta$ -plane (where the meridional gradient of the Coriolis parameter is assumed linear,  $f = f_0 + \beta y$ , with  $\beta = \partial f / \partial y$ ), Rossby waves are a solution to the equation of motion linearised about a time-independent basic state [e.g., Vallis, 2006]. In this case the dispersion relation for the Rossby waves is

$$\omega(k, l) = Uk - k \frac{\beta + Uk_d^2}{K^2 + k_d^2}, \quad (5.1)$$

where  $\omega$  is the frequency,  $K = \sqrt{k^2 + l^2}$ ,  $k$  and  $l$  are the zonal and meridional wave numbers, respectively,  $U$  is the zonal flow of the basic state, and  $k_d = 1/L_d$ , where  $L_d$  is the deformation radius (see Section 2.2).

*Matsuno* [1966] used a simple analytic model to study wave motions in the equatorial region and steady solutions when zonally asymmetric (longitudinally varying) forcing is applied. He considered a single layer of homogeneous, incompressible fluid with a free surface, i.e., a fluid governed by the shallow water equations, on a  $\beta$ -plane. A mass source and sink were placed along the equator, as a representation of thermal forcing, and a linear drag was applied. Solutions were found which consisted

of a long Rossby wave propagating westward, and a faster Kelvin wave propagating eastward.

The Kelvin wave is a type of gravity wave that exists in the presence of rotation and decays away from the equator. It has weak meridional winds but strong zonal winds. At low latitudes the solution is a superposition of the two waves in the forcing region, but at higher latitudes the Rossby wave response is more dominant. *Gill* [1980] extended this model (including forcing displaced off the equator) and applied it to explain features of the Earth’s tropical circulation. The understanding gained from these simple models has also been applied to explain features of more complex numerical calculations concerning the response to tropical heating in the Earth’s atmosphere [*Jin and Hoskins*, 1995]. *Showman and Polvani* [2010] and *Showman and Polvani* [2011] used models similar to the Matsuno and Gill models, but accounting for vertical momentum exchange with an underlying quiescent layer, to study mechanisms for equatorial superrotation on CEGPs.

### 5.3 Model Setup

In the following sections, results are presented from simulations where the strength of thermal forcing is varied between simulations. In addition, the very long term evolution of simulations which have the same forcing but different initial conditions is described. In all these simulations, the primitive equations (Equations 2.34-2.41) are solved, with the boundary conditions  $D\eta/Dt = 0$ , in the domain from  $p = 2.2$  mbar to  $p \sim 1$  bar (the bottom surface pressure is initially 1 bar, but can vary in time). For the numerical calculations, CAM 3.0 is used, as described in Chapter 4, with planetary parameters based on observed or expected values for HD209458b (as in Table 3.1). The horizontal resolution is T85 for core simulations, but some tests and long term evolution studies are run at T21 resolution.

As in Chapters 3 and 4, the thermal forcing is represented by Newtonian relaxation, but the forcing term and equilibrium temperature profile are restated here for convenience. The forcing term in the temperature

equation is

$$\frac{\dot{q}_{\text{net}}}{c_p} = -\frac{1}{\tau_{\text{th}}} (T - T_e), \quad (5.2)$$

where  $T_e = T_e(\lambda, \phi, \eta, t)$  is the equilibrium temperature distribution and  $\tau_{\text{th}}$  is the thermal relaxation (drag or “cooling”) time. The equilibrium profile is given by

$$T_e = T_m + \Delta T_e \cos \phi \cos \lambda, \quad (5.3)$$

with  $T_m = (T_D + T_N)/2$  and  $\Delta T_e = (T_D - T_N)/2$ .  $\Delta T_e$  is varied between simulations, but otherwise the equilibrium profile is kept the same in all the simulations of this chapter, and no height dependence is assumed. Both  $\Delta T_e$  and  $\tau_{\text{th}}$ , which is also varied between simulations, are assumed constant in each run. In Table 5.1 the simulations considered in this chapter are summarised, and Table 5.2 shows the common numerical parameters for the simulations. The names of the runs are chosen so that higher numbers indicate larger  $\Delta T_e$ , lower case letters (a, b, c, d, e) indicate successively faster relaxation (smaller  $\tau_p$ ), and ‘\*’ refers to higher resolution runs.

The two runs F4cI and F4cII have everything identical except the initial flow configuration. Both runs have thermal relaxation times of  $0.5 \tau_p$ . F4cI is initialised with a small, random perturbation introduced in the flow. Specifically, values of  $u$  and  $v$  are drawn from a Gaussian random distribution centered on zero with a standard deviation of  $0.05 \text{ m s}^{-1}$ . All the other simulations in Table 5.1 are initialised in the same way, except for run F4cII. In this case the calculation is initialised with a zonally-symmetric, westward equatorial jet of the following form:

$$u_0(\phi) = U \exp \left\{ \frac{(\phi - \phi_0)^2}{2\sigma^2} \right\}, \quad (5.4)$$

where  $u(t=0) = u_0$ ,  $U = -1000 \text{ m s}^{-1}$ ,  $\phi_0 = 0$ , and  $\sigma = \pi/12$ . All cases are initialised from an isothermal state with the initial temperature  $T_0 = T_m = 1400 \text{ K}$ .

Table 5.1: Summary of Runs with Varied Forcing Strength

Run	$\Delta T_e$ [K]	$\tau_{th}$ [ $\tau_p$ ]	Resolution	Comments
F1b	50	3	T21	
F1b*	50	3	T85	
F1c	50	0.5	T21	
F1d	50	0.1	T21	
F1d*	50	0.1	T85	
F2b	100	3	T21	
F2d	100	0.1	T21	
F3b	150	3	T21	
F3d	150	0.1	T21	
F4a	500	10	T21	
F4b	500	3	T21	
F4b*	500	3	T85	
F4cI	500	0.5	T21	Initialised with weak noise
F4cII	500	0.5	T21	Initialised with a westward jet
F4d	500	0.1	T21	
F4d*	500	0.1	T85	
F4e	500	0.01	T21	

Table 5.2: Numerical Parameters for Runs with Varied Forcing Strength

	Symbol	Value	Units
Truncation wavenumber	$N$	85 or 21	
Number of layers		26	
Timestep	$\Delta t$	60 or 240	s
Artificial viscosity operator	$\nabla^4$		
Superviscosity coefficient	$\nu$	$10^{22}$	$\text{m}^4 \text{s}^{-1}$
Robert-Asselin filter coefficient	$\epsilon$	0.06	

## 5.4 Results

### 5.4.1 States for Varied Forcing Strength

Figures 5.1-5.4 show results from simulations at four different points in the  $(\tau_{\text{th}}, \Delta T_e)$  parameter space (runs F1b\*, F4b\*, F1d\* and F4d\*). In all these runs, after an initial transient period of a few tens of rotations, a stationary or oscillatory state is reached, which lasts for at least a few hundred rotations. The upper panels of Figures 5.1-5.4 show snapshots of the temperature and wind fields that are representative of these states, at high and low altitude for each run. Note that the scales are not the same in all the figures (to emphasise contrasts and qualitative character). The temporal behaviour of each of the oscillating states is captured in Figures 5.5–5.8.

In the limit of weak forcing (run F1b\*, small  $\Delta T_e = 50$  K, slow  $\tau_{\text{th}} = 3 \tau_p$ ), the atmosphere settles into a baroclinic stationary state, shown in Figure 5.1. The flow is characterised by 4-6 vortices at each level and an undulating, high-latitude eastward jet. Both the flow and temperature fields vary with height, but with a low vertical mode (e.g. the equatorial flow turns from east to west with height, but only once). Compared to the other runs, wind speeds are relatively low ( $\sim 100$  m/s or less).

The state reached when  $\Delta T_e$  is greater (run F4b\*,  $\Delta T_e = 500$  K, slow  $\tau_{\text{th}} = 3$  rots) is shown in Figure 5.2. It is characterised by vertically tilted vortex columns, forming a quadrupole, i.e., a pair of cyclones and a pair of anticyclones at each height. Both the flow and temperature exhibit a cyclic behaviour, as shown in Figure 5.6 for the  $\eta = 0.83$  level. The mid- to high-latitude westward flow forms a wavy jet, with one trough for which the meridional amplitude varies as the wave travels westward. As the wave travels, the vortices on the jet flanks translate, elongate in the zonal direction, and reform, with large corresponding changes in the temperature field. These cycles have a period of roughly 20 rotations and persist for many hundreds of rotations.

For faster  $\tau_{\text{th}}$ , but small  $\Delta T_e$  (run F1d\*,  $\Delta T_e = 50$  K, fast  $\tau_{\text{th}} = 0.1$  rots), a cyclic state is also reached. Also here, as shown in Figure 5.2, a quadrupole of vortex columns is a dominant flow structure. However, in this case, both the flow and temperature are quite well aligned vertically

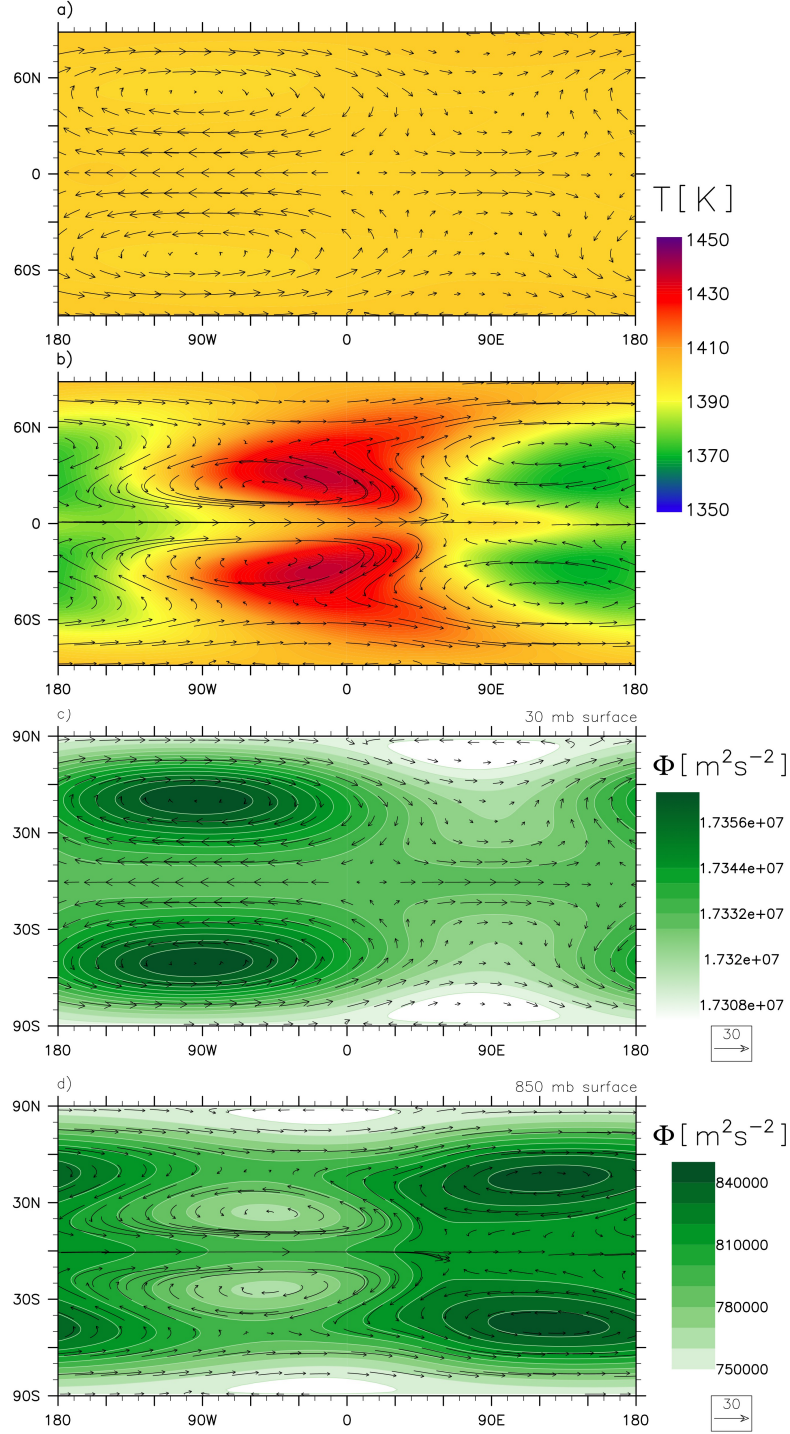


Figure 5.1: Snapshots from run F1b\* (small  $\Delta T_e = 50$  K, slow relaxation  $\tau_{\text{th}} = 3 \tau_p$ ), at  $t = 100 \tau_p$ . The upper panels show temperature (colour) and wind fields (arrows) at high ( $\eta = 0.24$ , panel a) and low ( $\eta = 0.83$ , panel b) altitude. The lower panels show geopotential (colour) and wind fields (arrows) at the 30 mb (c) and 850 mb (d) pressure surfaces. The substellar point is in the middle of each plot at  $0^\circ$  longitude and latitude.



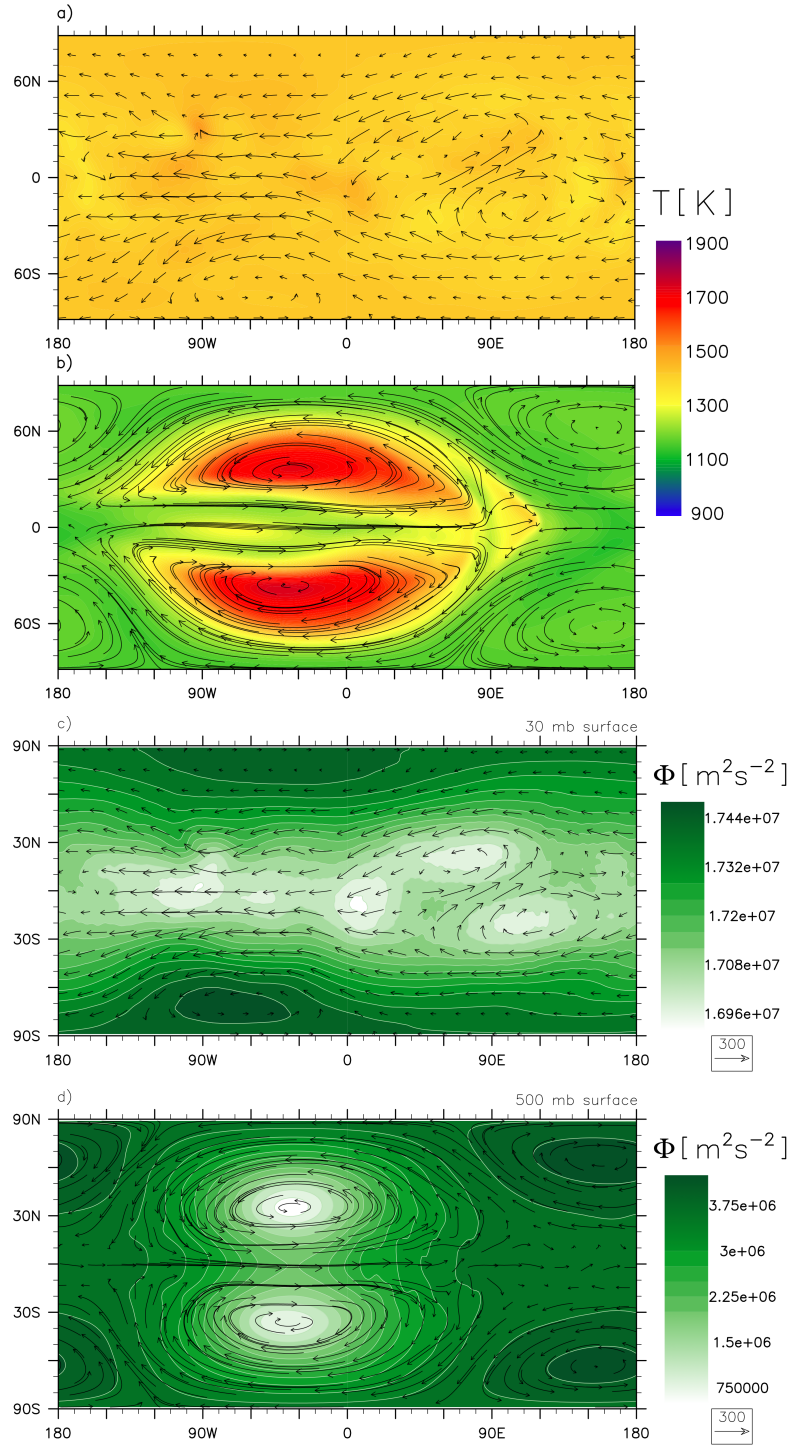


Figure 5.2: Snapshots from run F4b\* (large  $\Delta T_e = 500$  K, slow relaxation  $\tau_{\text{th}} = 3 \tau_p$ ), at  $t = 82 \tau_p$ . The upper panels show temperature (colour) and wind fields (arrows) at high ( $\eta = 0.24$ , panel a) and low ( $\eta = 0.83$ , panel b) altitude. The lower panels show geopotential (colour) and wind fields (arrows) at the 30 mb (c) and 500 mb (d) pressure surfaces.

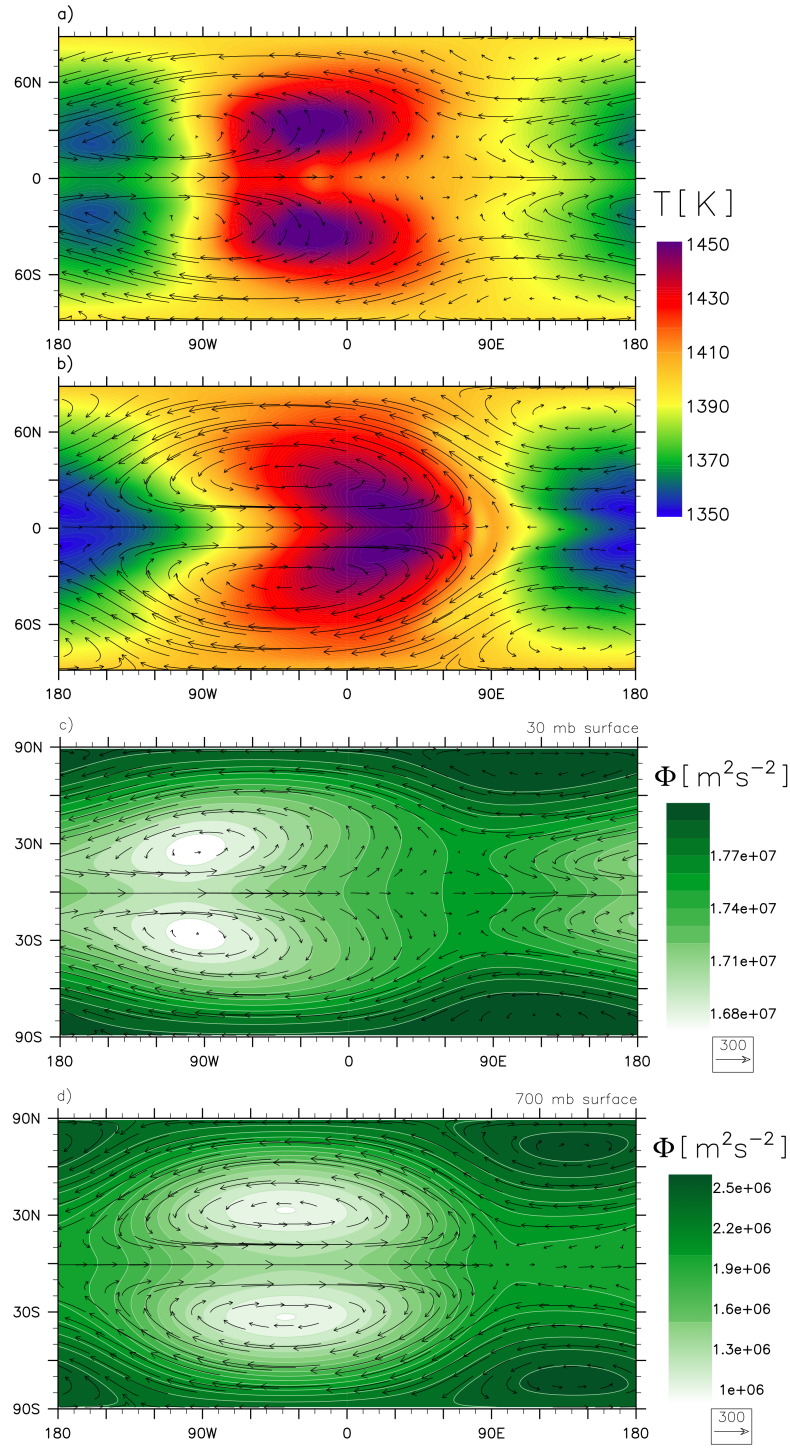


Figure 5.3: Snapshots from run F1d\* (small  $\Delta T_e = 50$  K, fast relaxation  $\tau_{\text{th}} = 0.1 \tau_p$ ), at  $t = 100 \tau_p$ . The upper panels show temperature (colour) and wind fields (arrows) at high ( $\eta = 0.24$ , panel a) and low ( $\eta = 0.83$ , panel b) altitude. The lower panels show geopotential (colour) and wind fields (arrows) at the 30 mb (c) and 700 mb (d) pressure surfaces.

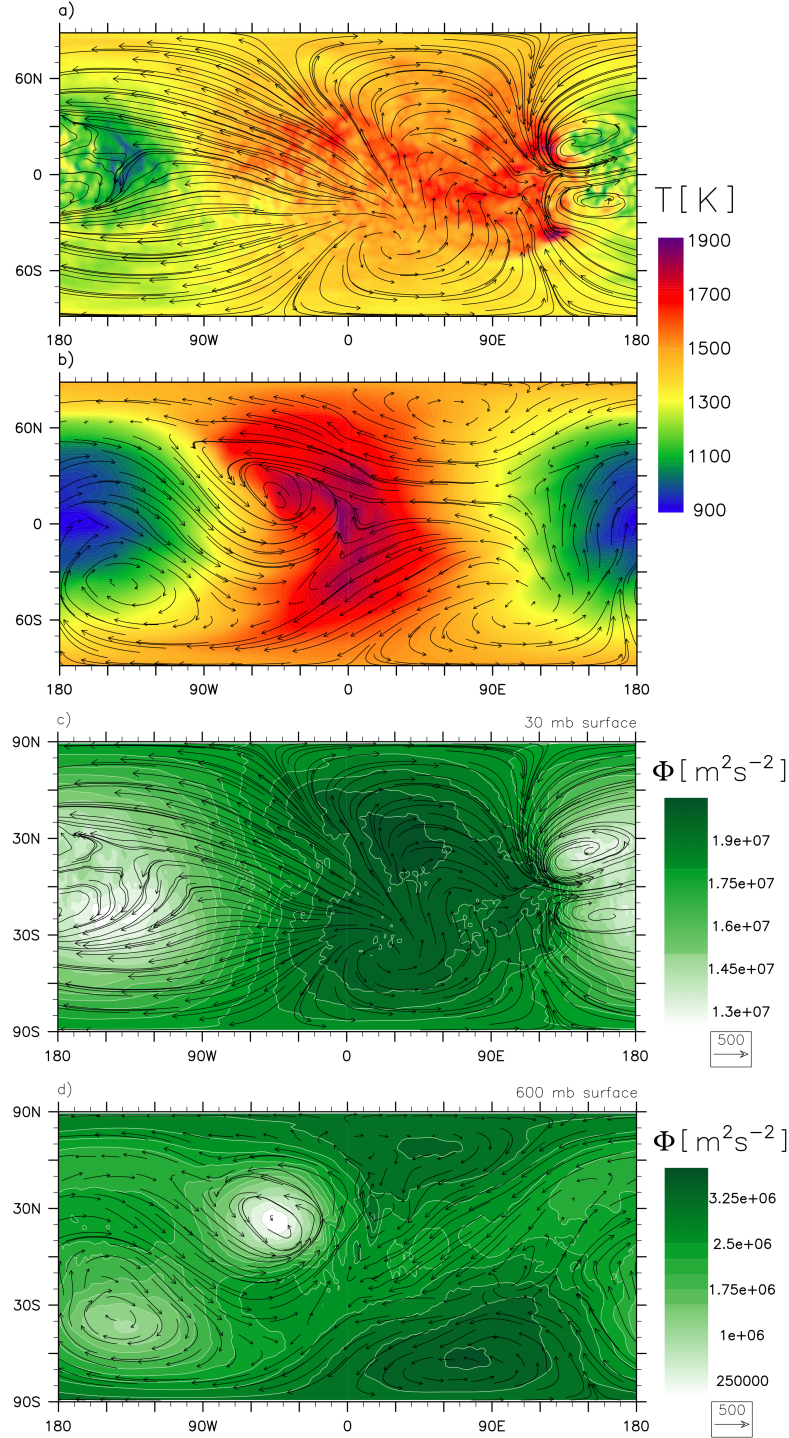


Figure 5.4: Snapshots from run F4d\* (large  $\Delta T_e = 500$  K, fast relaxation  $\tau_{\text{th}} = 3 \tau_p$ ), at  $t = 100 \tau_p$ . The upper panels show temperature (colour) and wind fields (arrows) at high ( $\eta = 0.24$ , panel a) and low ( $\eta = 0.83$ , panel b) altitude. The lower panels show geopotential (colour) and wind fields (arrows) at the 30 mb (c) and 600 mb (d) pressure surfaces.

(although there is a small tilt), As in run F4b\*, the mid- to high-latitude westward flow forms a wavy jet with one trough, and the wave pattern travels westward, as shown in Figure 5.7. But in this case the meridional amplitude of the wave does not change much during the cycle, which has a period of about 10-11 rotations. Here, as  $\tau_{th}$  is short, the temperature pattern does not follow the vortex columns as much as in run F4b\*, as they translate around the planet, but there is still a significant associated oscillation of the temperature pattern, especially at the higher altitudes.

In the limit of strong forcing (run F4d\*, large  $\Delta T_e = 500$  K, fast  $\tau_{th} = 0.1$  rots), an oscillatory state is quickly reached. Figure 5.4 shows a snapshot from this run. The flow is strongly asymmetric with respect to the equator, with an undulating eastward equatorial flow in the western hemisphere, that oscillates (the tilt of the streamlines fluctuating) with a period of about 2–3 rotations (see Figure 5.8). As the oscillations occur, cyclones are created in turn at one of the flanks, at the dayside front, which are then carried westward to the nightside, where they dissipate.

Figure 5.5 shows time series of meridional wind at a certain point in the atmosphere, for the first 1000  $\tau_p$  of runs F1b, F1d, F4b and F4d. These runs are the lower resolution equivalents of the four runs shown in Figures 5.1–5.4 and 5.6–5.8, and the higher resolution runs show the same behaviour for as long as they have been run (which is not as long as 1000  $\tau_p$  but at least 300  $\tau_p$ ). The chosen point is at mid latitude ( $\lambda \approx 45^\circ$ ),  $90^\circ$  west of the substellar point, at the level  $\eta = 0.83$ . At this point, the main characteristics of each of the different patterns of temporal behaviour discussed above are captured. The green curve displays the  $\sim 20$   $\tau_p$  period cycles of run F4b, where a planetary wave travels westward and undulates as it passes through the chosen point (as in Figure 5.6). The  $\sim 10$   $\tau_p$  period oscillation of run F1d, associated with the westward translation of a wave pattern and vortex columns (as shown in Figure 5.7), is manifested in the red curve. The blue curve shows the shorter ( $\sim 2$ – $3$   $\tau_p$ ) period oscillations of the equatorial eastward flow in the strongly forced run F4d (as in Figure 5.8). And finally, the flat black curve illustrates the stationary flow of the weakly forced simulation F1b.

The lower panels of Figures 5.1–5.4 show the geopotential field, and how it is aligned with respect to the flow, for the four different states dis-

cussed above. The panels show that in all the cases, geostrophic balance, where the Coriolis force and pressure gradient force are balanced (see Section 2.2), appears to be a reasonable approximation in large regions. Equations (2.12) which describe the geostrophic balance, can be recast in terms of the geopotential,  $\Phi$ , on constant pressure surfaces:

$$u = -\frac{1}{fR_p} \left( \frac{\partial \Phi}{\partial \phi} \right)_p \quad v = \frac{1}{fR_p \cos(\phi)} \left( \frac{\partial \Phi}{\partial \lambda} \right)_p \quad (5.5)$$

In almost all the frames shown, the wind blows along lines of constant geopotential, apart from the equatorial area. The flow is anticyclonic (clockwise in the northern hemisphere) around highs in geopotential, and cyclonic (anticlockwise in the northern hemisphere) around lows in geopotential, and thus consistent with geostrophic balance. This also holds at other times than shown here for the time variable states. At the equator, the geostrophic balance is expected to break down, since the Coriolis force goes to zero there. Apart from the equatorial regions, the main deviations from geostrophic balance, are in the upper parts of the run with the strongest forcing, F4d\*, where the winds are very strong.

For all the four states described above, the thermal forcing plays an active role, both in the development and maintenance of the states. Simulations were run, that were started from states similar to those shown in Figures 5.1–5.4, but with the thermal forcing turned off. In all cases, the atmosphere did not stay in the state it was in, but changed significantly. All of these runs seemed to evolve towards states with some common qualitative features. In all cases the zonal symmetry increased, and there was an eastward jet along the equator in the bottom part of the domain, with temperature increasing poleward, and a westward equatorial jet in the upper part of the domain. The negative vertical gradient of zonal wind and positive meridional gradient of temperature are consistent with thermal wind shear (see Equations 2.13).

Figure 5.9 shows snapshots at an early time in the evolution of run F4b\*,  $0.9 \tau_p$  after the simulation is started, both high up (top panel) and low down (bottom panel) in the domain. The simulation is started from an isothermal (1400 K) resting state, apart from small perturbations in the wind field. The initial response to the heating/cooling that is turned on at the initial moment, is that in the lower parts of the domain, the flow

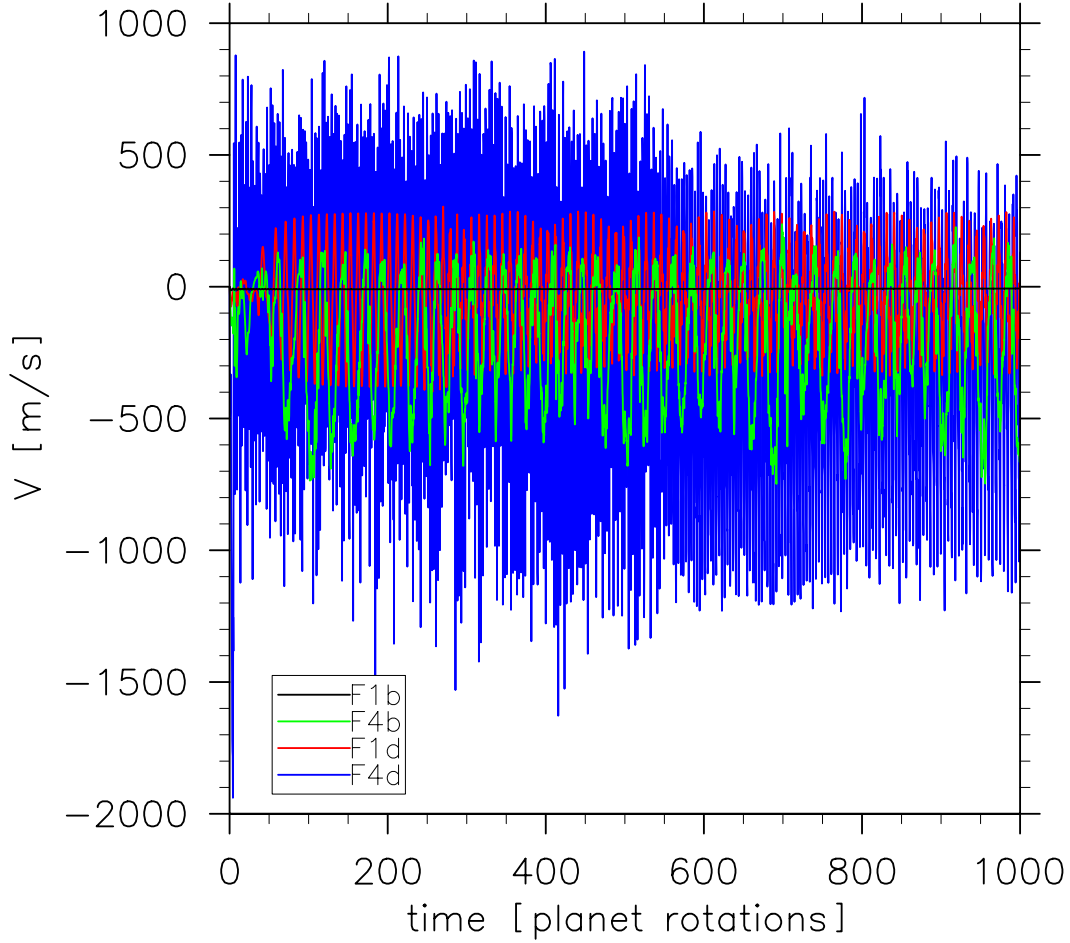


Figure 5.5: Time series of meridional wind at a certain point for four runs with a varied strength of forcing. The chosen point is at mid latitude ( $\lambda \approx 45^\circ$ ),  $90^\circ$  west of the substellar point, at the level  $\eta = 0.83$ , where the time series clearly show the different periodic oscillations that are characteristic of runs F1d (red line), F4b (green) and F4d (blue), and the stationary character of run F1b (black).



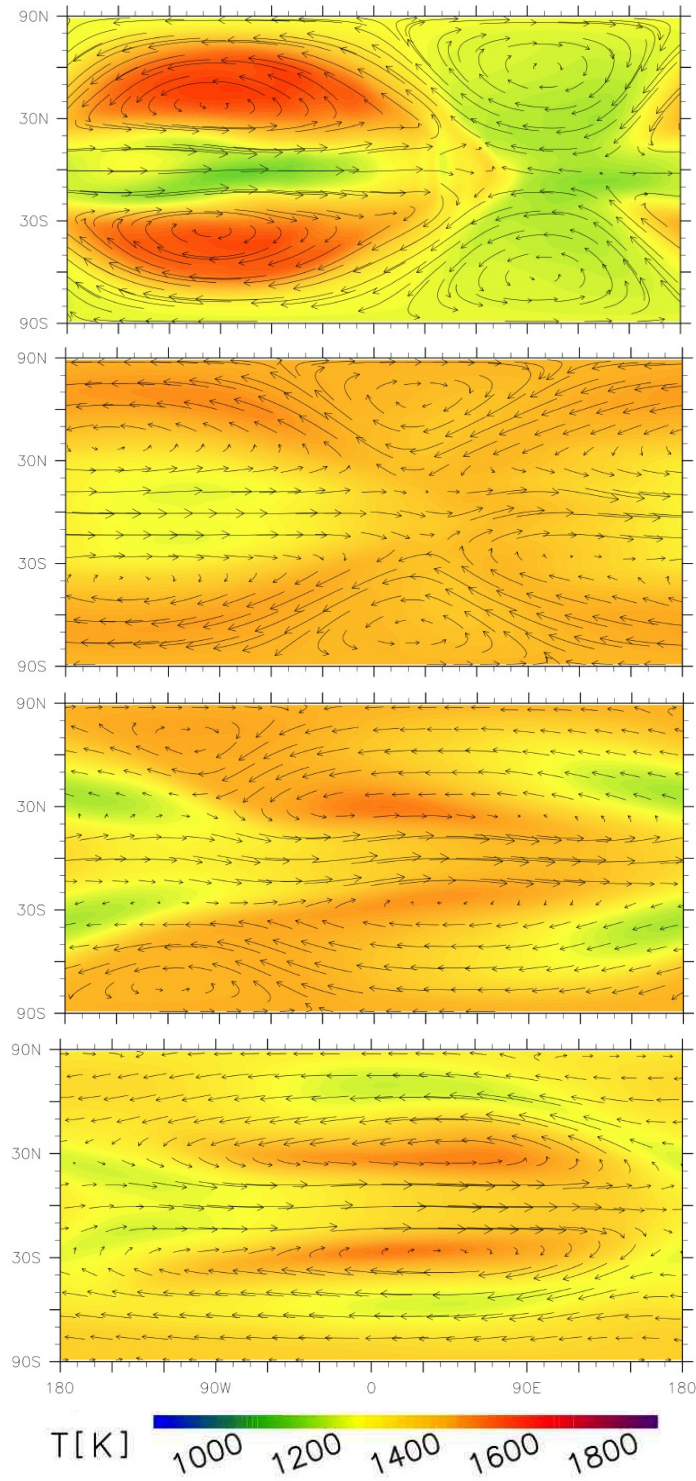


Figure 5.6: An oscillation cycle from run F4b\*. Each panel shows the temperature (colour) and flow (arrows) fields at a different time,  $t = \{89.1, 93.4, 96.0, 98.0\}\tau_p$ , with time increasing downward from panel to panel.

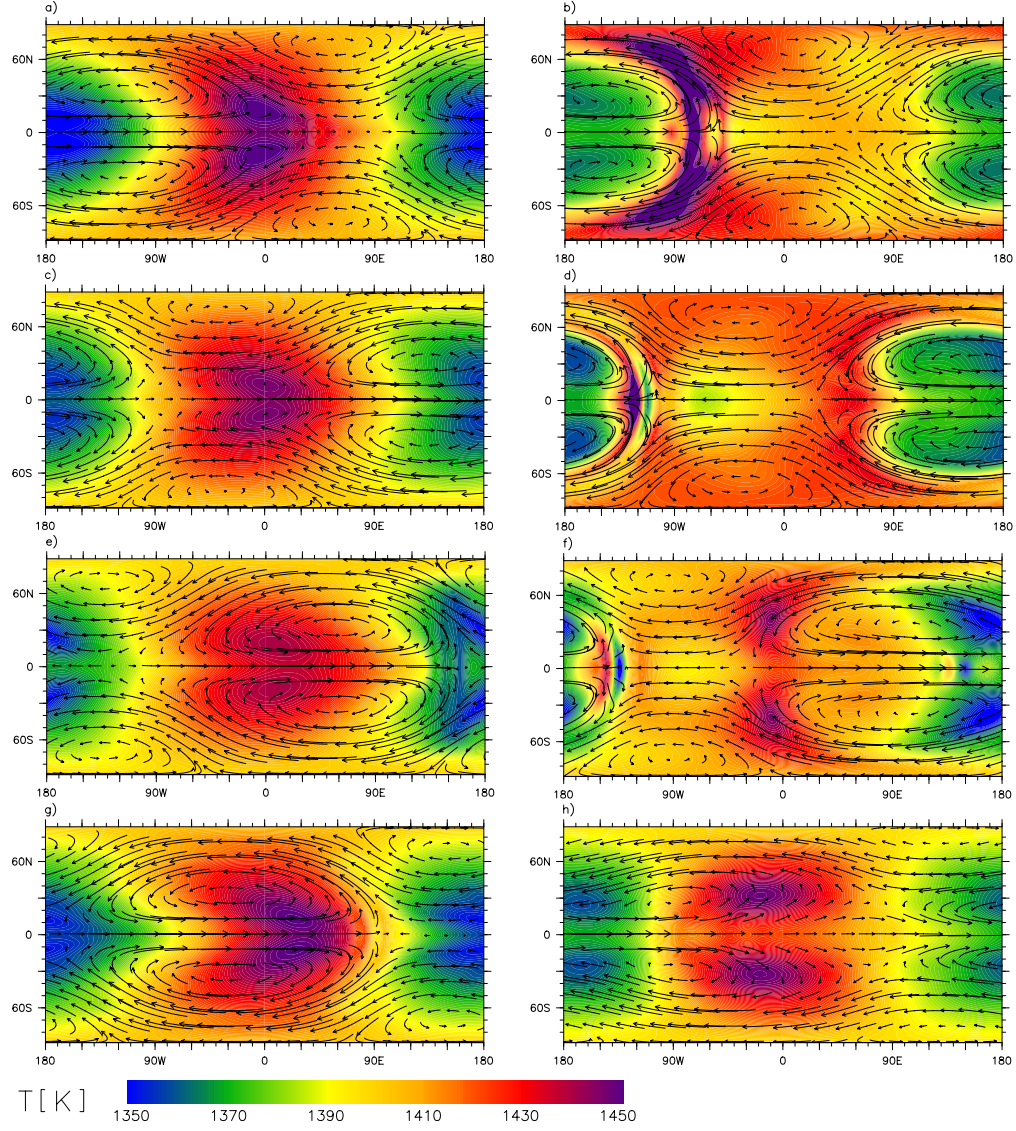


Figure 5.7: An oscillation cycle from run F1d\*. The temperature (colour) and flow (arrows) fields are shown at different times and heights. The panels show low (left column,  $\eta = 0.83$ ) and high (right column,  $\eta = 0.23$ ) altitude, at  $t = \{110.6, 113.1, 115.1, 117.7\} \tau_p$ , with time increasing downward from panel to panel.



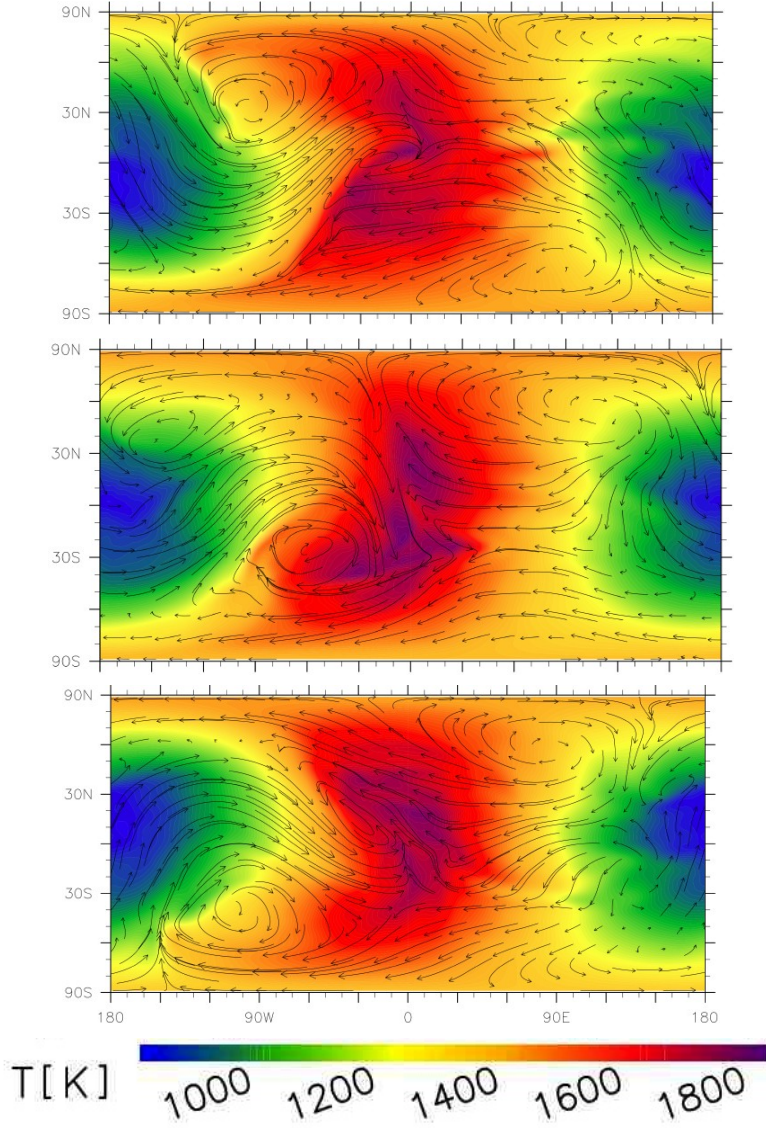


Figure 5.8: An oscillation cycle from run F4d\*. The temperature (colour) and flow (arrows) fields at the  $\eta = 0.83$  level are shown at different times. The panels show  $t = \{100.6, 101.1, 101.7\}\tau_p$ , with time increasing downward from panel to panel.

converges to a point close to where the heating peaks, where a low pressure (or low geopotential height) region is created, and there is a rising motion. On the antistellar hemisphere there is diverging, sinking motion in a high geopotential, cooled region. The rising motion on the dayside induces a mass source in the upper layers, and the flow and geopotential height quickly form a pattern that is qualitatively very similar to those discussed by *Matsuno* [1966] and *Gill* [1980] and in Section 5.2. It appears that the response to the heating here is similar, so that an eastward propagating Kelvin wave is launched, as well as a slower, westward propagating Rossby wave, with the flow and geopotential heights adjusting to near geostrophic balance. Thus, there is anticyclonic flow around the highs on each hemisphere, and cyclonic flow around the lows, very similar to Figure 9 of *Matsuno* [1966]. Lower down in the domain, lows are induced also at higher latitudes, with close to geostrophic cyclonic flow around them and anticyclonic flow around highs at higher latitudes on the night hemisphere (comparable to Figure 1 of *Gill* [1980]).

In this early phase described above, the atmosphere appears to be in the quasi-linear regime where a simple Matsuno-like model can apply, but here the strong linear drag that balances the steady-state solutions of *Matsuno* [1966] or *Gill* [1980] is not present, and non-linear interactions are not restricted, so the evolution quickly becomes more complex. After a few rotations, a pattern similar to that in Figure 5.2 has emerged, which subsequently reemerges periodically. The other runs F1b\*, F1d\* and F4d\* also show an initial response qualitatively similar to that shown in Figure 5.9, with Matsuno-like patterns emerging, but the subsequent evolution quickly diverges.

In simulations where the  $(\tau_{\text{th}}, \Delta T_e)$  parameter space is further explored, as well as when the long term behaviour in the simulations is inspected, long-lasting states of similar qualitative character to those described above are observed. Thus, a run with intermediate relaxation time ( $\tau_{\text{th}} = 0.5 \tau_p$ ) but large  $\Delta T_e = 500$  K (run F4cI), goes through a stage similar to the short-period oscillatory state of run F4d\*, before transitioning to a state more similar to run F4b\* with a longer period longitudinal translation and pulsation or “breathing” of vortex columns. A further transition is observed at extremely long times which is described in Section 5.4.2. A run

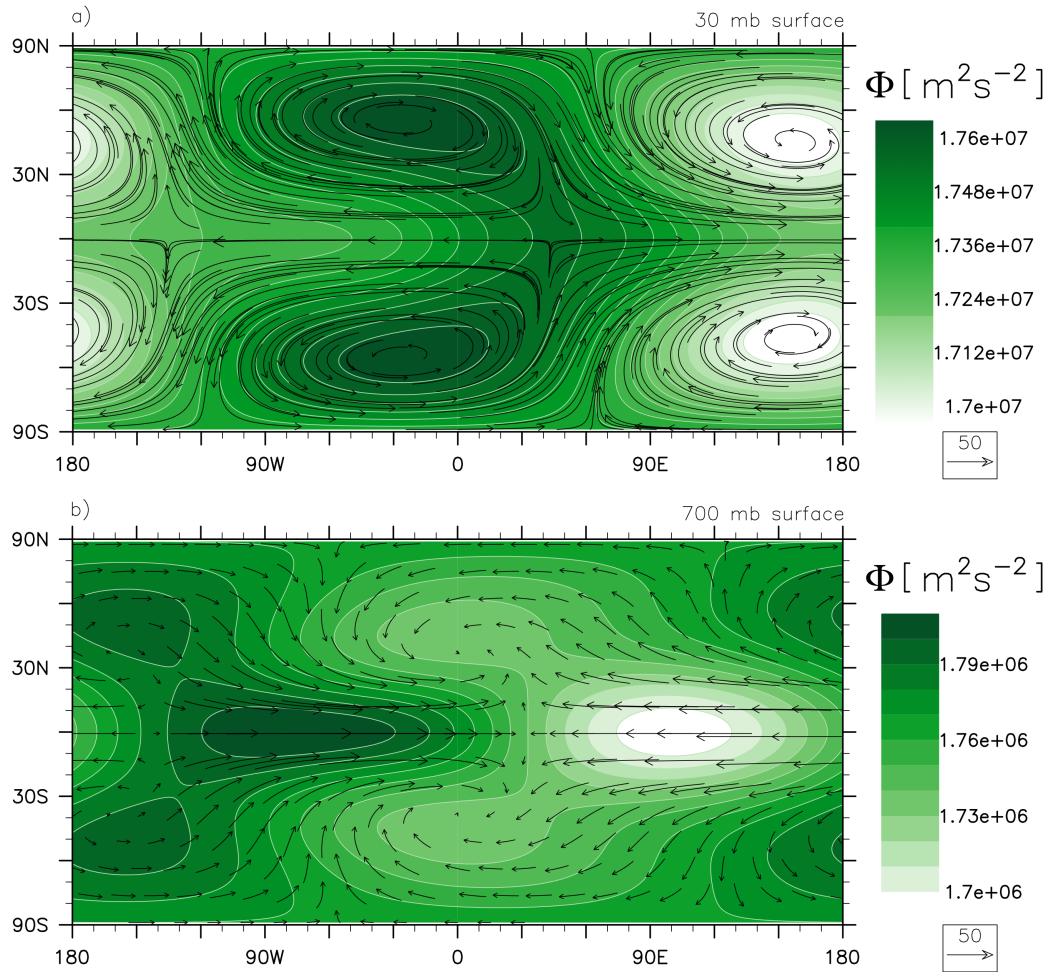


Figure 5.9: Early response in run F4b\*. Geopotential (colour) and wind fields (arrows) are shown at the 30 mb (top) and 700 mb (bottom) pressure surfaces, at an early time,  $t = 0.9 \tau_p$ .

with intermediate relaxation time ( $\tau_{\text{th}} = 0.5 \tau_p$ ) but small  $\Delta T_e = 50$  K (run F1c), appears to go through stages that resemble both the states shown for runs F1b\* and F4b\*.

In the case of intermediate  $\Delta T_e = 100$  K, the run with short  $\tau_{\text{th}} = 0.1 \tau_p$  (run F2d) exhibits behaviour similar to run F4d\*, and later a combination of the states of runs F1d\* and F4b\*. In run F1d\*, after a few hundred rotations, the north/south symmetry is broken and the equatorial jet starts to oscillate in a manner similar to the short period oscillation of run F4d\*. This meridional oscillation is then superimposed on the longer period zonal translation.

### 5.4.2 Transitions During Long Term Evolution

Different quasi-equilibrated states, that are reached for different initial conditions for a given forcing, are described in Chapter 3. In a further exploration, two simulations which only differed in the initial flow were run for extremely long times; more than 80,000 rotations. Both simulations exhibit ‘quasi-stable’ stationary or oscillatory states that are persistent for long periods, and can be distinguished into different stages – both within a given simulation and between them.

Figure 5.10 shows the kinetic energy evolution in these runs for various epochs. Focusing on the early evolution, the first 100 rotations shown in Figure 5.10a, run F4cI (black line) goes through an initial transient period which seems to level off at about  $30\text{--}40 \tau_p$ . After that the kinetic energy oscillates about a seemingly stable value, with a period of about  $7 \tau_p$ . Run F4cII (red line) also goes through an early transient period, but the kinetic energy seems to level off at roughly  $10 \tau_p$ , with  $\sim 4\tau_p$  period oscillations.

Frame b is focused on the first 1500 rotations. In run F4cI, larger oscillations start to appear around  $450 \tau_p$ , which get ever more frequent and regular, while there is a slow overall trend upwards. In contrast, the behaviour of run F4cII seems not to change much over this whole period. Zooming further out to the first 6000 rotations (Figure 5.10c), the upward tendency of run F4cI increases until at  $\sim 4000\text{--}5000 \tau_p$  the growth starts to slow down. The large oscillations quite suddenly shrink around

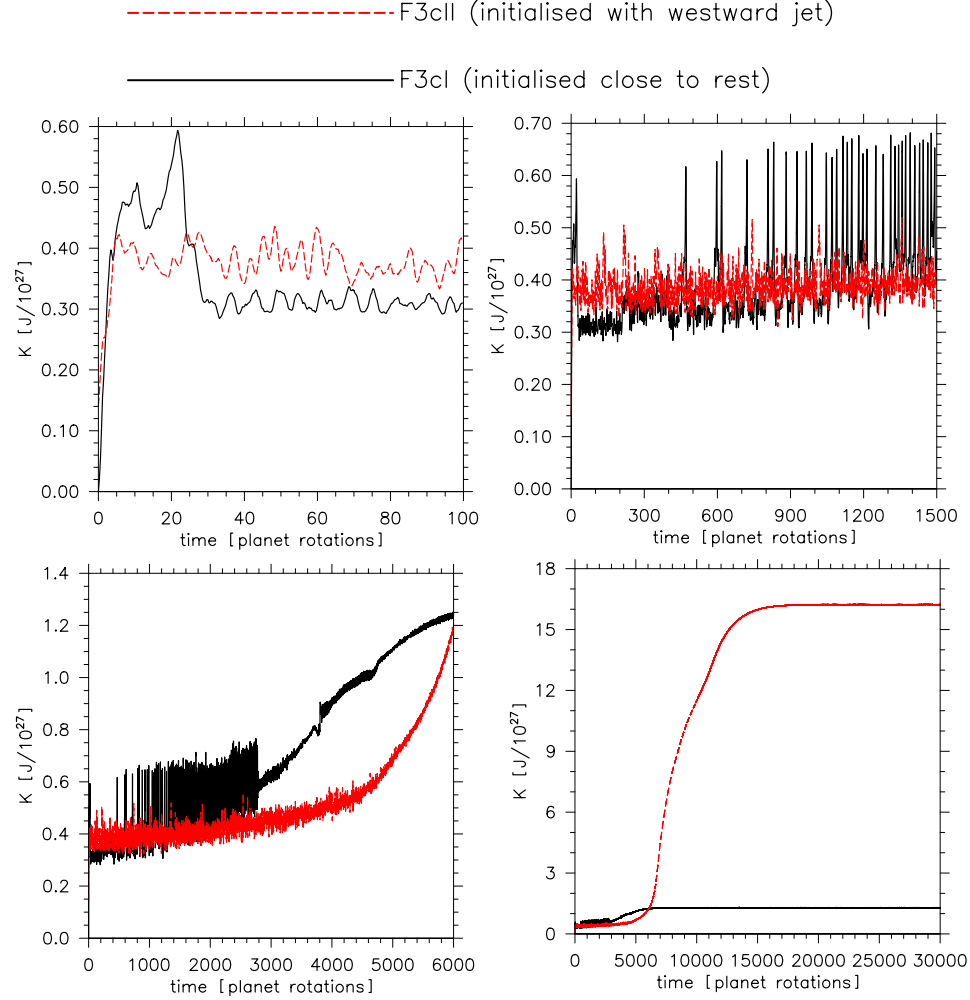


Figure 5.10: Total kinetic energy evolution of two runs that are identical apart from the initial condition. The four frames zoom in on different epochs. The black curve is for run F4cI, initialised with a small amount of noise, and the red curve is for run F4cII, started with a westward jet. After reaching the stage where both curves are flat, the total kinetic energy did not change for even longer than the last panel shows, and was still at the same value after more than 80000 planet rotations, when the simulation was stopped.

2800  $\tau_p$ . During this epoch, run F4cII exhibits an upward trend in the kinetic energy, which starts slowly but seems to grow exponentially, while the oscillations gradually decrease. As shown in frame d, this growth only starts slowing down at  $\sim 7000 \tau_p$ , and continues until  $\sim 18000 \tau_p$ . From then on, the global kinetic energy is stable for the whole duration of the simulation, more than 80000  $\tau_p$ . The curve for run F4cI levels off earlier, at  $\sim 7000 \tau_p$ , and stays flat past 80000  $\tau_p$ , until the end of the simulation.

Figure 5.11 shows the temperature and wind fields at four points in time for run F4cI. The different frames show snapshots at a low (left column) and high (right column) altitude, that are characteristic for the various stages of evolution that the atmosphere goes through during the simulation, and can be connected with the kinetic energy evolution described above.

The top row frames show the temperature and winds at  $t = 40 \tau_p$ , but the oscillatory, baroclinic state that has been reached, is characteristic of the first  $\sim 500 \tau_p$ . This state bears a qualitative resemblance to the state of F4d\* (see Figure 5.4), with the undulating eastward equatorial flow at the lower levels undergoing short ( $\sim 2 \tau_p$ ) period fluctuations, and the cyclones cyclically moving, dissipating and reforming.

The second row shows snapshots at  $t = 2700 \tau_p$ . At this point, the flow goes through longer period cycles more reminiscent of the state of F1d\* (see Figure 5.3), where the cyclones translate all around the planet, elongating and reforming periodically. These cycles correspond to the large spikes in the global kinetic energy evolution curve, that start to occur at  $t \sim 500 \tau_p$ , until shortly after this snapshot when the oscillations shrink. The row below shows the state after the kinetic energy oscillations have shrunk ( $t = 2900 \tau_p$ ). The eastward equatorial flow has now reached all around the planet at low altitudes, forming a wave with two troughs that propagates westward with a period of roughly 12–15  $\tau_p$ . During the period when the global kinetic energy is growing, the jet gradually spreads from the bottom up, until the flow and temperature are well aligned vertically throughout the domain. This is shown in the bottom row of Figure 5.3, which is taken at  $t = 20000 \tau_p$ .

If the forcing is turned off well after the kinetic energy has levelled off (at 20000  $\tau_p$ ), the wavy eastward jet straightens out, and the temperature



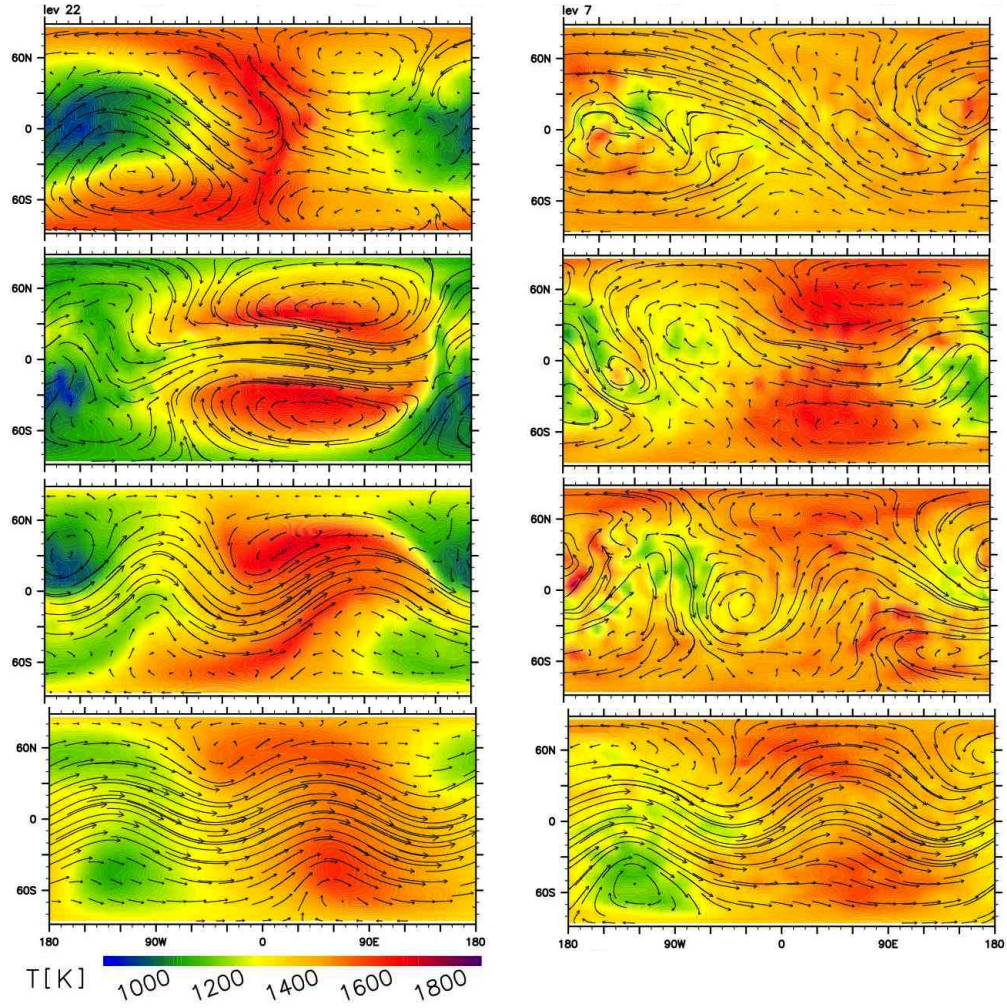


Figure 5.11: Snapshots of temperature (colour) and flow (arrows) fields at various stages of run F4cI. The panels show low (left column,  $\eta = 0.83$ ) and high (right column,  $\eta = 0.23$ ) altitude, at  $t = \{40, 2700, 2900, 20000\}\tau_p$ , with time increasing downward.

structure is adjusted according to thermal wind shear (see Equations 2.13). Thus temperature decreases poleward below where the speed of the jet peaks (where  $\partial u/\partial z > 0$ ), and increases poleward above the peak (where  $\partial u/\partial z < 0$ ).

Figure 5.12 shows the temperature and flow fields at various points in time for run F4cII, which was initialised with a westward equatorial jet. The left column shows low altitude ( $p \sim 850$  mb) and the right column high altitude ( $p \sim 100$  mb), and different rows show different times, with the time increasing downward. Figure 5.13 shows the strength of the zonal wind field for the same frames as in the right column of Figure 5.12.

The frames in the top row of Figure 5.12 are from  $t = 40\tau_p$ . At this point the atmosphere has reached an oscillatory baroclinic state, which can be compared with the state of F4d\* (Figure 5.4). Offset polar anticyclonic vortex columns, are present throughout the domain, tilted with height. At low altitudes, there are warm cyclone columns to the west of the substellar point, whereas at high altitudes, there is a cyclone column pair to the east. This state persists for thousands of  $\tau_p$ , with oscillations that correspond to the kinetic energy oscillations in Figure 5.10. The oscillations occur as the lower cyclones move, split and merge, and the horizontal tilt of the eastward flow between them periodically fluctuates, at the same time as the anticyclonic vortex columns revolve around a point just offset from the pole. The maxima of the global kinetic energy oscillations occur when the anticyclones are furthest from the pole and the flow between them (at lower latitudes) is ‘squeezed’ and accelerated. At  $t = 2700\tau_p$  (the second row of Figure 5.12), the above qualitative description still applies, although there are quantitative differences.

However, at  $t = 5000\tau_p$  (middle row), the lower cyclone pair has disappeared, and the flow is purely westward at the lower levels. The disappearance of the lower cyclone columns is gradual, and concurrent with the strong rise in the global kinetic energy. Once the lower cyclones are gone, the offset polar vortex columns stabilise and the global kinetic energy oscillations decrease. The broad westward jet gradually extends upward and the higher cyclone columns are pushed toward the top, becoming stronger but shallower, until the westward jet dominates throughout, as seen in the fourth row from the top in Figure 5.12 where the cyclones are gone at the



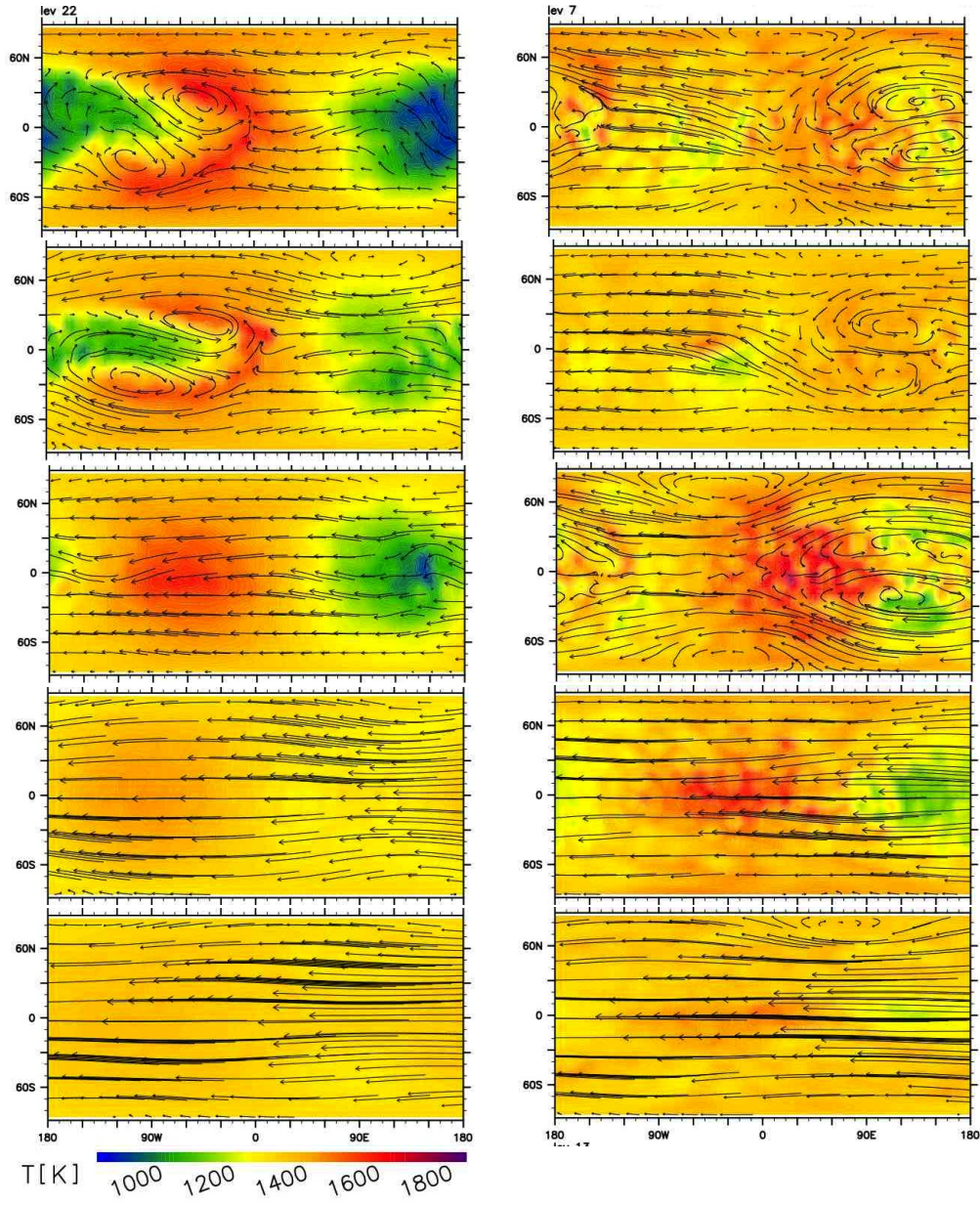


Figure 5.12: Snapshots of temperature (colour) and flow (arrows) fields at various stages of run F4cII. The panels show low (left column,  $\eta = 0.83$ ) and high (right column,  $\eta = 0.23$ ) altitude, at  $t = \{40, 2700, 5000, 7000, 20000\}\tau_p$ , with time increasing downward.

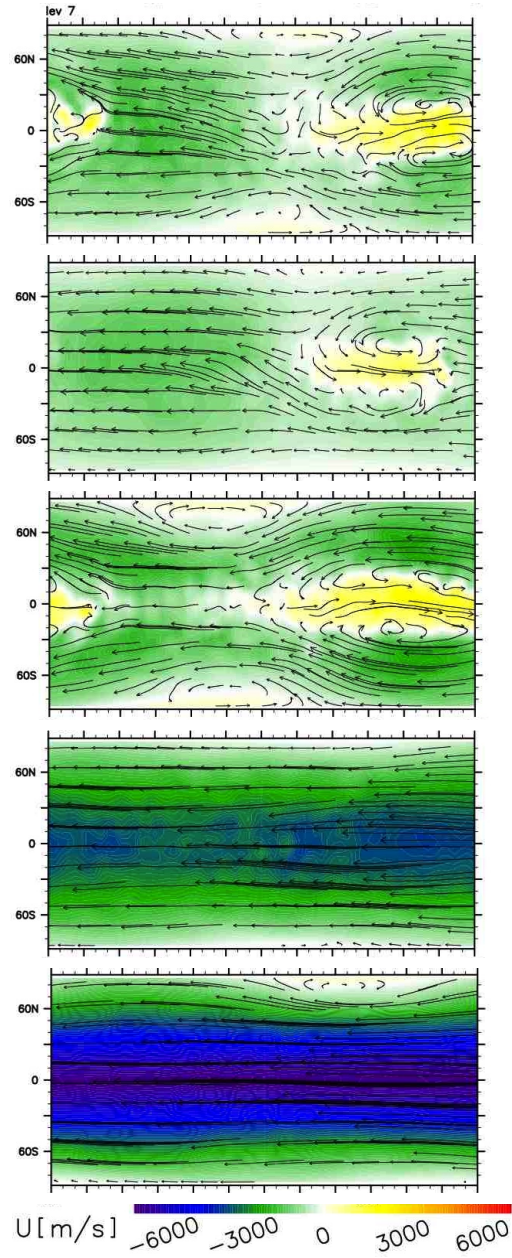


Figure 5.13: Snapshots of zonal wind (colour) and horizontal flow (arrows) fields at various stages of run F4cII. The panels all show the fields at  $\eta = 0.23$ , at  $t = \{40, 2700, 5000, 7000, 20000\} \tau_p$ , with time increasing downward.

shown levels. As the eddies are no longer ‘in the way’ the westward zonal flow speed increases drastically, as shown in Figure 5.13, up to  $\sim 7000$  m/s. The state shown in the bottom row of Figure 5.12, where the temperature field has been almost completely homogenised, is almost barotropic, although the polar vortex column does have a tilt. This state is stationary and persists till the end of the simulation. In contrast to the other runs described above, turning off the thermal forcing has little effect on this state.

It is clear from all the simulations discussed above, that the zonally asymmetric heating applied, tends to produce large-scale eddies or vortices, that persist for long time scales. When the forcing is turned off, the flow usually tends towards zonal symmetry. In run F4cI eddies are still present until the end of the run, and in F4cII where the flow eventually becomes almost zonally symmetric and speeds up, it is clearly associated with the gradual disappearance of the eddies.

The extremely fast flow speed reached at the end is well in the “transonic” regime (Mach number  $\sim 2.5$ )<sup>1</sup>, which raises serious concerns whether this interesting evolution has numerical, rather than physical causes, at the extremely long times. Furthermore, small scale oscillations are quite prominent at times in this strongly forced simulation, and numerical errors have had a long time to build up.

To put the time scales into context, the advection time for a 1000 m/s flow to reach around the planet is  $\tau_{adv} \sim 2\tau_p$ , so the different stages of evolution for the two runs F4cI and F4cII persist for times that are roughly two orders of magnitude longer than the advection or thermal relaxation time scales, and the final stages for at least four orders of magnitude longer.

### 5.4.3 Storms and Variability

The presence and large size of vortices, or storms, in most of the simulations discussed above, induces the question what their potential consequences might be for present and future observations. Figure 5.14 shows different phases of an evolution cycle of the cyclonic storms in run F4d\*.

<sup>1</sup>Here we refer to the sound speed that would be associated with the temperature in the actual atmosphere ( $c_s = (\gamma RT)^{1/2}$ ), whereas in the primitive equations model atmosphere the sound speed would go to infinity as sound waves are filtered out.

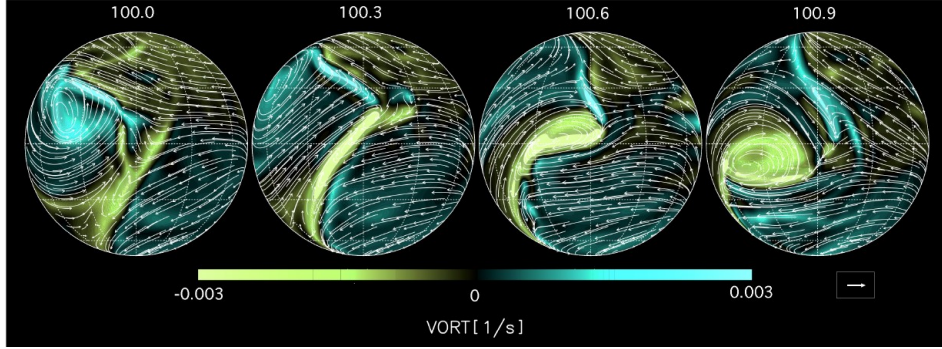


Figure 5.14: Results from run F4d\*, at four successive times (100.0, 100.3, 100.6 and 100.9 planet rotations). The plots are centered at the substellar point, with the color scale showing vorticity. The flow is highly variable in time, with large scale vortices, or storms, moving and changing in cyclic fashion.

The figure shows the vorticity field at four successive points in time (see also Figure 5.8 for the temperature variations in a cycle of the same run). The storms form near the substellar point through folding of fronts about every couple of days for many hundreds of planet rotations. In the simulation shown, the storms form alternatively in the northern and southern hemispheres, move off to the night side, where they are dissipated; then, a new storm forms on the day side. From careful analysis of movies from the simulations the storms are observed to be responsible for advecting and mixing heat across the day-night hemispheres, which are broadly hot-cold when thermal relaxation times are short.

In cases where the relaxation time is longer, different cycles of storms moving across the face of the planet, can cause even greater effects on the temperature field, as can be seen in e.g., Figure 5.6 (from run F4b\*, where  $\tau_{\text{th}} = 3\tau_p$ ), or Figure 5.11 (from run F4cI, where  $\tau_{\text{th}} = 0.5\tau_p$ ). From the simulations the power spectrum of the temperature field can be obtained. Figure 5.15 shows a power spectrum of temperature at selected points on the planet for run F4cI, taken over the period between 500 and 2500  $\tau_p$ . In principle, this kind of plot can provide ‘variability periods’ which can allow observers to plan their observing runs. The power spectrum shows that the bulk of the energy is contained in slow ( $\sim 15$ -day) oscillations, which are planetary in scale; observe that the spectrum on the antipodes of the planet (substellar and antistellar points) nearly coincide – partic-



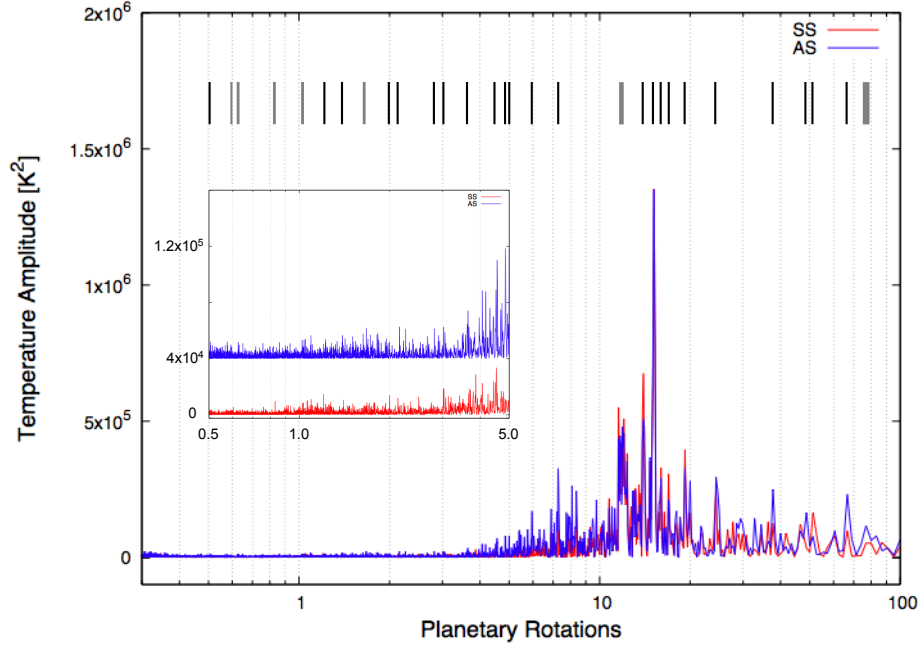


Figure 5.15: Power spectrum of temperature time series for a CEGP simulation. The red line shows the temperature at the substellar point and the blue line at the antistellar point. Both show temporal variability of various periods, but clearly identifiable dominant components.

ularly for periods greater than 3 or 4 planetary rotations. The inset is a zoom of the short period region. The set of lines at the top of the figure shows the strong peaks in the spectrum; the variability is ‘rich’, with many identifiable peaks. The most dominant periods can be associated with specific processes (such as the cycles described in Section 5.4.1) by careful analysis of the simulations. Variability of this type and scale will affect disk-integrated flux and could be detectable by observing multiple transits of the same planet, even without having spatial resolution or composition constraints for the atmosphere. This can help guide/design proposed missions, such as *Thesis/EChO* and *JWST*, and gives a glimpse of how a combination of observations and modelling could provide insights into mechanisms at play in the atmospheres.

Another example of the time variability can be seen in Figure 5.6 from run F4b\*. In the top frame, the cyclones act as hot spots when they are

on the dayside, keeping fluid confined where it can keep warm. But as the cyclones move away to the nightside and weaken, the westward jet bulges down to the substellar point and distributes hot fluid to the night side more quickly, resulting in a more even temperature field. The period of the oscillations here is about  $15\text{--}20 \tau_p$ .

The vortices in the simulations discussed above can be either transient or long-lasting. In addition to the different temperature, markedly different chemistry, clouds and aerosols could exist inside the long-lasting vortices, although that is not modelled here. On the other hand, vigorous and efficient mixing can take place through the transient vortices and outside the vortices.

Further explorations of the parameter space, e.g. with different vertical structure of the forcing, forcing in a narrow region, with a different functional shape of the relaxation temperature profile, or different vertical domain sizes, have given further implications of the important role of large scale vortices and time variability.

## 5.5 Conclusion

In this chapter it has been shown that for a different strength of thermal forcing, varied through  $\tau_{th}$  and  $\Delta T_e$ , idealised CEGP simulations exhibit multiple states, which are qualitatively different. The states are either stationary or oscillating, but equilibrated in the statistical sense over at least several hundred  $\tau_p$ . The oscillatory states are characterised by planetary scale waves and large scale vortices pulsating (elongating and reforming) and/or translating around the planet with long ( $\sim 10\text{--}20 \tau_p$ ) periods, or by shorter ( $\sim 2\text{--}3 \tau_p$ ) period equatorial oscillations, with corresponding storm cycles, or by a combination of these types of oscillations. Separate statistical or stationary equilibria can be reached for a given forcing, through varying initial conditions. But also, transitions between distinguishable long lasting states are exhibited during the long term (tens of thousands of planet rotations) evolution of individual simulations.

The long term evolution can lead to broad jets, either wavy or straight, eastward or westward. But in all the simulations, large eddies characterise the early evolution, and in most cases the appearance of large vor-

tices persists for long (hundreds of  $\tau_p$ ) time scales. While these studies are idealised, temporal variability of the kind described here, associated with the large scale waves and vortices, can have implications for observational studies. The flow variability is intimately linked with temperature fluctuations and transport of heat from warm to cold regions. Since temperature crucially affects observed flux and spectra, such variability can cause discrepancies between measurements taken at different epochs. But this also presents an opportunity to measure potential periodicities and link them with physical processes and mechanisms, by making repeated measurements of a given planet. For example, the correspondency between the substellar and antistellar point periodicities, discussed in Section 5.4.3, would suggest a causal connection between the opposite sides of the planet, that could be an implication of planetary scale waves.

The thermal forcing leads to large eddy/wave responses in all the cases considered. In a more realistic scenario the forcing is dependent on space and time, through e.g., distributions of radiatively active species, and the dependence of opacities on density and temperature, etc. When the forcing is turned off in the simulations, the atmosphere usually goes to a different state. This suggests that for more variable forcing, time variability will be even more pronounced.

The results of this exploration lead to several ways to move forward in understanding atmospheric dynamics of synchronously rotating extra-solar giant planets. Matsuno-Gill type models for the response to zonally asymmetric forcing are relevant, but at very early times. However, interaction with a background flow needs to be taken into account in more extended studies. Over a wide range of parameter space, large regions in the domains of the simulations, are seemingly consistent with geostrophic balance. Thus, simple quasi-geostrophic analysis can be useful. Most of the long lasting states observed in the simulations, are characterised by low order modes, in the zonal, meridional and vertical directions. This suggests that highly truncated spectral analytical methods can be relevant to study these states. Stability studies of simple, idealised states, akin to Charney & DeVore (1980) appear a promising route to take, to gain further understanding of dominant features and processes in the simulations.

However, small scale waves and processes may have an important role.

They would not be captured in this type of study, and they may be artificially suppressed by the way the simulations that have been described here are set up. The distinct states that have been identified in the preceding sections could be useful as initial conditions in high resolution studies, where the fluid is not as suddenly exposed to sharp forcing gradients and less artificial damping is needed to stabilise the simulations. This might allow smaller scale effects and their interaction with the larger scales to be addressed more realistically.



# Chapter 6

## Conclusion

The atmospheric circulation of extrasolar giant planets on synchronous orbits has been the focus of this thesis. The expected hot temperatures, fixed day/night thermal forcing and relatively slow rotation rates ( $\sim 50$ – $100$  h periods), place these planets in a parameter regime which is only beginning to be explored. Furthermore, thus far only limited constraints are available from observational studies to constrain the model parameters. However, the tight link between dynamics, temperature distributions and observed signals makes the understanding of the dynamics crucial. Given the rapid improvements in the measurement techniques, there is a great opportunity and challenge for observers and theorists to work together to find ways to extend current knowledge of atmospheric dynamics and learn about the conditions, physical processes and mechanisms that prevail on these planets.

### 6.1 Summary

In this thesis a numerical General Circulation Model (GCM) has been used to study Close-in Extrasolar Giant Planet (CEGP) atmospheres. This type of model has been successful in studies of the Earth and other Solar System planets, but it requires a number of poorly constrained parameters for CEGPs, and its use has many pitfalls. The limited observational constraints and the limited currently available experience of modelling CEGP atmospheres, call for a careful approach to their modelling. The overall approach taken here, has been to i) strive for minimal complexity and

reliance on unknown constraints, ii) set up idealised scenarios, iii) do a thorough and systematic exploration of the relevant parameter space, and iv) identify robust features and important sensitivities.

In the relatively unexplored area of CEGP atmospheric modelling, it is especially important to ask whether the results of numerical simulations are actually physical or whether they are contaminated or caused by numerical artefacts, in which case they should be discarded. The expected realm of CEGP atmospheres is extreme in some sense, as the thermal forcing may be strong and temperature contrasts can be large. In attempting to model this, GCMs can easily be stretched to or even beyond their limits.

In Chapter 4 I focused on some crucial aspects for numerical modelling of CEGPs, which had not been given much attention before in the extrasolar planet literature. I demonstrated the importance of effects of artificial viscosity, which is necessary to control unphysical small-scale oscillations. In particular, I concentrated on the relation between the artificial viscosity and thermal forcing within the context of Newtonian thermal relaxation. In many numerical studies of CEGP atmospheric dynamics [e.g., *Showman et al.*, 2008a; *Rauscher and Menou*, 2010], a large range of thermal relaxation times ( $\sim 10$  days to  $\sim 1$  hour) is used within a given simulation. In Chapter 4 it was demonstrated that a short relaxation time (much less than the planetary rotation time) leads to a large amount of noise, unless an excessive amount of artificial viscosity is used. This effect is more pronounced when the gradients in the equilibrium temperature profiles are large. The implication is that simulations with a large range of relaxation times, including very short ones, will be either under-dissipated (noisy) or over-dissipated (sluggish and spread out), or both, if a single value is used for the strength of artificial viscosity.

The analysis of kinetic energy spectra, in combination with vorticity fields, was used to show how the “optimal” artificial viscosity can be chosen, and when simulation results should be discarded. Large equilibrium temperature gradients combined with fast relaxation time scales represent a violent forcing, especially when the flow is initialised far from a balanced state, and *this should be avoided*. This applies to more complex representations of radiative heating/cooling as well. Simulations using a narrow range of relaxation times can still be useful, as long as they are

combined with parameter sensitivity studies. But if the short  $\tau_{\text{th}}$  really are physically relevant, then alternative ways of representing the forcing, such as using adiabatic, steady forcing, seem more appropriate, as the radiative processes appear as practically instantaneous anyway. In any case, an improved setup for modelling of strongly forced atmospheres should involve a gradual ramping up of the heating and/or initialising simulations close to a balanced state.

In Chapter 3, the sensitivity of the evolution of flow and temperature to the initial flow state was investigated for conditions relevant to CEGP atmospheres. It was shown that the flow and temperature distributions depend strongly on the initial state. Simulations initialised with a different jet configuration, but all other parameters identical, settle into different quasi-equilibrated states. In all cases the flow is characterised by a small number of large scale vortices ( $\sim 4$ ) and jets ( $\sim 1-3$ ). But the directions of the jets vary between the simulations, and the locations and temporal behaviour of the vortices, as well as the associated temperature distribution, exhibit distinctly different character.

The sensitivity is present if time averages are taken over long periods of time (hundreds of  $\tau_p$ ), and for a large range in parameters such as the relaxation time. This result is in contrast with the results or assumptions of many published studies, and underlines the fact that circulation models are currently unsuitable for quantitative predictions (e.g., location and size of a “hot spot”) without better constrained, and well-posed, initial conditions. More broadly, it also highlights the importance of testing different initial conditions to verify robust features and mechanisms, and shows the relevance of studying interactions with a variety of background flow states.

The behaviour described above suggests that multiple quasi-equilibrated states can be reached for a given forcing condition, relevant to CEGPs. The study of the multiple equilibria was addressed more thoroughly in Chapter 5, where this behaviour was studied in extremely long time (more than 80,000  $\tau_p$ ) integrations. During the long term evolution, transitions between different long lasting states were observed and characterised. Furthermore, distinct stationary or oscillatory states were reached for variations of the thermal forcing strength. In all of the simulations, large scale

vortices are formed, which are dominant features of the flow, and persist during most of the long-lasting states. Some of the oscillatory states are characterised by planetary scale waves and large scale vortices, which pulsate (elongate and reform) and/or translate around the planet with long ( $\sim 10\text{--}20 \tau_p$ ) periods. The other oscillating states exhibit shorter ( $\sim 2\text{--}4 \tau_p$ ) period equatorial oscillations, with corresponding storm cycles, or a combination of these types of oscillations. The variability due to motions of planetary waves and vortices, is accompanied by an associated periodic variability in the temperature field.

These idealised calculations are not intended or expected to give an accurate match to the actual state of the atmosphere of a particular planet, but they can suggest plausible features that are relevant for observations. Thus, the common presence of large scale storms and their associated variability can suggest time scales relevant for future observational studies, and provides a strong argument in support of repeated observations of a given planet.

## 6.2 Outlook

*The parameter space relevant for CEGPs is vast, and only a subset of it has been explored here. The appropriate way to model the effects of the thermal forcing is far from obvious, and even within the simple Newtonian relaxation scheme there are many possibilities to consider. For example, it is unknown at what depth, or over how large a range in depth, the stellar irradiation is absorbed. Thus, looking at variations of the vertical structure of the forcing in a systematic way, is an interesting problem. I have begun to look into this matter and intend to continue this study in detail. This would involve understanding of the vertical propagation and trapping of planetary and/or gravity waves, how this is related to the vertical extent and depth of the forcing region, and how wave motion is affected at the top and bottom boundaries.*

A related topic is the role of drag or dissipation mechanisms that could be at play, and in particular how they would affect wave motions if they are present near the boundaries. In this respect, the effects of unresolved gravity waves could be manifested as a momentum drag, to a first de-

gree [Watkins and Cho, 2010]. Also the presence of magnetic fields could cause an effective drag on the flow [Cho, 2008; Koskinen *et al.*, 2010; Perna *et al.*, 2010]. Other drag and dissipation mechanisms, and some of their possible effects, are discussed in Rauscher and Menou [2011] and Li and Goodman [2010]. But the magnitude and location of all these potential drag mechanisms is very uncertain. In GCM simulations for the Earth, it is common to include “sponge layers”, or enhanced dissipation in the top layers of the model. This is done in order to absorb vertically propagating planetary wave energy and the strength of the dissipation is tuned to match observations [Collins *et al.*, 2004]. But potentially, this kind of drag could cause spurious effects as well, and cause not only damping but also reflection of waves.

In this new regime of application for GCMs it is of great importance to understand when their results are of numerical origin. In this backdrop, model validations and comparisons of different codes are an important avenue to study. I have already been involved with a study addressing this issue directly (see below) and will work on this further. Some work has been done toward this goal in the extrasolar planet literature. Rauscher and Menou [2010] set up their spectral model in a similar way to the finite difference model of Cooper and Showman [2005] and compare their results. Heng *et al.* [2011] propose test cases motivated by Held and Suarez [1994], but extended for a hot Jupiter setup that also resembles Cooper and Showman [2005]. However, these tests emphasise comparison of spatial averages and long term statistics which can easily conceal important problems. Besides, they are rather complex and difficult to compare.

I have taken part in a group project where alternative test cases are studied for extrasolar planet atmospheric circulation code comparison. Some of the test cases we have been studying are similar to Polvani *et al.* [2004], but extended to CEGP conditions. They test how well the codes maintain an exact steady-state solution, and also test the short-term evolution of a slightly perturbed, baroclinically unstable jet, in a well defined setup. In another part of this code comparison study, the codes are stretched to their limits in a setup similar to the cases with the strongest forcing in chapters 4 and 5. Based on the studies presented in this thesis, that is not a realistic way to set up the calculations, but it is useful to un-

derstand where the limits are, and to understand much of the current body of work that has been presented in the literature, concerning extrasolar planet atmospheric circulation.

In future studies, improved ways of setting up the problems and calculations are necessary. More realistic ways of initialising the simulations are needed, instead of letting the atmosphere very suddenly react to huge forcing gradients. This could involve slowly ramping up the heating, and studying the adjustment when an initial state which is close to a balance reacts to the forcing. Of course, the forcing is more complex than has been modelled here. But when taking into account more realistic properties of the forcing (e.g., spatiotemporal variability and dependence on density, temperature, and radiative properties), care must be taken to do it in a meaningful way, and not just add complexity at little reward. Properly resolving or parameterising effects of small scale phenomena such as turbulence and gravity waves, will be important efforts in future studies. In this respect, the distinct states obtained in Chapter 5 can be used as initial conditions in studies where the smaller scale phenomena are better resolved and not overly dissipated, avoiding a too catastrophic initialisation that leads to numerical difficulties.

To gain a better physical understanding of the features and mechanisms, important instabilities and wave types, that are at play in the simulations discussed in this thesis (as well as extensions of those studies), there are several promising ways to move forward, which can build on past success in the geophysical community. As discussed in Chapter 5, based on the results presented in this thesis, simple quasi-geostrophic models may be useful. Also studying the flow in terms of highly truncated spectral analytical methods, similar to the approach of *Charney and Devore* [1979], appears to be a promising route to take.

Understanding gained from CEGP studies may also be useful for comprehending the circulation of planets of other types or masses, especially if they have a similar forcing condition. Several of the extrasolar planets have masses ranging from a few Earth masses to a few Neptune masses, and they orbit very close to their central stars. Their bulk densities indicate solid or ocean surfaces. Hence, they are referred to as super-Earths and hot Neptunes. In future work, I intend to study the atmospheres of these

types of planets. The moderately slow rotation rate of planets in close-in orbits, if assumed tidally-synchronised, can (depending on their characteristic temperatures, strength of gravity and size) put them in a similar dynamical regime as that of the CEGPs, such as HD 209458 b, that have been the subject of this thesis. As an example, the hot Neptune GJ 436 b can be expected to have a Rossby deformation radius which is a large fraction of the planetary radius, so that atmospheric features such as vortices may be relatively large. Thus, understanding the formation and dynamics of large-scale vortices, as well as what controls the time scales of their variability, is important and highly relevant for super-Earths and hot Neptunes. Given the rapid developments in the field of extrasolar planets there will surely be opportunities to apply and extend the lessons learned from this thesis.

# References

- Adcroft, A., J.-M. Campin, C. Hill, and J. Marshall (2004), Implementation of an Atmosphere Ocean General Circulation Model on the Expanded Spherical Cube, *Monthly Weather Review*, 132, 2845.
- Agol, E., N. B. Cowan, H. A. Knutson, D. Deming, J. H. Steffen, G. W. Henry, and D. Charbonneau (2010), The Climate of HD 189733b from Fourteen Transits and Eclipses Measured by Spitzer, *ApJ*, 721, 1861–1877.
- Andrews, D. G., J. R. Holton, and C. B. Leovy (1987), *Middle atmosphere dynamics.*, Academic Press, New York, NY, USA.
- Arakawa, A. (1966), Computational Design for Long-Term Numerical Integration of the Equations of Fluid Motion: Two-Dimensional Incompressible Flow. Part I, *Journal of Computational Physics*, 1, 119.
- Asselin, R. (1972), Frequency Filter for Time Integrations, *Monthly Weather Review*, 100, 487.
- Batchelor, G. K. (1967), *An Introduction to Fluid Dynamics*, Cambridge University Press.
- Boyd, J. P. (2000), *Chebyshev and Fourier Spectral Methods*, 2nd ed., New York, NY: Dover.
- Burrows, A., I. Hubeny, J. Budaj, H. A. Knutson, and D. Charbonneau (2007), Theoretical Spectral Models of the Planet HD 209458b with a Thermal Inversion and Water Emission Bands, *ApJ Letters*, 668, L171–L174.
- Burrows, A., J. Budaj, and I. Hubeny (2008), Theoretical Spectra and Light Curves of Close-in Extrasolar Giant Planets and Comparison with Data, *ApJ*, 678, 1436–1457.
- Byron, F. W., and R. W. Fuller (1992), *Mathematics of Classical and Quantum Physics*, Mineola, NY: Dover.



- Canuto, C., M. Y. Hussaini, A. Quarteroni, and T. A. Zang (1988), *Spectral Methods in Fluid Dynamics*, Springer Ser. Comput. Phys.
- Chapman, S., and R. Lindzen (1970), *Atmospheric tides. Thermal and gravitational*, Dordrecht: Reidel.
- Charbonneau, D., T. M. Brown, D. W. Latham, and M. Mayor (2000), Detection of Planetary Transits Across a Sun-like Star, *ApJ Letters*, 529, L45–L48.
- Charbonneau, D., T. M. Brown, R. W. Noyes, and R. L. Gilliland (2002), Detection of an Extrasolar Planet Atmosphere, *ApJ*, 568, 377–384.
- Charbonneau, D., H. A. Knutson, T. Barman, L. E. Allen, M. Mayor, S. T. Megeath, D. Queloz, and S. Udry (2008), The Broadband Infrared Emission Spectrum of the Exoplanet HD 189733b, *ApJ*, 686, 1341–1348.
- Charbonneau, D., et al. (2005), Detection of Thermal Emission from an Extrasolar Planet, *ApJ*, 626, 523–529.
- Charney, J. G., and J. G. Devore (1979), Multiple Flow Equilibria in the Atmosphere and Blocking, *Journal of Atmospheric Sciences*, 36, 1205–1216.
- Cho, J. Y-K. (2008), Atmospheric dynamics of tidally synchronized extrasolar planets, *Royal Society of London Philosophical Transactions Series A*, 366, 4477–4488.
- Cho, J. Y-K., and L. M. Polvani (1996), The emergence of jets and vortices in freely evolving, shallow-water turbulence on a sphere, *Physics of Fluids*, 8, 1531–1552.
- Cho, J. Y-K., K. Menou, B. M. S. Hansen, and S. Seager (2003), The Changing Face of the Extrasolar Giant Planet HD 209458b, *ApJ Letters*, 587, L117–L120.
- Cho, J. Y-K., K. Menou, B. M. S. Hansen, and S. Seager (2008), Atmospheric Circulation of Close-in Extrasolar Giant Planets. I. Global, Barotropic, Adiabatic Simulations, *ApJ*, 675, 817–845.
- Collins, W. D., et al. (2004), Description of the NCAR Community Atmosphere Model (CAM 3.0), *Tech. rep.*, NCAR, nCAR/TN-464+STR.
- Cooper, C. S., and A. P. Showman (2005), Dynamic Meteorology at the Photosphere of HD 209458b, *ApJ Letters*, 629, L45–L48.

- Cooper, C. S., and A. P. Showman (2006), Dynamics and Disequilibrium Carbon Chemistry in Hot Jupiter Atmospheres, with Application to HD 209458b, *ApJ*, 649, 1048–1063.
- Cowan, N. B., E. Agol, and D. Charbonneau (2007), Hot nights on extrasolar planets: mid-infrared phase variations of hot Jupiters, *MNRAS*, 379, 641–646.
- Crossfield, I. J. M., B. M. S. Hansen, J. Harrington, J. Y-K. Cho, D. Deming, K. Menou, and S. Seager (2010), A New 24  $\mu\text{m}$  Phase Curve for ups Andromedae b, *ApJ*, 723, 1436–1446.
- Deming, D., S. Seager, L. J. Richardson, and J. Harrington (2005), Infrared radiation from an extrasolar planet, *Nature*, 434, 740–743.
- Dobbs-Dixon, I., and D. N. C. Lin (2008), Atmospheric Dynamics of Short-Period Extrasolar Gas Giant Planets. I. Dependence of Nightside Temperature on Opacity, *ApJ*, 673, 513–525.
- Dritschel, D. G., C. V. Tran, and R. K. Scott (2007), Revisiting Batchelor’s theory of two-dimensional turbulence, *Journal of Fluid Mechanics*, 591, 379–391.
- Durran, D. (1999), *Numerical Methods for Wave Equations in Geophysical Fluid Dynamics*, Springer, New York.
- Durran, D. R. (1991), The third-order Adams-Bashforth method - an attractive alternative to leapfrog time differencing, *Monthly Weather Review*, 119, 702–720.
- Edson, A., S. Lee, P. Bannon, J. F. Kasting, and D. Pollard (2011), Atmospheric circulations of terrestrial planets orbiting low-mass stars, *Icarus*, 212, 1–13.
- Eliassen, E., B. Mechenhauer, and E. Rasmussen (1988), Tech. Rep. 2, *Tech. rep.*, Copenhagen Univ., Inst. Teoretisk Meteorologi.
- Fortney, J. J., K. Lodders, M. S. Marley, and R. S. Freedman (2008), A Unified Theory for the Atmospheres of the Hot and Very Hot Jupiters: Two Classes of Irradiated Atmospheres, *ApJ*, 678, 1419–1435.
- Geisler, J. E., and D. E. Stevens (1982), On the Vertical Structure of Damped Steady Circulation in the Tropics, *Quarterly Journal of the Royal Meteorological Society*, 108, 87–93.
- Gill, A. E. (1980), Some simple solutions for heat-induced tropical circulation, *Quarterly Journal of the Royal Meteorological Society*, 106, 447–462.

- Goldreich, P., and S. Soter (1966), Q in the Solar System, *Icarus*, 5, 375–389.
- Grillmair, C. J., D. Charbonneau, A. Burrows, L. Armus, J. Stauffer, V. Meadows, J. Van Cleve, and D. Levine (2007), A Spitzer Spectrum of the Exoplanet HD 189733b, *ApJ Letters*, 658, L115–L118.
- Grillmair, C. J., A. Burrows, D. Charbonneau, L. Armus, J. Stauffer, V. Meadows, J. van Cleve, K. von Braun, and D. Levine (2008), Strong water absorption in the dayside emission spectrum of the planet HD189733b, *Nature*, 456, 767–769.
- Guillot, T., and A. P. Showman (2002), Evolution of “51 Pegasus b-like” planets, *A&A*, 385, 156–165.
- Harrington, J., B. M. Hansen, S. H. Luszcz, S. Seager, D. Deming, K. Menou, J. Y-K. Cho, and L. J. Richardson (2006), The Phase-Dependent Infrared Brightness of the Extrasolar Planet Upsilon Andromedae b, *Science*, 314, 623–626.
- Held, I. M., and M. J. Suarez (1994), A Proposal for the Intercomparison of the Dynamical Cores of Atmospheric General Circulation Models., *Bulletin of the American Meteorological Society*, 75, 1825–1830.
- Heng, K., K. Menou, and P. J. Phillipps (2011), Atmospheric circulation of tidally locked exoplanets: a suite of benchmark tests for dynamical solvers, *MNRAS*, 413, 2380–2402.
- Henry, G. W., G. W. Marcy, R. P. Butler, and S. S. Vogt (2000), A Transiting “51 Peg-like” Planet, *ApJ Letters*, 529, L41–L44.
- Holton, J. R. (2004), *Introduction to Dynamical Meteorology*, Burlington MA, Academic Press.
- Jin, F., and B. J. Hoskins (1995), The Direct Response to Tropical Heating in a Baroclinic Atmosphere., *Journal of Atmospheric Sciences*, 52, 307–319.
- Kasahara, A. (1974), Various Vertical Coordinate Systems Used for Numerical Weather Prediction, *Monthly Weather Review*, 102, 509–+.
- Knutson, H. A., D. Charbonneau, L. E. Allen, J. J. Fortney, E. Agol, N. B. Cowan, A. P. Showman, C. S. Cooper, and S. T. Megeath (2007), A map of the day-night contrast of the extrasolar planet HD 189733b, *Nature*, 447, 183–186.

- Knutson, H. A., D. Charbonneau, L. E. Allen, A. Burrows, and S. T. Megeath (2008), The 3.6-8.0  $\mu\text{m}$  Broadband Emission Spectrum of HD 209458b: Evidence for an Atmospheric Temperature Inversion, *ApJ*, 673, 526–531.
- Knutson, H. A., D. Charbonneau, N. B. Cowan, J. J. Fortney, A. P. Showman, E. Agol, G. W. Henry, M. E. Everett, and L. E. Allen (2009), Multiwavelength Constraints on the Day-Night Circulation Patterns of HD 189733b, *ApJ*, 690, 822–836.
- Koshyk, J. N., B. A. Boville, K. Hamilton, E. Manzini, and K. Shibata (1999), Kinetic energy spectrum of horizontal motions in middle-atmosphere models, *Journal of Geophysical Research*, 104, 27,177–27,190.
- Koskinen, T. T., J. Y-K. Cho, N. Achilleos, and A. D. Aylward (2010), Ionization of Extrasolar Giant Planet Atmospheres, *ApJ*, 722, 178–187.
- Langton, J., and G. Laughlin (2007), Observational Consequences of Hydrodynamic Flows on Hot Jupiters, *ApJ Letters*, 657, L113–L116.
- Langton, J., and G. Laughlin (2008), Hydrodynamic Simulations of Unevenly Irradiated Jovian Planets, *ApJ*, 674, 1106–1116.
- Li, J., and J. Goodman (2010), Circulation and Dissipation on Hot Jupiters, *ApJ*, 725, 1146–1158.
- Lim, H., and C.-P. Chang (1983), Dynamics of Teleconnections and Walker Circulations Forced by Equatorial Heating., *Journal of Atmospheric Sciences*, 40, 1897–1915.
- Longuet-Higgins, M. S., and A. E. Gill (1967), Resonant Interactions between Planetary Waves, *Royal Society of London Proceedings Series A*, 299, 120–140.
- Lubow, S. H., C. A. Tout, and M. Livio (1997), Resonant Tides in Close Orbiting Planets, *ApJ*, 484, 866.
- Matsuno, T. (1966), Quasi-Geostrophic Motions in the Equatorial Area, *Journal of the Meteorological Society of Japan*, 44, 25.
- Mayor, M., and D. Queloz (1995), A Jupiter-mass companion to a solar-type star, *Nature*, 378, 355–359.
- Menou, K., and E. Rauscher (2009), Atmospheric Circulation of Hot Jupiters: A Shallow Three-Dimensional Model, *ApJ*, 700, 887–897.

- Menou, K., J. Y-K. Cho, S. Seager, and B. M. S. Hansen (2003), “Weather” Variability of Close-in Extrasolar Giant Planets, *ApJ Letters*, 587, L113–L116.
- Nayfeh, A. H. (1973), *Perturbation Methods*, New York, NY: Springer-Verlag.
- Orszag, S. A. (1970), Transform Method for the Calculation of Vector-Coupled Sums: Application to the Spectral Form of the Vorticity Equation., *Journal of Atmospheric Sciences*, 27, 890–895.
- Orszag, S. A. (1971), On the Elimination of Aliasing in Finite-Difference Schemes by Filtering High-Wavenumber Components., *Journal of Atmospheric Sciences*, 28, 1074–1074.
- Pedlosky, J. (1987), *Geophysical Fluid Dynamics*, New York, NY: Springer-Verlag.
- Perna, R., K. Menou, and E. Rauscher (2010), Magnetic Drag on Hot Jupiter Atmospheric Winds, *ApJ*, 719, 1421–1426.
- Polvani, L. M., R. K. Scott, and S. J. Thomas (2004), Numerically Converged Solutions of the Global Primitive Equations for Testing the Dynamical Core of Atmospheric GCMs, *Monthly Weather Review*, 132, 2539.
- Rasio, F. A., C. A. Tout, S. H. Lubow, and M. Livio (1996), Tidal Decay of Close Planetary Orbits, *ApJ*, 470, 1187.
- Rauscher, E., and K. Menou (2010), Three-dimensional Modeling of Hot Jupiter Atmospheric Flows, *ApJ*, 714, 1334–1342.
- Rauscher, E., and K. Menou (2011), The Role of Drag in the Energetics of Strongly Forced Exoplanet Atmospheres, *ArXiv e-prints (submitted to ApJ)*.
- Rauscher, E., K. Menou, J. Y-K. Cho, S. Seager, and B. M. S. Hansen (2007), Hot Jupiter Variability in Eclipse Depth, *ApJ Letters*, 662, L115–L118.
- Rhines, P. B. (1975), Waves and turbulence on a beta-plane, *Journal of Fluid Mechanics*, 69, 417–443.
- Robert, A. (1966), The integration of a low order spectral form of the primitive meteorological equations, *J. Meteorol. Soc. Japan. Ser. II*, 44, 237.

- Salby, M. L. (1989), Deep circulations under simple classes of stratification, *Tellus Series A*, 41, 48–65.
- Salby, M. L. (1996), *Fundamentals of Atmospheric Physics*, Academic Press, Inc., San Diego, California, USA.
- Saravanan, R. (1993), Equatorial Superrotation and Maintenance of the General Circulation in Two-Level Models, *Journal of Atmospheric Sciences*, 50, 1211–1227.
- Scott, R. K. (2010), The structure of zonal jets in shallow water turbulence on the sphere, in *Proceedings of the IUTAM Symposium on Rotating Stratified Turbulence*, edited by Dritschel, D. K., IUTAM Bookseries, pp. 243–252, Springer.
- Scott, R. K., and L. M. Polvani (2008), Equatorial superrotation in shallow atmospheres, *Geophysical Research Letters*, 35, L24,202.
- Showman, A. P., and T. Guillot (2002), Atmospheric circulation and tides of “51 Pegasus b-like” planets, *A&A*, 385, 166–180.
- Showman, A. P., and L. M. Polvani (2010), The Matsuno-Gill model and equatorial superrotation, *Geophysical Research Letters*, 37, L18,811.
- Showman, A. P., and L. M. Polvani (2011), Equatorial superrotation on tidally locked exoplanets, *ArXiv e-prints (in press at ApJ)*.
- Showman, A. P., C. S. Cooper, J. J. Fortney, and M. S. Marley (2008a), Atmospheric Circulation of Hot Jupiters: Three-dimensional Circulation Models of HD 209458b and HD 189733b with Simplified Forcing, *ApJ*, 682, 559–576.
- Showman, A. P., K. Menou, and J. Y-K. Cho (2008b), Atmospheric Circulation of Hot Jupiters: A Review of Current Understanding, in *Extreme Solar Systems, Astronomical Society of the Pacific Conference Series*, vol. 398, edited by D. Fischer, F. A. Rasio, S. E. Thorsett, & A. Wolszczan, p. 419.
- Showman, A. P., J. J. Fortney, Y. Lian, M. S. Marley, R. S. Freedman, H. A. Knutson, and D. Charbonneau (2009), Atmospheric Circulation of Hot Jupiters: Coupled Radiative-Dynamical General Circulation Model Simulations of HD 189733b and HD 209458b, *ApJ*, 699, 564–584.
- Simmons, A. J., and R. Strufling (1981), NCAR Technical Report No. 28: An Energy and Angular Momentum Conserving Finite-Difference Scheme, Hybrid Coordinates and Medium-Range Weather Prediction, *Tech. rep.*, NCAR.

- Simmons, A. J., B. J. Hoskins, and D. M. Burridge (1978), Stability of the Semi-Implicit Method of Time Integration, *Monthly Weather Review*, *106*, 405.
- Sing, D. K., J.-M. Désert, A. Lecavelier Des Etangs, G. E. Ballester, A. Vidal-Madjar, V. Parmentier, G. Hebrard, and G. W. Henry (2009), Transit spectrophotometry of the exoplanet HD 189733b. I. Searching for water but finding haze with HST NICMOS, *A&A*, *505*, 891–899.
- Suarez, M. J., and D. G. Duffy (1992), Terrestrial Superrotation: A Bifurcation of the General Circulation., *Journal of Atmospheric Sciences*, *49*, 1541–1556.
- Swain, M. R., G. Vasisht, and G. Tinetti (2008), The presence of methane in the atmosphere of an extrasolar planet, *Nature*, *452*, 329–331.
- Thrastarson, H. T., and J. Y-K. Cho (2010), Effects of Initial Flow on Close-in Planet Atmospheric Circulation, *ApJ*, *716*, 144–153.
- Thrastarson, H. T., and J. Y-K. Cho (2011), Relaxation Time and Dissipation Interaction in Hot Planet Atmospheric Flow Simulations, *ApJ*, *729*, 117.
- Tinetti, G., et al. (2007), Water vapour in the atmosphere of a transiting extrasolar planet, *Nature*, *448*, 169–171.
- Vallis, G. K. (2006), *Atmospheric and Oceanic Fluid Dynamics*, Cambridge University Press.
- Wan, H., M. A. Giorgetta, and L. Bonaventura (2008), Ensemble Held Suarez Test with a Spectral Transform Model: Variability, Sensitivity, and Convergence, *Monthly Weather Review*, *136*, 1075.
- Watkins, C., and J. Y-K. Cho (2010), Gravity Waves on Hot Extrasolar Planets. I. Propagation and Interaction with the Background, *ApJ*, *714*, 904–914.
- Williams, G. P. (1978), Planetary circulations. I - Barotropic representation of Jovian and terrestrial turbulence, *Journal of Atmospheric Sciences*, *35*, 1399–1426.
- Williams, P. D. (2009), A Proposed Modification to the Robert-Asselin Time Filter, *Monthly Weather Review*, *137*, 2538.
- Wolszczan, A., and D. A. Frail (1992), A planetary system around the millisecond pulsar PSR1257 + 12, *Nature*, *355*, 145–147.